SOLID STATE ADDITIVE MANUFACTURING

A STUDY TO UNDERSTAND THE BONDING PROCESS OF FRICTION SURFACING USING AA2024-T351 ONTO AA2024-T351.

M. de Leede
Msc thesis
May, 2017

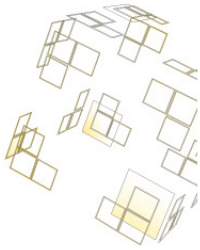

PRODUCTION TECHNOLOGY
MECHANICAL ENGINEERING

EXAMINATION COMMITTEE
Dr. Ir. T.C. Bor
Dr. Ir. S. Liu
Dr. Ir. H.J.M. Geijselaers

DOCUMENT NUMBER
MS3/PT-0002

UNIVERSITY OF TWENTE.

Preface

This thesis was written to complete the master study of Mechanical Engineering at the University of Twente. The research was conducted under the supervision of the research chair of Production Technology at the department Mechanics of Solids, Surfaces and Systems. It represents my findings in the study for the understanding of the bonding behaviour during a friction surfacing process. This report is primarily addressed for the researchers of the new solid state additive manufacturing process. The knowledge I gained in this thesis will be helpful as a foundation for the new design of the solid state additive manufacturing process.

A large part of the subject in this thesis covers the metallurgic behaviour of certain aluminium alloys. As a mechanical engineer, the material knowledge required a lot of literature research for me. Therefore the thesis is written in such a way that someone who lacks knowledge about material science can easily find the most important factors of the specific aluminium alloys in this thesis.

Enjoy your reading,

Marijn de Leede
14 May 2017, Enschede

Acknowledgements

This thesis, as well as my study at the University of Twente, would not have been completed without the support of many people. I would like to use this opportunity to thank the people who have helped in this process.

A special thanks to my daily supervisor Ton Bor, Who managed to give me more questions than answers in almost every conversation we had. But because of that he left me curious to find the answers on this subject. The extensive assistance and valuable input I have received from him was remarkable. I would also like to thank Shaojie Liu, who functioned as a daily adviser to me for all the practical problems during this study and was always ready for a discussion on theory of the subject. Bert Geijselaars I would like to thank for participating my graduation committee.

Finally, I would like to thank my girlfriend, mother and father for their support during my studies. I could always count on your support and you have my gratitude for that.

Summary

Additive manufacturing (AM), or 3D printing, provides a new and challenging approach towards mold-free product manufacturing through a layer-by-layer deposition of thin layers. State-of-the-art metal AM is mostly fusion based allowing complex product shapes to be realized. Unfortunately, the materials microstructure is often non-homogeneous and suffers from porosity and residual stresses. Only a limited number of alloys can be employed due to solidification related problems, such as cracking.

A new and promising approach to extend the range of alloys applicable and to improve the microstructure of the manufactured product is based on solid stage deposition. Within this research project the possibilities and limitations of solid state additive manufacturing have been investigated. The manufacturing process is based on the friction surface cladding process developed within the PT research chair. Here, frictional heating and compressive forces are used to enable controlled deposition of thin layers on a substrate in the solid state.

The aim of this study was to understand the bonding process of the added metal on the substrate and to find the important parameters that determine the bonding quality. The research concentrated on the deposition of a high strength aluminium alloy 2024-T351 typically used for aerospace applications.

In this study, an experimental study using friction surfacing was performed to investigate the bonding behaviour. The experimental setup consisted out of a rotating aluminium 2024-T351 rod(mechtrode) that was forced with an axial force onto an aluminium 2024-T351 plate (substrate). The frictional forces initiated heating that allowed the bonding of the mechtrode onto the substrate. Sets of different axial forces, rotational speeds and surface temperatures were investigated. Base on the measurements of the force, torque and temperature the bonding process could be divided into four different stages.

In stage I_a, the process was started, shortly after the temperature and the axial force reached a plateau. In stage I_b, both the temperature and the applied torque suddenly rose. In Stage II, local plastic deformation at the mechtrode was observed, a peak was reached at the applied torque and was starting to drop, the temperature started to level. In Stage III, the temperature was levelled and plastic deformation was observed around the whole contact surface. A deposit started to grow between the mechtrode and substrate. Finally, the deposit started to rise. The various sets of experiments presented in this work showed that bonding can be achieved within a large range of process parameters.

Subsequently, a thermo-mechanical model was made to investigate the temperature distribution during the bonding process and to explain the stages that occurred in the process. In stage I_b it showed that the sudden rise in temperature was caused by a saturation of heat for the surrounding materials in combination with a rising friction coefficient for rising temperature. Stage II could be approximated by an analytical equation combining Coulomb's law of friction with the flow stress of the material with an exponentially declining. And at stage III, it was found that the rise of the contact area is caused by the substrate that is better in conducting heat away in comparison to the mechtrode.

Finally, the quality of the bonding was investigated using uniaxial tensile tests on the samples and hardness test and a microscope study on the cross sections of the samples for the different parameter sets. It showed that the hardness distribution is similar to FS of other materials and based on the hardness distribution the cross section of a sample could be divided into three zones. A thermo-mechanical effected zone, in this zone the material was influenced by the mechanically induced shear and heat, a heat effected zone, in this zone only the heat was effecting the material structure and finally the base material, in this zone the penetration of the heat was too low to cause change in the material structure. The tensile test showed that higher rotation speeds and higher axial forces during the experiment, that caused a more unstable bonding process, resulted in a lower ultimate tensile force (UTF) of the bonding. It was also found that the minimum required temperature at the inside thermocouple location had to be 240 °C for bonding to be initiated between the mechtrode and the substrate.

This study showed that with a broad operation window the bonding of aluminium 2024-T351 onto aluminium 2024-T351 is possible. Yet the influence of the parameters on the bonding quality cannot be neglected and caused a reduction loss between 14 and 29% of the initial hardness. However, higher hardness values did not necessarily result a higher UTF of the bonding, showing that influence of the parameters on the stability of the bonding process was more important than the loss of hardness for the bonding quality.

Nomenclature

Abbreviations

AA	Aluminium alloy
BM	Base material
EBSD	Electron back scatter diffraction
FEM	Finite element model
FS	Friction surfacing
FSC	Friction surface cladding
FZ	Friction zone
RPM	Rotation per minute
SSAM	Solid state additive manufacturing
TMAZ	Thermal mechanical effected zone
UTF	Ultimate tensile force

Greek symbols

δ	The slip/stick coefficient	-
θ	The angle along the mechtrode's longitudinal axis	-
θ-phase	Phase of the Al_2Cu precipitate	-
σ_{33}	The stress in the mechtrode longitudinal direction	MPa
σ_P	The pressure of the press	MPa
σ_s	The pressure of the feed material on the substrate	MPa
$\tau_{contact}$	The contact shear stress between the mechtrode and the substrate	MPa
τ_{flow}	The maximum stress before the material flows	Mpa
ω	The rotation speed of the mechtrode	rad/s
ω_s	The rotation speed of the feed material	rad/s
ω_t	The rotation speed of the rotation tool	rad/s

Roman symbols

F	The axial force on the mechtrode	N
F_0	The starting force on the mechtrode	N
J_t	The torsion constant	m^3
M	The torsion on the mechtrode	Nm
Q	The total heat	W
P	The pressure in the mechtrode	MPa
P_t	The pressure of the press	MPa
Q_{slip}	The heat generation from slipping	W
Q_{stick}	The heat generation from sticking	W
R	The radius of the mechtrode	m
R_{eff}	The effective radius of the mechtrode	m
S-phase	Phase of the Al_2CuMg precipitate	-
T_{ci}	The temperature of the inside thermocouple	°C
T_{co}	The temperature of the outside thermocouple	°C
T_{sub}	The highest temperature at the thermocouples location	°C
V_t	The speed of the feed material	m/s

Contents

Chapter 1

Introduction

Additive manufacturing(AM), or 3D printing, provides a new and challenging approach towards mold-free product manufacturing through a layer-by-layer deposition of thin layers. Currently AM materials can be divided into two major fields 'polymers' and 'metals'. The metal field has been intensively studied and used in the industry. Many processes using lasers, electron beam and arc techniques have been developed that showed good results[1]. Unfortunately, certain metal alloys such as many alloys of the aluminium 2xxx-serie show solidification related problems that makes it nearly impossible to use the previously stated process for AM.

A solution for that problem could be the solid state additive manufacturing (SSAM). This technology is quite similar to already broadly studied Friction Stir Welding (FSW), a technology that uses rotational friction to join materials e.g. AA2024-T35 joints [2]. The advantage of FSW in comparison to conventional welding methods is that the heat input required is much lower, solidification related problems are absent and dimensional and microstructural changes remain modest [3]. This technique makes it also possible to join different types of materials e.g. aluminium to copper [4].

While FSW only joins materials, preferably plates, SSAM creates a multidimensional model using a layer by layer build up. One of the first recorded SSAM methods is Friction Surfacing (FS). FS uses a rotating consumable clad rod (mechtrode) that is pressed against a metal product (substrate). Friction occurs at the interface leading to local heating and softening of the clad rod. As soon as the clad rod and the substrate are heated up sufficiently, the rotating rod is moved over the substrate surface while being pressed against it. Part of the softened clad rod is transferred to the substrate generating a clad layer [5]. More of the FS process is explained in Chapter 2.

A typical problem of FS is excessive flash formation. The applied pressure on the rotating rod is relatively high compared to the strength of the rod near the clad rod-substrate interface. This leads to severe plastic deformation and the loss of large amounts of clad material [3]. Van der Stelt et al. [6] introduced a solid state process, called Friction Surface Cladding (FSC), with the aim of, amongst others, solving the main problems observed in FS. This process provides effective control over the deposition of the clad material by using a specially designed cladding tool. Inspired by the setup of Van der Stelt et al. the Production Technology (PT) group from the university of Twente has been designing a new process that is explained in the next section.

1.1 The new SSAM setup

The design of the new SSAM process is shown in Figure 1.1. At the start of the process the material is fed through a tube, Figure 1.1(a). At a certain time the material makes contact with the rotation tool, Figure 1.1(b). Frictional forces between the feed material and the rotation tool generate heat that softens the feed material.The pressure of the press causes the material to flow. The geometry of the rotation forces most of the material downwards until the material reaches the substrate, Figure 1.1(c). The thermal mechanical process between the feed material and the substrate creates a bonding, Figure 1.1(d). Once proper bonding between the feed material and the substrate is achieved the housing will translate to deposit the feed material onto the substrate, Figure 1.1(e). The final step in process is the refill, Figure 1.1(f). In comparison to conventional SSAM methods this process allows refilling of the material while the process is still working. The lateral confinement of the housing prevent the problems that occur at flash forming by for example FS.

In general the process can be divided into four parts, the feeding part where the material is fed and will deform around the rotating tool, the bonding part where the feeding material will touch the substrate and start to bond, the translation part, once a proper bond is set the setup will translate to expand the bonding and the refill part. In an explorative it was found that approximately 3kN was necessary for the feeding of alumimium 1050 with a diameter of 10mm, proving that semi continues feeding process like this can be achieved with relatively low process parameters. Though due to the limited academical models that could be fitted on this process it was chosen to concentrate on the second part of the process. Technical drawings have been added in appendix A and B.

One of the most important parts of the process is the bonding of the feed material to the substrate. In order to get understanding of the bonding process, the conditions of step c and d of the new SAMM setup need to be known. The aim of this study is therefore to create an understanding of the bonding process and to find the parameters that give the optimal bonding.

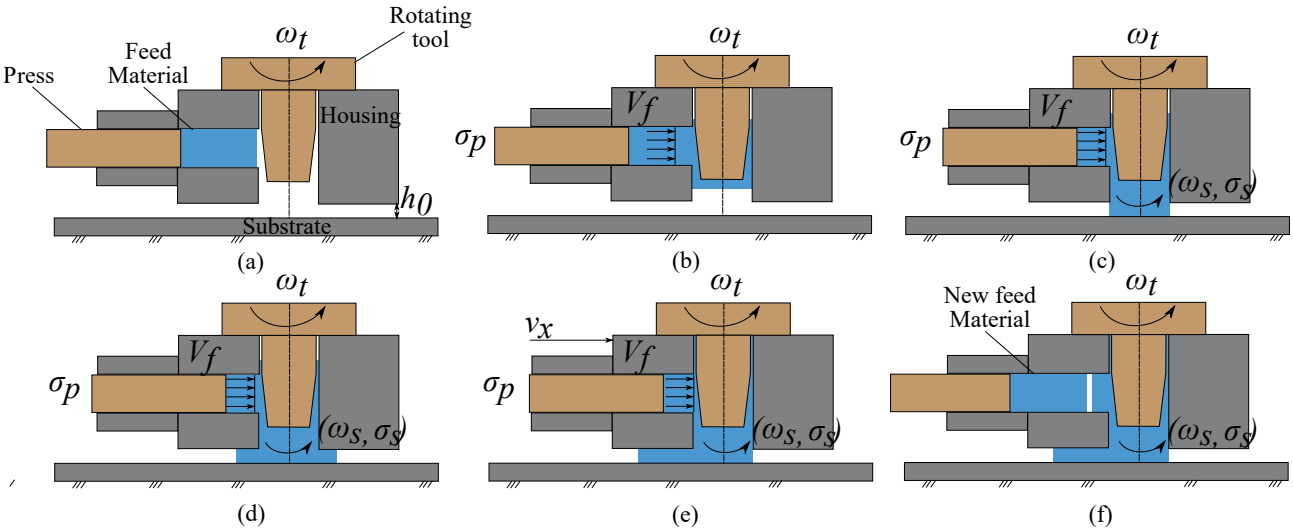

Figure 1.1: *Schematic steps of the new SSAM process: (a) the cladding tool positioned at required height and start of tool rotation at a rotation rate of ω_t, (b) the feed material makes contact with the rotating tool and deforms around it, heat is generated and the feed material will warm up (c) the feed material leaves the housing and has a rotation speed of ω_s and applies a pressure of σ_s (d) on the substrate (d) the cladding phase starts: the rotating tool translates with respect to the substrate at translation speed of v_t.*

The fusion process that enables the bonding is a complex process that is influenced by a lot of variables. The most important parameters of the fusion process are the amount of heat and compressive forces that are used. The heat in turn is dependant of the rotation speed and the frictional forces between the feed material, substrate and setup. S. Liu et al. [3] showed that stable deposition of aluminium AA1050 onto AA2024 through FSC is possible, but due to the difference in conditions of the setup, the found process window cannot be used for the new design of PT. Figure 1.1 shows that the new design is also not suited to create an understanding of the bonding process. Because the rotation speed of the feed material in this setup will still be unknown. Therefore it will be hard to determine the amount of heat that is generated and will end up in the substrate. A new experimental setup is needed that is able to extract the bonding conditions in a similar situation as step c and d of the new SAMM process, while the rotation speed of the feed material can be determined.

In Figure 1.2 a FS setup is proposed that is able to simplify the bonding process, while simulating the situation of Figure 1.1 (c) and (d). The setup works with a metal rod (mechtrode) that is pressed to a metal plate (substrate) with axial force F and rotation speed ω. The work of the mechtrode is transferred through frictional forces between the mechtrode to the substrate into heat. When enough heat is generated the mechtrode will bond to the substrate. In the experiment the mechtrode is directly connected to the motor and thus the rotational speed can be measured. When it is assumed that all heat is transferred into heat, the generated heat can be found with equation 1.1.

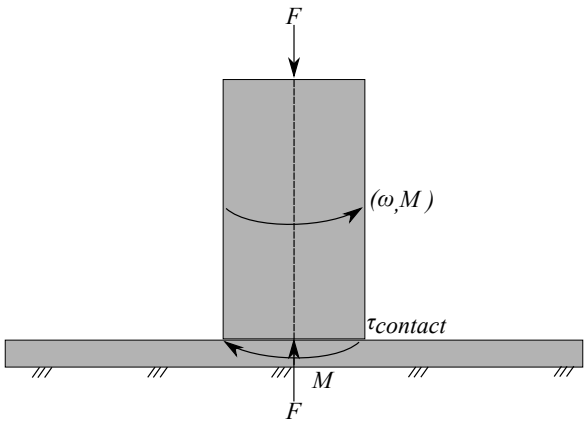

Figure 1.2: *The experimental setup with a stationary rotating mechtrode. The applied torque, rotation speed and axial force will be measured to create an understanding of the bonding process.*

$$dQ = \omega dM \tag{1.1}$$

Although the subject of FS has already been studied, all of the literature focuses on the translating steady state part of the process with a translating mechtrode. Therefore, the bonding process is not fully understood. In these experiments the mechtrode will remain stationary enabling to control the deposition and to study the starting phase of FS to understand the bonding process.

1.2 Objective and scope

In this thesis the bonding mechanism of the startup phase of a FS process using an aluminium mechtrode and an aluminium substrate is studied. An experimental setup is used to investigate the effect of the parameters: axial force(F), rotation speed (ω) and the contact surface temperature between the mechtrode and the substrate (T_{con}) on the quality of the bonding, other parameters are left for further study. The goal is to create an understanding of the bonding process and to find the parameters that give the optimal binding. An understanding of the bonding process is required to minimize the influence of the bonding process on the initial microstucture and mechanical properties of the material.
The relations that influence the bonding quality is divided into the initial conditions and the conditions during the experiment. The initial conditions are the conditions that will remain the same during the whole research. The conditions during the experiment will vary for each test. Some of these parameters i.e. the axial force, rotation speed and contact surface temperature will change according to a predefined research scheme the others will change because of the changes in these parameters. In conditions post experiment the quality of the bonding is tested, using several tests that determine the property of bonding. In Figure 1.3 a schematic overview of this is shown.

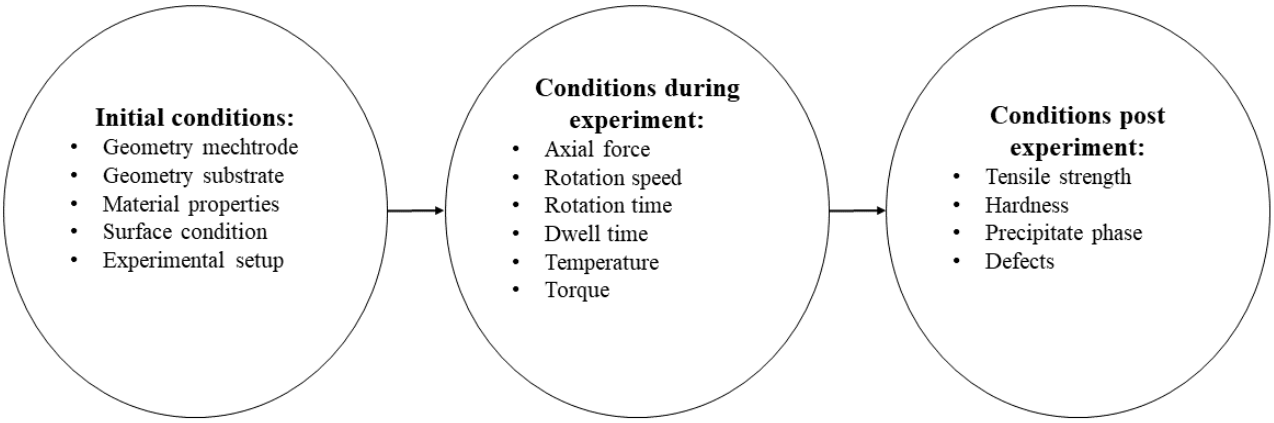

Figure 1.3: *Schematic overview of the correlation between the initial conditions, conditions during the experiments and the condition after the experiment that determine the quality of the bonding.*

1.3 Outline

The outline of this thesis is schematically illustrated in Figure 1.4. The thesis is divided into two subjects. The chapters can be bonding process related, bonding quality related or both. Chapter 2 introduces a literature study for the material selection, the FS process and then an analytical model is introduced that describes the heat generation of the FS, to form a basis for the following chapters. In chapter 3 the range of each tested parameter of the FS experiment is defined, the experimental setup is explained and the data of the experiments analysed. Subsequently a thermo-mechanical model is made in chapter 4. The model approximates the real temperature distribution using the measured torque of chapter 3 as input and the measured temperature as a control. The heat distribution from the thermo-mechanical model and the analytical model used to explain the stages of the bonding process. In Chapter 5 the quality of the bonding is studied with use of hardness and tensile tests. In this chapter the theory of the selected material from Chapter 2 and the temperature distribution of chapter 4 are used to explain the hardness observations in the bonding. Chapter 6 addresses the discussion that reflects on the main findings of the work. Finally, the main conclusions of this study together with some recommendations are presented in Chapter 7.

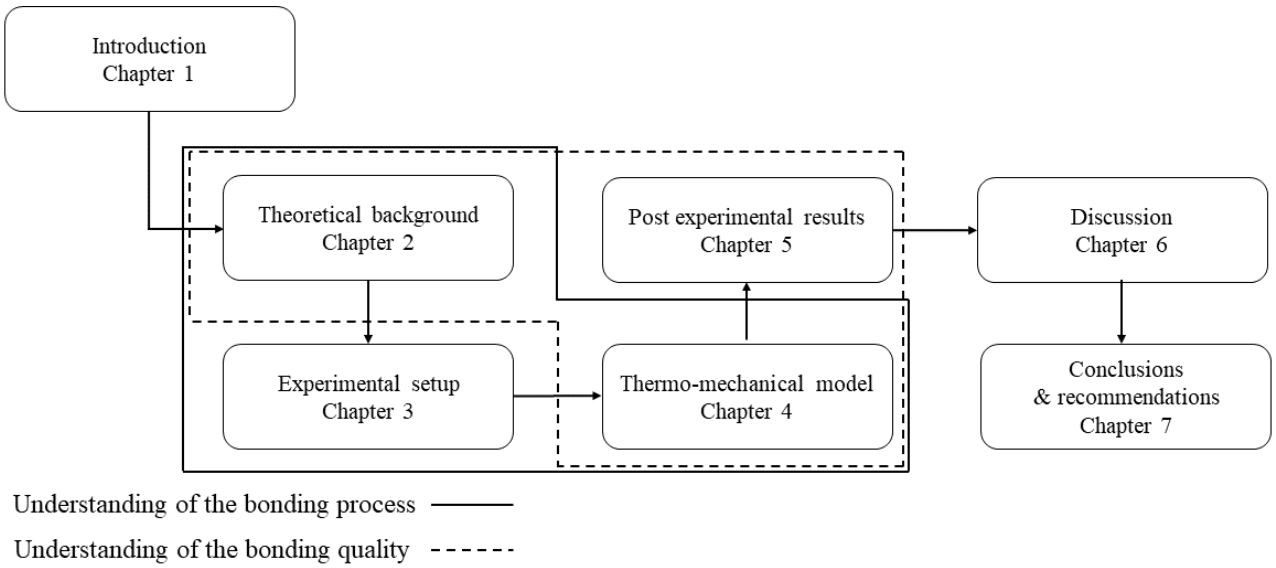

Figure 1.4: *Schematic representation of the thesis outline*

Chapter 2

Theoretical background

This chapter is dedicated to the theoretical background that is needed for further investigation in this study. In this chapter chapter a small literature review is done for the properties of aluminium 2024 alloy, the process of FS and analytical models that are used to predict the process of FSW.

2.1 Aluminium 2024

The 2xxx series alloy, having copper as the primary alloy addition, posses high strength but a somewhat lower corrosion resistance than most other aluminium alloys. Therefore it is often clad with aluminium or Al-Zn for protection, although this may reduce the fatigue strength [7]. Many of these alloys also possess relatively good elevated- temperature strength. Magnesium is also added to the 2xxx series alloys for increased strength but results in greater crack sensitivity when the material solidifies. Alloy 2024 is one of the highest-strength 2xxx alloy and is used extensively in the aircraft industry; however, the 3.8 - 4.9 wt% Cu content of 2024 hinders its weldability due to increased weld crack sensitivity [8]. The FSW process in SSAM bonds the material at a temperature near the solidus of the material, lowering the risk of weld cracks. This enables the process to bond materials where other processes can have a substantial difficulty with bonding. Therefore the aluminium 2024 composition has been chosen to be investigated in this study. The nominal chemical composition of this material is shown in Figure 2.1.

Table 2.1: *Chemical composition of aluminium 2024 [9].*

Element (wt %)	Al	Cr	Cu	Fe	Mg	Mn	Si	Ti	Zn
AA2024	90.7 - 94.7	$\leq$0.1	3.8 - 4.9	$\leq$0.5	1.2 - 1.8	0.3 - 0.9	$\leq$0.5	$\leq$0.15	$\leq$0.25

Precipitates

The AA2024 alloy is a heat-treatable alloy. Increase of strength and hardness can be achieved by heating and cooling, through development of precipitations. The mechanism of strengthening from precipitates involves the formation of coherent clusters of solute atoms. Clusters of solute atoms have collected but still have the same crystal structure as the solvent. This causes strain because of mismatch in size between the solvent and the solute atoms. Consequently, the presence of the precipitates, and the strain fields in the matrix surrounding the coherent particles, provide higher strength by obstructing and retarding the movement of dislocations [8]. Essential for forming of precipitates, is a temperature dependent equilibrium solid solubility characterized by increasing solubility with increasing temperature, see the solvus of Figure 2.1(a). The precipitates that play a major role in the strength- and hardening of the 2024 alloy are:

- Aluminium-copper (Al_2Cu), strengthens the composition [10], [11],[12] and [13].
- Aluminium-copper-magnesium (AL_2CuMg), addition of magnesium to (Al_2Cu) alloys accelerate and intensify natural age hardening [10], [11],[14],[12], [15] and [16].

The general requirement for precipitation strengthening of supersaturated solid solutions involves the formation of finely dispersed precipitates during ageing heat treatments (which may include either natural ageing or artificial ageing). In this study the heat treatment T351 and T4 will be considered.

With a T351 and 4-treatment the aluminium is heated between 488-499 $^\circ$C, by diffusion all Cu and Mg will be in solid solution as a stable Face centred cubic (FCC) α phase, see Figure 2.1(b). By quenching the specimen into water there is no time for any transformation to occur so that the solid solution is retained largely unchanged to room temperature. Hence, the solid solution is now supersaturated with Cu and Mg and there is a driving force for precipitation of the equilibrium θ-phase ($CuAl_2$) and S-phase (AL_2CuMg)[17], see Figure 2.2 (b).

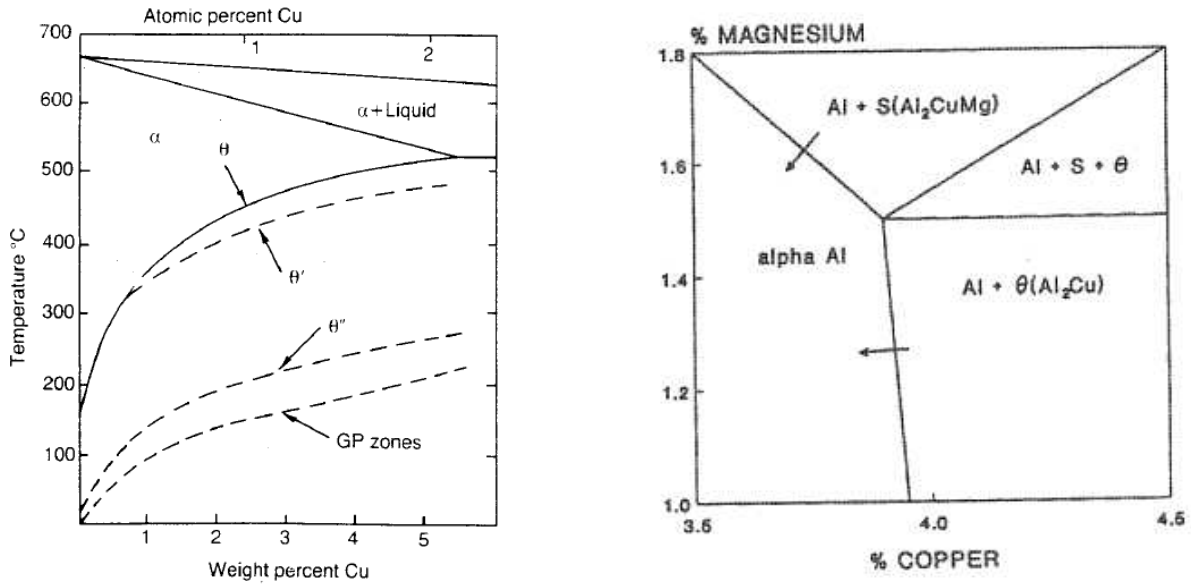

Figure 2.1: *(a) Phase diagram of the AlCu [17]; note the GP zones lowest interfacial energy of the phases of the AlCu compositions, this zone is also metastable. The solvus is on the θ-line. (b) Composition-phase relations for an Al-Cu-Mg system at 499° C, according to R.D. Dalward [18].*

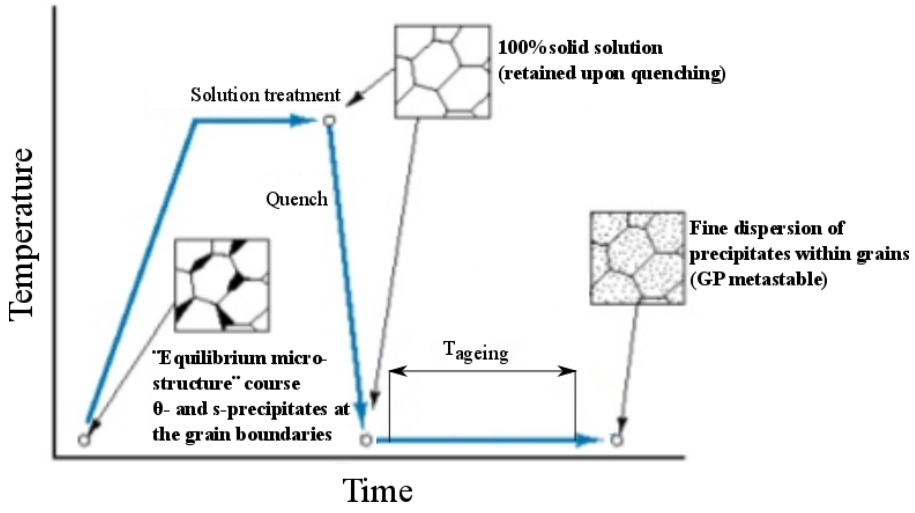

Figure 2.2: *The heat treatment of aluminium 2024 T351/4. Note the changes in microstructure after each process step.*

Phase forming

In literature the formation of the θ-phase has been investigated thoroughly. It is found that a series of intermediate metastable phases, the gp-zones, precedes the formation of the θ-phase, when aluminium 2024 is left for natural ageing. These consist of one atom layer copper-rich regions of a disk like shape, orientated parallel to $\{100\}$ planes. The diameter of these zones does not change with ageing time at room temperature and is estimated to be 3 to 5 nm. The number is not constant and increases with time, until in fully age condition, the average distance between zones is about 100 nm. The GP zones start to disappear at a temperature of 100 °C and higher and are replaced by a structure designated θ" which, see Figure 2.1(a), although only a few atoms layers in thickness, is considered to be three-dimensional and has to have an ordered atomic arrangement. The transition phase, θ', having the same composition as the stable phase, forms after θ" but coexist with it over a range of time and temperature. The final stage in the sequence is the transformation of θ' into θ [19]. The time and temperature dependent structure sequence may be reads as:

$$SS \rightarrow GP \rightarrow \theta" \rightarrow \theta' \rightarrow \theta \tag{2.1}$$

Despite the presence of S-phases in the most of the popular commercial aluminium compositions, the details of the precipitation mechanism and structures are less well developed than those of the θ-phase. The formation of zones during natural ageing have been observed, but so far it has not been possible to determine their form or size They are believed to collect on $\{110\}$ matrix planes in groups of magnesium and copper atoms [19]. The observed acceleration of this process by the addition of magnesium can be the result of complex interaction between vacancies and the two solutes. Another suggestion is the preparatory pairing of the copper and magnesium atoms, the pairing may increase hardening by a mechanism of dislocation pinning. Elevated temperatures ageing of the 2024 alloy produces the transition phase S', which is on $\{021\}$ matrix planes, whereas temperatures that reach overageing produce the formation of the equilibrium S phase [19]. The time and temperature dependent structure sequence may be reads as:

$$SS \rightarrow GP \rightarrow S' \rightarrow S \tag{2.2}$$

The reason for the formation of the phases has to do with the relative activation energy barriers for nucleation. The GP zones are fully coherent with the matrix and this results in a very low interfacial energy, whereas the θ and S have a complex tetragonal crystal structure which results in incoherent interfaces that have a high interfacial energy. Because of this, the barrier to nucleation is lower for the GP zones than for the θ-phase, despite the fact that the driving force for precipitation of GP zones is less than for the equilibrium phase the zones nucleate more rapidly. Transition phases form for the same reason, only is their activation energy barrier higher than the GP zones, but still lower than the equilibrium phase, see Figure 2.3(I). In an alloy with no transition phases the free energy would only decrease at the equilibrium phase. In an alloy with the transition phases, the transition phases cause a decrease for each transition phase, therefore decreasing the free energy more rapidly as can be seen in Figure 2.3(II). The crystal structures of the transition phases are intermediate between those of the matrix and the equilibrium phase, thus lowering the activation energy that is needed [17].

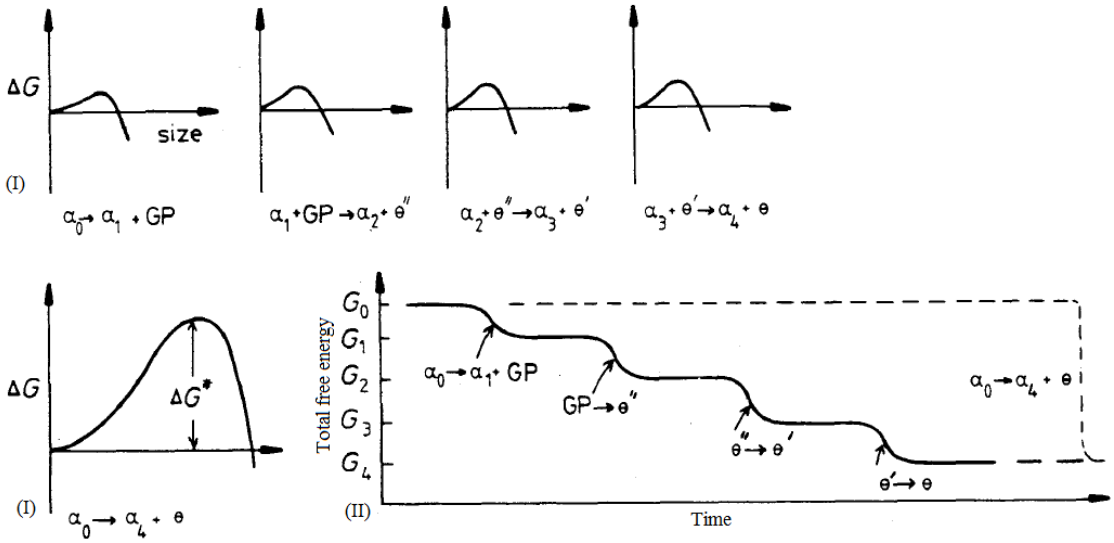

Figure 2.3: *(I) The activation energy barrier to the formation of each transition phase is very small in comparison to the barrier against the direct precipitation of the equilibrium phase. (II) Schematic diagram showing the total free energy of the alloy versus time[17]*

Ageing

The formation sequence of GP zones and transition precipitates is only possible when ageing is performed at a temperature below the transitional solvus. For example, the precipitate will be θ' nucleated on the dislocations, when ageing is carried out at a temperature above the θ" solvus but below the θ' solvus. When ageing is performed at a temperature above the θ' solvus, the only precipitates that will appear are the θ-precipitates which nucleates and grows at grain boundaries[20]. When an alloy contains GP-zones by for example natural ageing, and is heated beyond the GP-zone solvus afterwards, the zones will dissolve. This is known as reversion. The TTT-diagram in Figure 2.4(a) illustrates the effect of ageing temperature and time on the sequence of precipitates.

Solution treatment and ageing operations can greatly improve the mechanical properties of alloys that show transition phase precipitation. The correlation of these structures with the hardness is illustrated in Figure 2.4(b). The curves vary in absolute values for different ageing temperatures but the same trend remains. The

hardness can be explained based on the microstructure of the transitional phases. Immediately after quenching the GP zone have not formed yet, therefore the main resistance to dislocation movement is solid solution hardening. Deforming of the specimen is relatively easy and the hardness is low. Overtime the GP zones are formed, with the increase of GP zones the hardness increases due to the extra stress required to force dislocations through the coherent zones. When coherent θ" precipitates are formed the hardness increases further, because the misfit from the θ" plates causes a high strain field that limits the movement of dislocations. At a certain point the spacing between the precipitates becomes larger, enabling the dislocation to move between the precipitates, with a decrease of the hardness as a result. The maximum hardness is achieved when a combination of θ" and θ' precipitates are present. After the maximum has been reached the hardness only decrease further due to the increasing distance in the precipitates. Overageing starts when the ageing procedure goes beyond the maximum hardness.

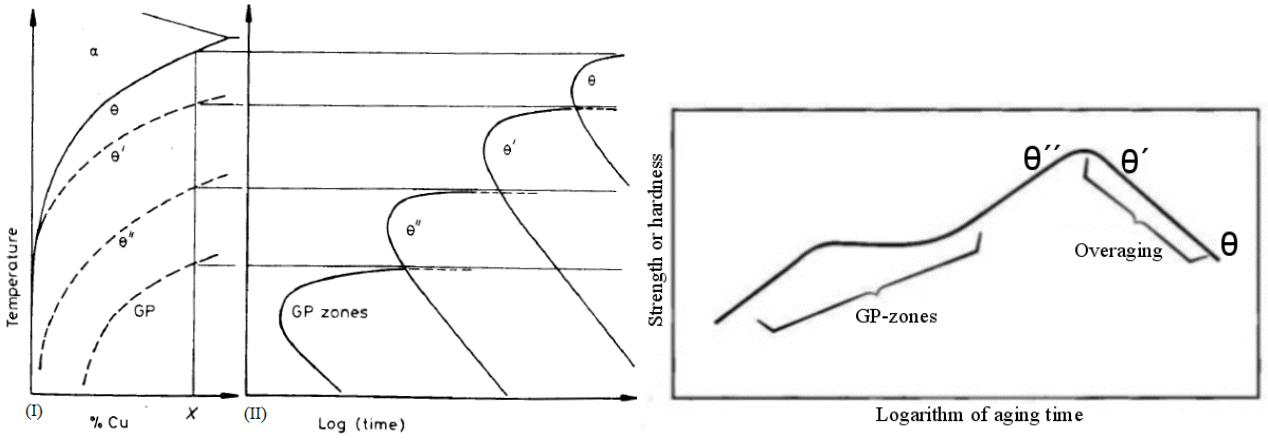

(a) (b)

Figure 2.4: *(a)(I) The meta stable solvus lines in Al-Cu (schematic). (II) Time for start of precipitation at different temperatures for alloy X in (I) [17]. (b) The effect of the AlCu precipitates phases on the hardness and strength when it is artificiality aged above the GP-zone temperature [20].*

So far it has been assumed that the aluminium 2024 alloy is obtained through direct ageing after quenching, which is the case for the T4 condition. In the T351 condition the alloy is stress relieved by stretching 1-3% prior to ageing [21]. The strain introduced by the stretching causes a finer precipitate dispersion resulting in an increase of strength. However, the toughness can be adversely affected by the type of temper. In Figure 2.5(b) [8] the effect of the temper on the strength and toughness is shown on aluminium 2024. Both the T351 and T4 conditions acquire maximum strength in approximately four to five days, after those days the influence of further natural ageing is of relatively minor magnitude[17].

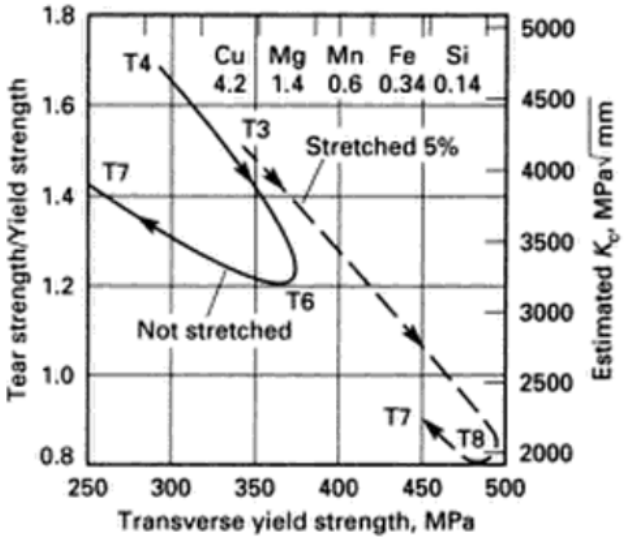

Figure 2.5: *The effect of the AlCu phases on the hardness and strength when it is artificiality aged above the GP-zone temperature [8].*

Effect of peak temperatures

So far the only heating that was considered was relatively long in time duration in the form of natural or artificial ageing. This was well suited to explain the behaviour of the precipitates as the long time period gives the precipitates all the time needed to mature in their respective phase. However, when SSAM is applied, the local heating of the material is in order size of seconds instead of hours/days used for artificial and natural ageing. Thus resulting in peak temperatures that could create a different phase ratio than has been found in literature so far. Y.T. Sato et al. [14] examined the effect of peak temperatures on the hardness and precipitates, using small aluminium 2024 T4 specimen heated to a peak temperature within 50 s, kept at that temperature for 3 s, and then cooled to less than 150°C within 20 s to 30 s, as shown in Figure 2.6 (a). The peak temperatures varied from 177°C to 504°C. Temperatures lower than 177°C showed no difference in comparison to the parent material and have therefore not been investigated any further.
The relationship between peak temperature and hardness is shown in Figure 2.6(b). The specimens exhibited roughly the same hardness as the parent material when peak temperatures were lower than 177°C, between 254°C and 354°C, and higher than 456 °C. On the other hand, hardness reductions were seen at peak temperatures between 223°C-233°C and 382°C-430°C.

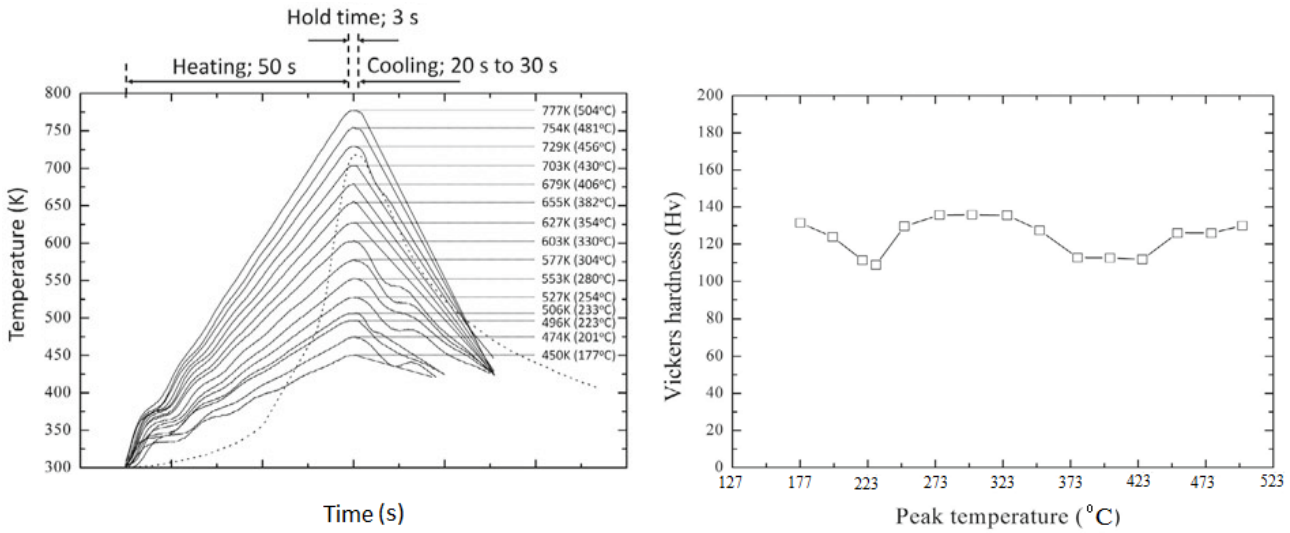

(a) (b)

Figure 2.6: *(a)Thermal history during FSW in the stir zones (dotted line) and thermal hystereses simulated in AA2024 parent material (solid lines)[14]. (b)The hardness of aluminium 2024-T4 when subjected to a peak temperature range to simulate the welding condition[14].*

Yield stress of aluminium with increasing temperature and strain rate

Not only the properties of the aluminium as a result of the SSAM process are of interest, but also the properties during the process are interesting and important. In Chapter 4 a model for the prediction of the heat transfer during the SSAM process is made. For this the properties of the aluminium versus the temperature and strain rate must be mapped. This subsection is devoted to the mapping of flow stress.

Lipski et al. [22] investigated the effect of temperature on the properties of the 2024-T351 for a range of 25 to 200 °C. Furthermore J.D.Seidt et al. [23] studied the effect of the strain rate and for a few different temperature values. But the information is insufficient to map the behaviour aluminium versus the temperature and strain rate. In the previous subsection it was found that the increase of mechanical properties decreases again, once the temperature of the ideal ratio of precipitates θ" and θ' is past. This means that for the 2024-T351 alloy, a high increase of heat not only allows easier movement of dislocations but also permanently reduce the flow stress of the material. This allows the behaviour of the mechanical properties of 2024-T351 for higher temperatures to be modelled as 2024-O, that has been broadly studied by Y.V.R.K. Prasad et al. [24]. It is therefore assumed that for temperatures higher than 300 °C the yield flow stress behaves the same for a 2024-T351 as for 2024-O, the result is shown in Figure 2.7(a). The steep decrease in the figure models the behaviour of the material that goes past the ideal ratio of precipitates θ" and θ'. In Figure 2.7(b) the behaviour of flow stress versus the strain rate is plotted. The material shows a shear thinning behaviour.

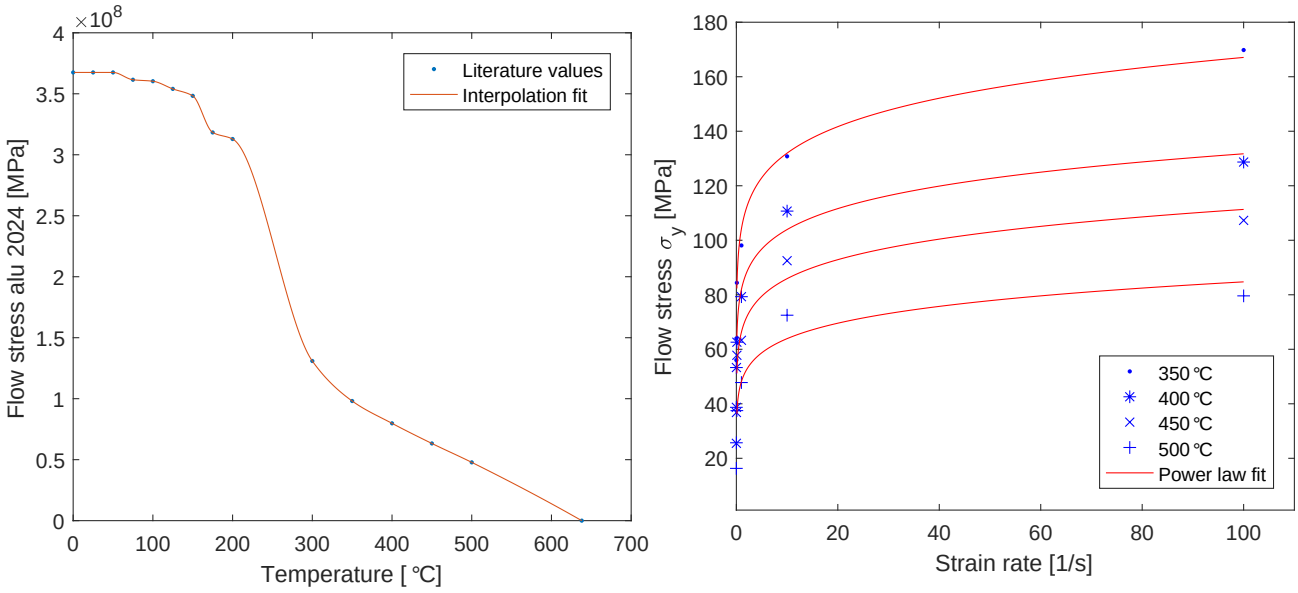

Figure 2.7: *(a)Flow stress versus the temperature at a strain rate of $100s^{-1}$, (b) Flow stress versus the shear rate. Note: the shear thinning behaviour of aluminium 2024.*

2.2 Friction surfacing

In the experiments a FS setup is proposed. FS is a solid state process based on the plastic deformation of a metallic mechtrode. Figure 2.8 shows the video captures, the measured torque, applied force on the mechtrode and the displacement along the mechtrode direction axial direction for a FS process. J. Gandra et al. [25] divided the process in two main stages: (i) an initial deformation period and (ii) deposition.

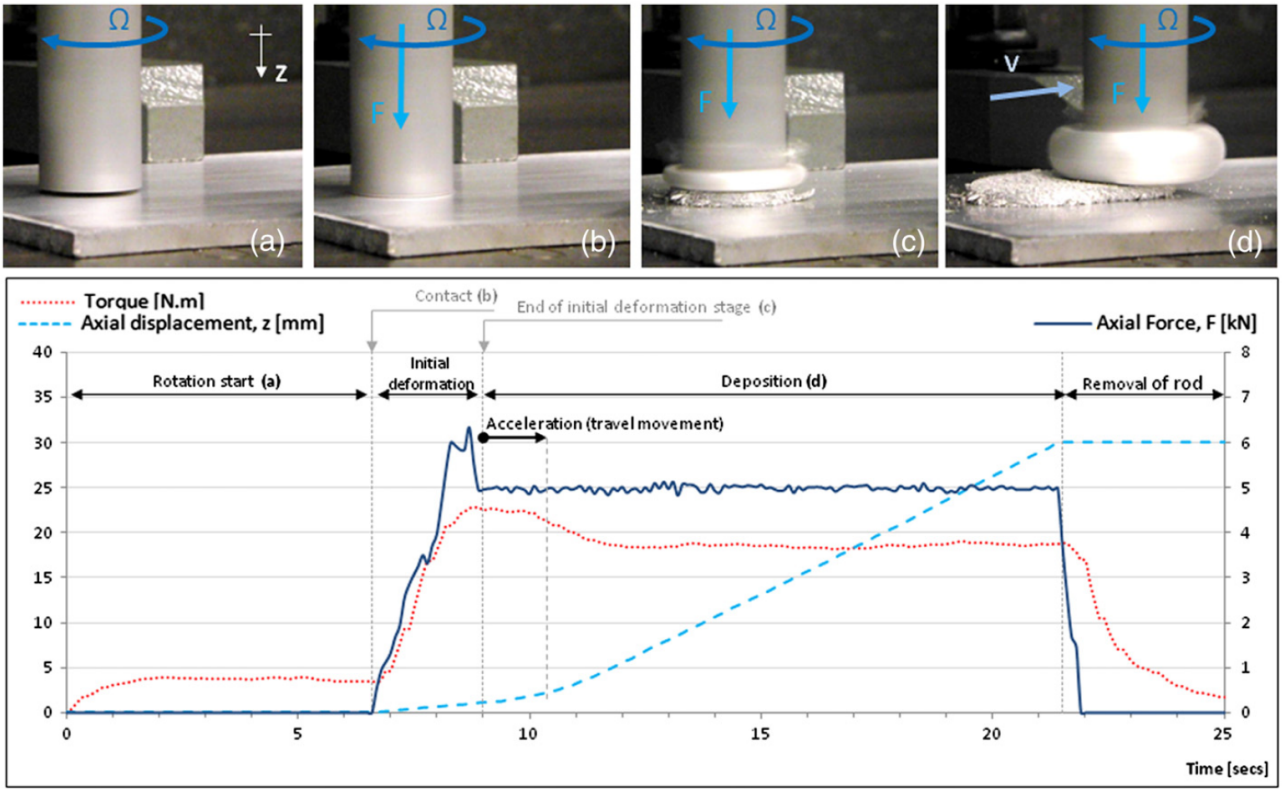

Figure 2.8: *Friction surfacing of an AA6082-T6 aluminium alloy over AA2024-T3 shown with video captures and registered evolution of torque, applied force on the consumable rod and the displacement along the consumable rod axial direction. (a) Rotation start, (b) initial contact, (c) initial deformation stage and (d) deposition stage[25].*

The process starts with a rotating mechtrode, Figure 2.8 (a). When the mechtrode is up to speed it is pressed against the substrate, starting the initial deformation period, Figure 2.8 (b). The contact causes a sharp increase in the measured force and torque.
The heat generated from the friction process causes the mechtrode to soften and lowers the measured force and torque. When enough heat is generated the mechtrode will bond to the substrate and form a deposit, Figure 2.8 (c). The main heat source shifts from interfacial friction to plastic deformation. The deposition period is then started. The plasticized material at the tip of the mechtrode is pressed against the substrate without lateral restraint, flowing outside the mechtrode diameter region. This causes the development of a revolving flash as well as the lack of bonding at the coating edges, as described by Nicholas and Thomas[26]. The mechtrode starts to translate when enough deposit has been reached, Figure 2.8 (d). The deposit will bond over the substrate creating a 3D product The translation allows the measured force to instantly stabilize. The torsion has a small delay but eventually also stabilizes. Note that FS relies solely on interfacial friction and plastic deformation for heat source, because the heat generated by friction dissipation tends to zero as the material gets near the fusion temperature the maximum temperature achieved within processed zone is physically limited by the fusion temperature and thus all the deformation is restricted to solid state condition [5].

In literature this process is already a broadly studied subject with different materials. A. van Kalken [27] showed that the deposition of stainless steel on mild steel is possible through wide operation window of FS. J. Gandra et al. [28] did a performance analysis of friction surfacing of mild steel, for a range of parameters. They investigated the influence of forging force, the mechtrode tilt angle, travel and rotation speeds on interfacial bond properties and the process efficiency. In the study of M. Shariq [29] this is extended to feasibility of FS on non-ferrous substrates. He showed the possibility to use FS to clad stainless steel (AISI 304) on an aluminium (AA1050A) substrate. A start-up plate of another material was needed to bring the rod on a sufficient temperature to enable deposition. In other studies of J. Gandra et al. [25][30], the mechanical and wear characterization and the influence of process parameters in the friction surfacing of AA 6082-T6 over AA 2024-T3 have been determined. So far most of these studies have been focussing on adding a clad layer with enhanced properties, e.g. applying AA6082-T6 over AA2024-T3 to improve the corrosion resistance of the material. The research of using FS for AM is limited and according to the authors knowledge depositing AA2024-T351 onto AA2024-T351 has not been researched yet. Also all of the research found has been focussing on the steady state part (the deposition of the mechtrode), concluding there is still a gap of knowledge on this process for similar materials and the start-up.

FS model

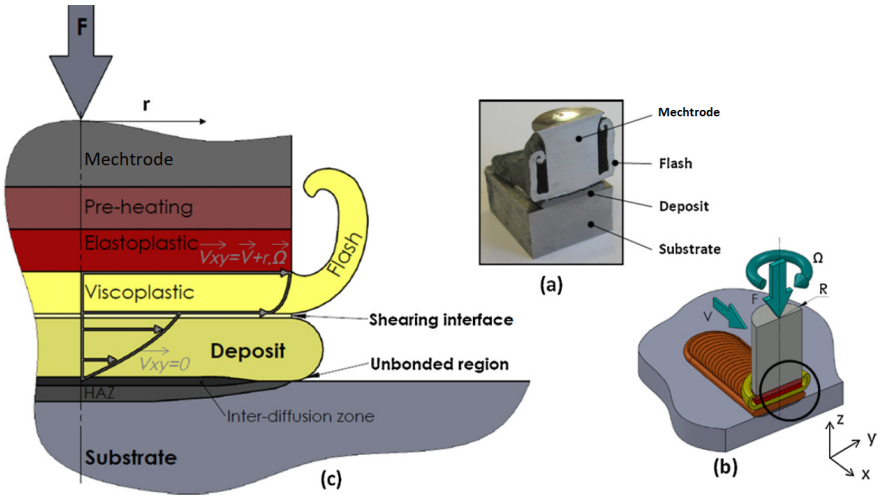

Figure 2.9: *Thermo-mechanics of friction surfacing. (a) Sectioned mechtrode, (b) process parameters and (c) thermo-mechanical transformations and speed profile. F forging force; ω rotation speed; v travel speed and V_{xy} speed resultant in-plan xy given by composition of rotation and travel speeds[28].*

J. Gandraa et al. [28] proposed in their study a model for the global thermal and mechanical processes involved during friction surfacing, based on the metallurgical transformations, shown in Figure 2.9. They divided the cross section in several zones. The mechtrode zone, in this the material was unaffected by the process. The pre-heating zone, in this zone the microstructure of the mechtrode material is effected by the heat that is produced by the process. The elastoplastic zone, this zone is thermo-mechanically effected by the process.

The viscoplastic zone, this zone is thermo-mechanically effected but also produces the flash. The deposit, The material that is added to the substrate. The heat affected zone (HAZ), the zone of the substrate that is affected by the heat of the process. And finally the substrate, the unaffected part of the substrate.

The model shows that the detachment of the deposit is caused by the speed difference of the viscoplastic material that is rotating along with the rod at v_{xy}, and the material joined to the substrate (v_{xy}=0). The deposit material has no lateral confinement, resulting into a revolving flash attached to the tip of the mechtrode. Hence, the most significant heat source is the viscous shearing friction. The flash and unbonded regions function as boundary conditions of temperature and pressure for the joining process.

FS hardness distribution

According to J. Gandraa et al. [25], the thermo-mechanical events experienced by the mechtrode during friction surfacing are reflected by the hardness profile, as depicted in Figure 2.10. The frictional forces force between the mechtrode and the substrate generate heat that is conducted through the mechtrode, this preheats the material that facilitates the plastic deformation in a compression/torsion process. In the mechtrode's HAZ hardness drops due the loss of the T6 heat treatment. The hardness increases in the thermal mechanically affected zone (TMAZ) and the friction zone(FZ) due to strain hardening and grain refinement. The FZ presents a finer microstructure, but still has a 15% lower hardness than the original material due loss of the T6-heat treatment. The profile also show a 2mm deep HAZ of the substrate.

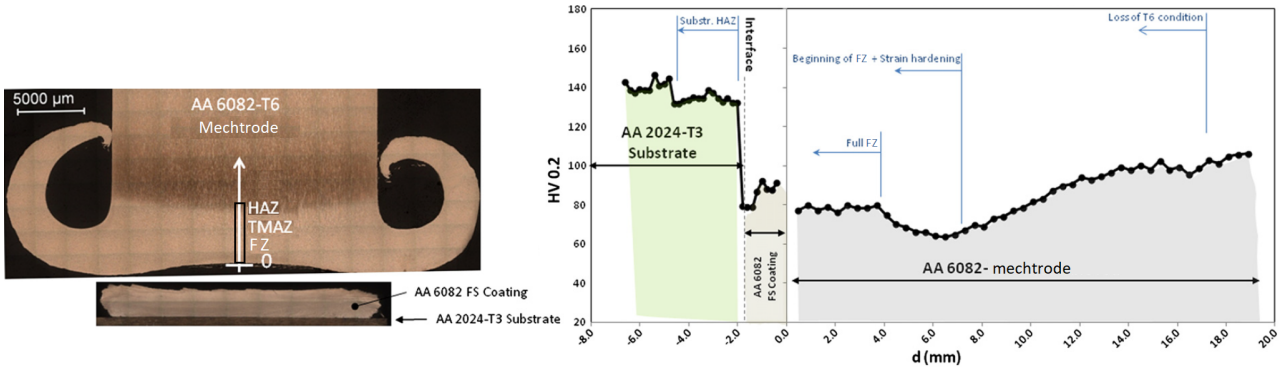

Figure 2.10: *The coating cross section and hardness profile along the mechtrode.[25]. Note the black he black rectangle indicates the EBSD map*

2.2.1 FS microstructure

U. Suhuddin et al. [31] analysed the microstructural evolution during FS of AA6082-T6 mechtrode on an AA2024-T351 substrate using the electron back scatter diffraction(EBSD) technique. They defined three microstructural zones in the mechtrode material: the unaffected base material(BM), the TMAZ and the friction zone (FZ). A EBSD map obtained from the mechtrode material is shown in Figure 2.11. The map was taken respectively from each zone shown as a black box in Figure 2.10. The EBSD map is divided in three microstructural regions respective to the three defined zones.

The high-magnification of region 1 is shown in Figure 2.11(b). In region I the boundaries of the grains are preferentially aligned in the longitudinal direction of the substrate. The geometrical strain requirement forces the parents grains to be sheared in a common direction. Region 2 shows the grains are reorientated almost parallel to the substrate surface see Figure 2.11(c). The thickness of the grains has been substantially reduced, approaching subgrains size sometimes. Indications of a temperature increase have been found, shown by wavy grain boundaries. Several cases showed the serrated boundaries come close to each other, causing the subdivision of thin, elongated grains into strings of nearly equiaxed grains, an example is circled in Figure 2.11(c). A behaviour that is similar to the definition of geometrical recrystallisation. But the grains are to thick for such a process. Therefore it is thought that the contribution of geometrical recrystallisation is not very high. Region 3 shows many fine grains and the course grains are almost entirely disappeared, see Figure 2.11(d). The leftover course grains typically have a irregular shape and have a developed subgrain structure, see high magnification insert.

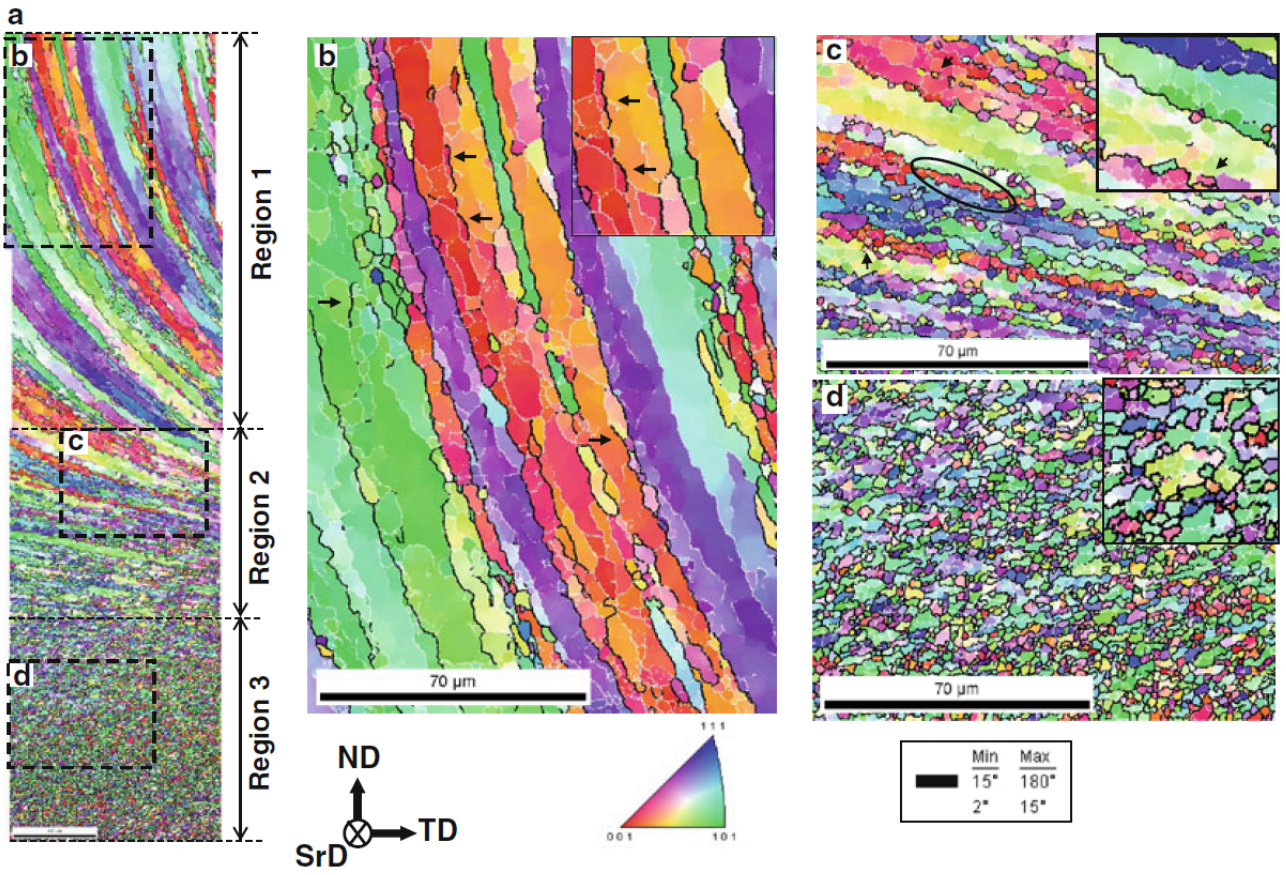

Figure 2.11: *An EBSD map taken from the mechtrode material AA6082 (a). With selected areas shown at high magnification in; BM(b), TMAZ(c) and FZ(D). On the map individual grains are coloured according to their orientation relative to the surfacing direction; a color-coded triangle is shown in the bottom part of the figure.*

Influence of the process parameters on FS

The parameters such as the mechtrode's axial force and rotation speed influence the quality of the bonding. One of the indicators of the quality of the bonding is bonded width, this is the width of the bonding between the deposit and the substrate without voids or gaps, see Figure 2.12). Another point of interest is the bonding thickness, that is the average measured thickness of the bonding.

J. Gandra et al. [30], studied the influence of the mechtrodes axial force and the rotation speed on the bonded width, the width and the thickness. It was found that the axial force improves the bonding width and results in wider and thinner deposits, as shown in Figure 2.14(a). Insufficient axial forces result in poor consolidated interfaces, with a decrease on the bonded width, see Figure 2.13(a). The decrease in thickness for higher axial forces was also followed by concave shaped cross sections and enhanced substrate heat affected zones, see Figure 2.13(b). Excessive forces can also result in the depression of the substrate surface as evidenced in Figure 2.13(b). Rotation speed influences the bonding quality and coating width 2.13(b). While lower to intermediate rotation speeds enhance bonding quality, higher rotation speeds produce a more flat and regular deposit.

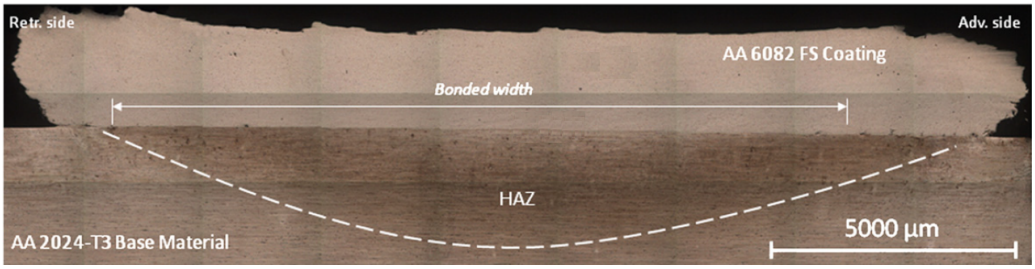

Figure 2.12: *Coating cross section macrograph. Note the defined bonded width[25].*

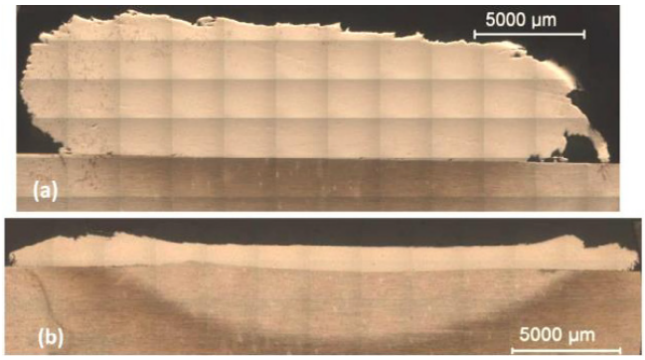

Figure 2.13: *Influence of axial force and rotation speed on coating cross section and substrate HAZ; (a) 5kN, 1500 rpm, 4.2 mm/s; (b) 9 kN,3000 rpm, 4.2 mm/s[30].*

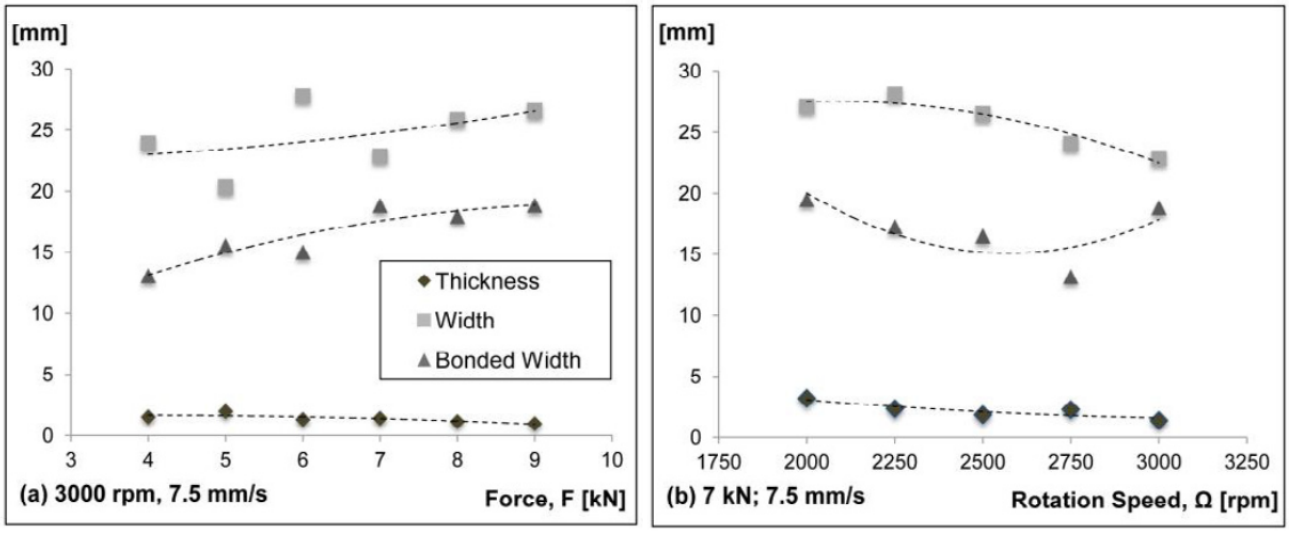

(a) (b)

Figure 2.14: *Effect of force and rotation speed on coating thickness, width and bonded width[30].*

2.3 Analytical models of the heat input

For a true understanding of the bonding mechanism between the substrate and the mechtrode, it must be known how the heat is generated. For FS no model that is able to predict the heat generation of this process has been found in literature. However, for FSW two types of heat prediction models are known. The first is a model for a surface heat source, the second a volumetric heat source. Based on the observations of the experiments and considering the mechtrode does not plunge in the material, as the FSW tool does, the generation of heat in starting phase of FS is assumed to be surface heat source.

Lohwasser [32] and Schmidt [33] suggest for the FSW process a surface heat source that is based on the constitutive behaviour for the force equilibrium between the tool and workpiece. They suggest that there are are two contributions to the heat generation: (i) frictional dissipation and (ii) plastic or viscous dissipation. The frictional dissipation is driven by the frictional stress field at the contact interface. In their model the whole geometry of the rotation tool i.e. the shoulder, probe and probe tip, is included. The situation for FS is simpler and therefore in the derivation one can assume a tool with only a flat shoulder. The following assumptions were made for the derivation of the heat flux of the FS starting phase:

- An uniform contact shear stress $\tau_{contact}$ was assumed.
- The sliding condition of the shearing takes place at the contact interface.
- Other mechanism of heat generation, such as deformation were not considered.

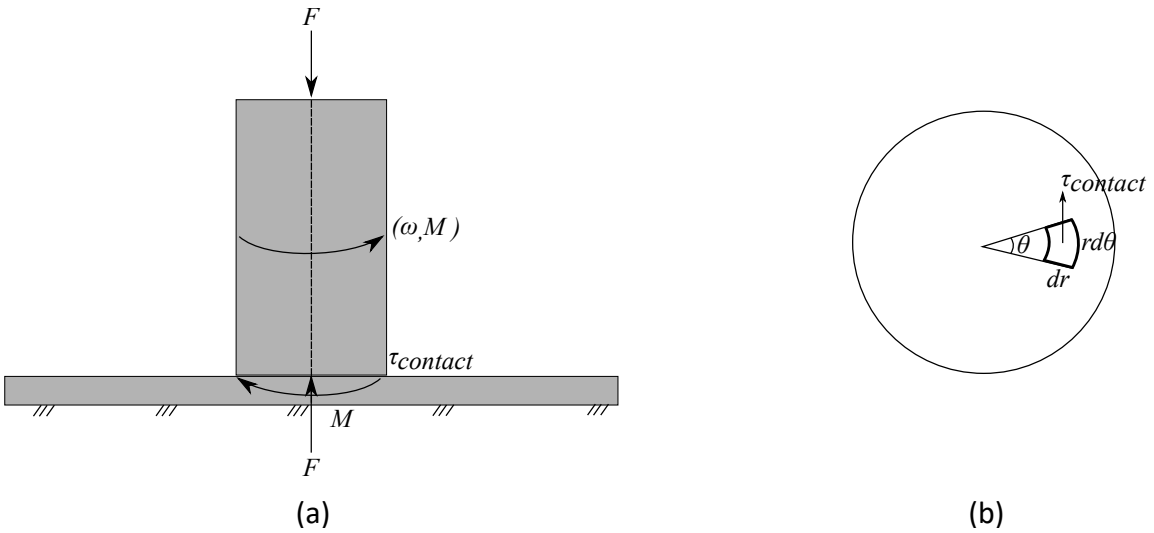

Figure 2.15: *(a) The mechtrode with axial force F and rotation speed ω transfers the torque M to the substrate through a contact stress between the mechtrode and the substrate. (b) Schematic drawing of the contact stress applied at the interface with infinitesimal segment areas.*

To calculate the heat generation from the mechtrode surface, an infinitesimal segment on that surface is investigated, see Figure 2.15. The infinitesimal segment area dA = r dθ dr is exposed to an uniform contact shear stress $\tau_{contact}$. This segment contributes with an infinitesimal force of dF = $\tau_{contact}$ dA and torque of dM = r dF. The heat generation from this segment is:

$$dQ = \omega dM = \omega r dF = \omega r^2 \tau_{contact} d\theta dr, \tag{2.3}$$

where r is the distance from the investigated area to the centre of rotation, and r dθ and dr the segment dimensions. Integrating over the contact surface of the mechtrode gives:

$$Q = \int_0^{2\pi} \int_0^R \omega r^2 \tau_{contact} dr d\theta = \frac{2\pi}{3} \omega R^3 \tau_{contact}. \tag{2.4}$$

Equation 2.4 is based on the general assumption of a constant contact shear stress as mentioned before, but the mechanisms behind the contact shear stress vary depending on whether the sliding or sticking condition is present. A distinction is made between three types; full sticking, full sliding and partial stick/sliding at the surface interface. For the full sticking state it is assumed that the contact stress, due to static friction, is higher than the material shear yield stress. The mechtrode fully sticks to the substrate and therefore $\tau_{contact}$ is defined by the shear stress of the weakest material.

$$Q_{stick} = \frac{2\pi}{3} \omega R^3 \tau_{yield}. \tag{2.5}$$

The Von Mises yield criterion is used to estimate the shear stress with respect to the yield stress

$$\tau_{yield}(T) = \sqrt{\frac{\sigma_{yield}(T)^2 - \sigma_{33}^2}{3}} = \sqrt{\frac{\sigma_{yield}(T)^2 - (\frac{F}{\pi R^2})^2}{3}}, \tag{2.6}$$

where σ_{yield} is the yield stress of AA2024 shown in Figure 2.15 and F the axial(normal) force. Implementing the Von Mises yield criterion in heat flux for sticking gives equation 2.7.

$$Q_{stick} = \frac{2\pi}{3} \omega R^3 \sqrt{\frac{\sigma_{yield}(T)^2 - (\frac{F}{\pi R^2})^2}{3}}. \tag{2.7}$$

For the full sliding state it is assumed that no plastic deformation is caused in the substrate due to the rotation of the mechtrode. The contact stress is lower than the material shear yield stress. In this case, the Coulomb law of friction is applied to describe the shear forces at the interface. In general, the law estimates the contact shear stress as:

$$\tau_{contact} = P\mu = \sigma_{33}\mu = \frac{F}{R^2\pi}\mu, \tag{2.8}$$

Where μ is the dynamic friction coefficient, and P and σ are the contact surface pressure. Implementing the Coulomb law of friction in equation 2.4 results in:

$$Q_{slip} = \frac{2\pi}{3}\omega R^3 \sigma_{33}\mu = \frac{2}{3}\omega RF\mu. \tag{2.9}$$

The partial stick/sliding is a combination of the previous two. In this situation the matrix segment accelerates to a velocity less than the tool surface velocity, where it stabilizes. The equilibrium establishes when the dynamic contact shear stress equals the internal yield shear stress due to a quasi-stationary plastic deformation rate. This is referred to as the partial sliding/sticking condition. In order to do this a slip parameter is defined as:

$$\delta = \frac{\nu_{matrix}}{\nu_{tool}}. \tag{2.10}$$

Combining this with the previous equations of heat flux of slick and slip gives the following stick/slip equation:

$$Q_{stick/slip} = \delta Q_{stick} + (1-\delta)Q_{slip} = \frac{2\pi}{3}\omega R(\delta\sqrt{\frac{\sigma_{yield}(T)^2 - (\frac{F}{\pi R^2})^2}{3}} + (1-\delta)\sigma_{33}\mu), \tag{2.11}$$

Note when δ= 1 the equation changes in the stick equation and similar for δ=0 the equation changes into the slip equation. In practise δ may change value during the start-up phase and may also be dependant on r.

Chapter 3

Experimental study

3.1 Introduction

This chapter is dedicated the experimental setup of this study. The aim of this study is to create an understanding of the bonding process and to find the parameters that give the optimal bonding. The aim of this study will be investigated using a FS experimental setup. For the experiments it was chosen to analyse three parameters sets: the rotation speed, the axial force and the substrate temperature. The rotation speed set varied between 450, 600 and 900 RPM and was performed at an axial force of 5kN till the maximum substrate temperature was reached. The axial force set varied between 5kN to 12.5kN and were performed at rotation speed of 450RPM till a maximum substrate temperature of 330 °C was reached. Some arbitrary higher axial forces of 14, 18.5 and 25kN were tried but for a single time, a whole data set like the previously stated range was left out for these axial forces due to a limited time frame. The substrate temperature set varied from the start of the bonding at approximately 230 °C to the maximum temperature of 350 °C with a temperature step of 20 degrees, and was performed at rotation speed of 450 RPM and an axial force of 5kN.

This Chapter will start with an explanation of the experimental setup in section 3.2. In section 3.3 the experimental procedure, the result of the parameter sets and the data processing is shown. Finally the results of the experiments are discussed in section 3.4.

3.2 Experimental setup

In the experimental setup an aluminium substrate was placed in an arm that was able to rotate freely, see Figure 3.1 (a) and (b). Clamps were used to properly fix the substrate to the arm. This arm had three thermocouples installed that were able to measure the temperature distribution of the substrate bottom along the radius of the mechtrode. A mechtrode of aluminium was pressed on the substrate with force F that was measured in a load cell. When the mechtrode started to rotate, the frictional/shear forces caused a torque in the arm. The torque was measured with the second load cell that prevented the arm from rotating. The arm was mounted on a press that had a constant pressure. The constant pressure was needed to ensure a constant contact between the the mechtrode and the substrate once enough heat was generated for the mechtrode to plastically deform. Subsequently the press was mounted in a ball bearing setup that enabled the setup to rotate freely. Finally the ball bearing housing was fixed on a plate that enabled the whole setup to be mounted on a machine table.

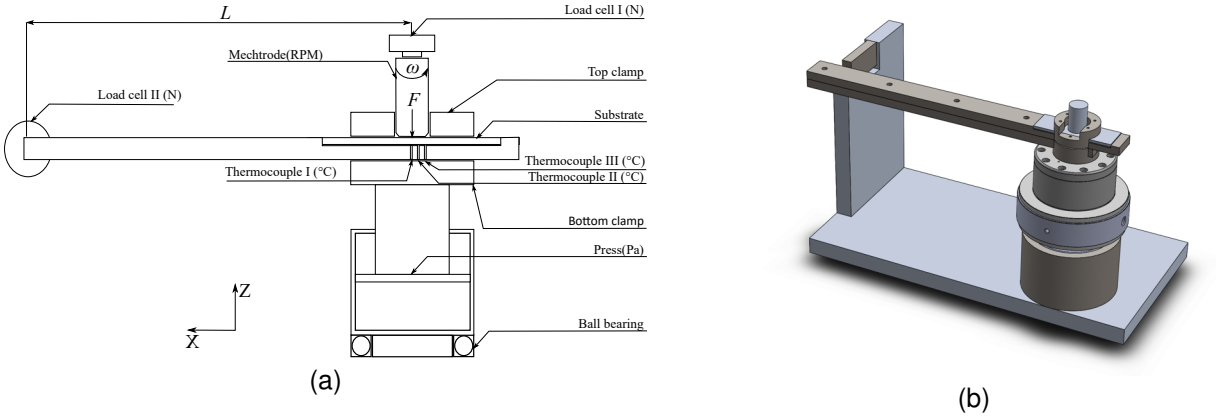

Figure 3.1: *(a) Schematic overview of the experimental setup with the billet/mechtrode pressed on the substrate with force F and rotation speed ω. (b) Cad impression sketch of the experimental setup. Note the free space in the top clamp. This was used to record the process.*

The experiments were carried out on a modified planer machine equipped with a 13 kW motor, see Figure 3.2. The mechtrode of Figure 3.1 was connected to the motor via an adapter. The machine allowed rotation speeds ω between 450 and 1500 RPM and a normal force F up to 50 kN. The experimental setup was first aligned with the axis of the motor before the flat plate was clamped on the machine table. For the substrate and mechtrode aluminium 2024 T-351 was used. The substrate and mechtrode were cut with a hardened steel

saw with coolant. The substrate were cut in sections of 90x30mm from an aluminium plate with a thickness of 4mm with the roll direction along the long axis. The protection film was left on the substrate until it was mounted on the arm. The mechtrode was cut from a rod with a diameter of 20mm at a length of 50mm. A flat surface of 33mm long was milled to fit the mechtrode in the adapter and to fixate it in the z-rotation-direction. Some of the mechtrodes were tapped with 12M thread for tensile test, see chapter 5.

(a) (b)

Figure 3.2: *(a) The modified planer machine that was used for the experiments,(b) the fixation of the experimental setup. Note this is an old picture, the recording gap near the mechtrode in the clamp shown in the cad impression was implemented in later experiments.*

3.3 Experimental procedure and data filtering

The procedure started with the recording of all the data in Labview 2014. After that the mechtrode was pressed with starting axial force F_0 on the substrate. When sufficient force was reached the motor was powered by the operator to rotate the mechtrode with the predefined rotation speed ω. This caused a torque in the substrate and was registered by the load cell. The operator stopped the experiment when the predefined substrate temperature T_{sub} was reached. When the motor was stopped the mechtrode made a few more rotations, depending on the initial rotating speed, to stop the rotor of the motor that was still rotating due to inertia.

The tested parameter sets were divided in three different sets: the rotation speed Table 3.1, the axial force Table 3.2 and the substrate temperature set Table 3.3. For the rotation speed set the experiments were performed with different rotational speeds. The starting force was kept at 5 kN and the experiment ran until a maximum substrate temperature was observed at the thermocouple with the highest temperature, that was thermocouple I at a temperature of approximately 340 °C. After the experiments of the rotation speed set the thermocouples had to be replaced and the mechtrode was set differently in the adapter for easier reloading of the mechtrode. Consequently, the following experimental sets are not directly comparable and the different

Table 3.1: *Rotational speed data set*

Test	ω(RPM)	F_0(kN)	T_{sub}(C°)	Post test
1	900	5	340	T
2	900	5	340	T
3	900	5	320	T
4	900	5	320	T
5	900	5	280	T
6	900	5	340	T
7	900	5	320	T
8	900	5	320	T
9	450	5	330	T
10	450	5	330	T
11	600	5	315	T
12	600	5	315	T

Table 3.2: *Axial force data set*

Test	ω(RPM)	F_0(kN)	T_{sub}(°C)	Post test
35	450	5	340	T
36	450	5	335	T
44	450	5	350	H
45	450	5	320	T
60	450	5	330	H
50	450	7.5	330	T
52	450	7.5	330	T
53	450	7.5	330	T
59	450	7.5	330	H
55	450	10	330	T
56	450	10	330	T
57	450	10	330	H
54	450	12.5	325	T
58	450	12.5	340	H
43	450	14	380	T
46	450	18.5	390	T
51	450	25	380	T

Table 3.3: *Substrate temperature data set*

Test	ω(RPM)	F_0(kN)	T_{sub}(°C)	Post test
49	450	5	230	H
40	450	5	240	H
48	450	5	240	T
47	450	5	245	T
39	450	5	270	T
41	450	5	280	H
42	450	5	280	T
37	450	5	300	H
38	450	5	300	H
45	450	5	320	T
60	450	5	330	H
61	450	5	330	T
36	450	5	335	T
35	450	5	340	T
44	450	5	350	H

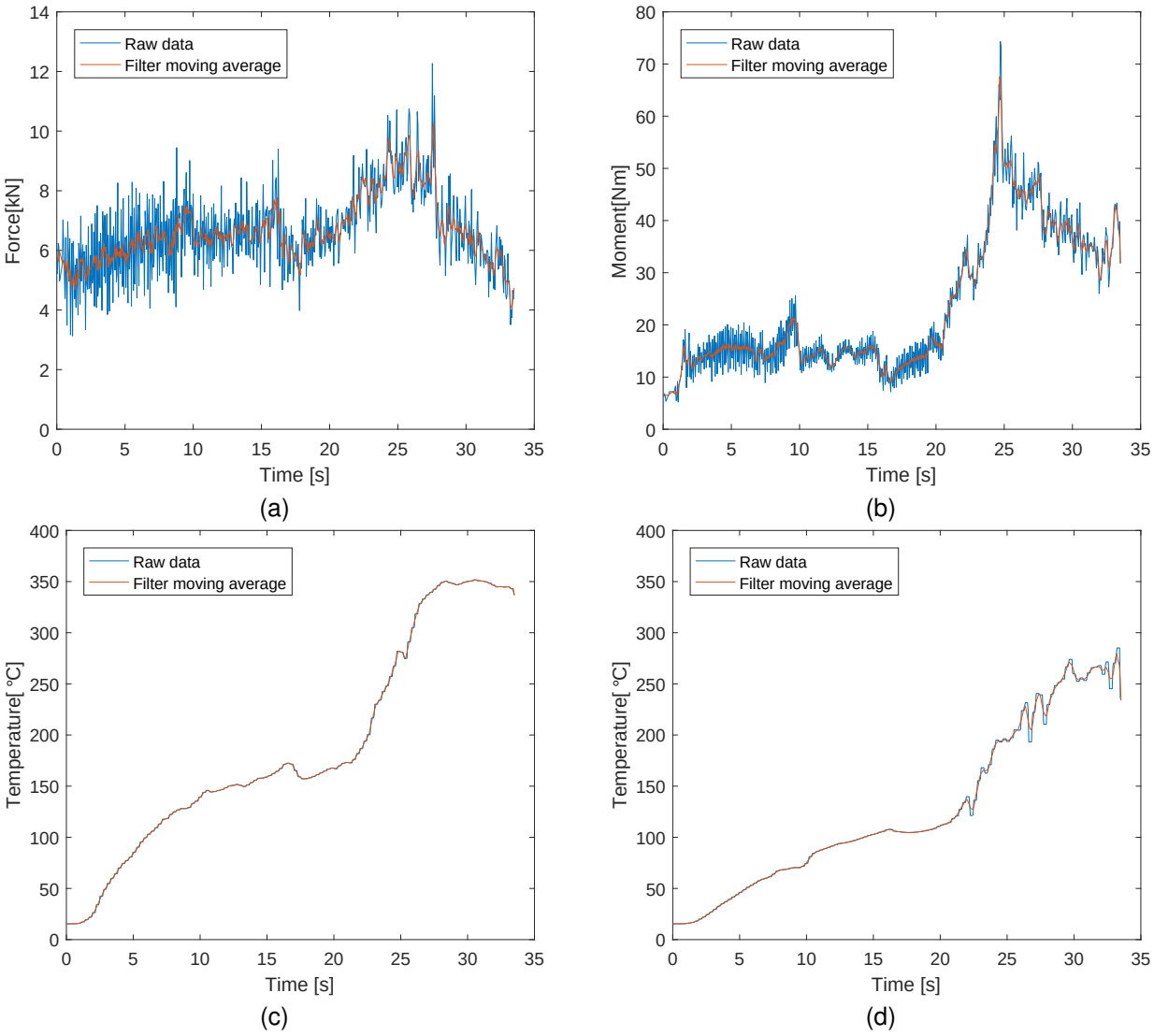

Figure 3.3: *Raw data vs filtered data using a moving average as filter:(a) Force, (b) Torque, (c)Temperature inside Thermocouple, (d)Temperature outside Thermocouple*

conditions should be held into account when the sets are compared to each other.

In the axial force set the experiments were performed with different starting axial forces F_0. For most of the experiments the maximum substrate temperature was set at approximately 20°C before global plastic deformation was expected at a temperature of 330 °C. This was done to prevent the formation of flash in the samples and the samples could be used for tensile test in Chapter 5. As stated earlier some arbitrary higher axial forces of 14, 18.5 and 25kN were tried but for a single time. In the substrate temperature set the experiments were performed with different maximum temperatures measured at the thermocouple I. Originally this set was meant to take the rotation time in account. However, in the experiments the time the stages took for experiments with the same parameters showed a large scatter. To compare the results of the experiments the substrate temperature was used as a reference instead. A higher surface temperature means that more heat has been put in the mechtrode and substrate. Therefore the results of experiments that showed large scatter of the time scale could still be compared. Note that there is an overlap of experiments between the axial force set and the substrate temperature set. This was allowed because the experiments were performed under similar conditions. After the experiments the sample were divided between micro scope research and hardness test, and the tensile tests. In the tables 3.1, 3.2, 3.3 the microscope research and hardness test were denoted as H and the tensile tests as T.

To filter the raw data several filters were tried i.e. a moving average, Savitzky-Golay, Local regression and Gaussian, eventually the moving average was chosen because the least amount of information was lost while most of the noise was filtered out. To prevent loss of overview the information outside the experiment, that is the information before and after the applied torque, were also filtered out. In Figure 3.3 the effects of the filter are shown.

3.4 Results

In this research a lot of experiments have been performed. In this section Test 44 was used as a reference because this test was operating at parameters that were researched the most in this study. Test 44 was used to explain the process and the phenomena that occurred during testing. Later on, the effect of a higher axial force and the effect of a higher rotation speed will be studied in comparison to the reference. The effect of the different maximum substrate temperatures will be researched in chapter 5 testing because the effect was mainly related to the bonding quality while all the other aspects were already covered in the reference experiment.

The reference experiment

Test 44 was performed with a force of 5kN, a rotation speed of 450 RPM and was stopped after the measured maximum temperature was reached. In Figure 3.4 the registered torque, axial force and temperatures during the test have been plotted as function of time. Snap shots of the video recording have been added at various time step a different phenomena was observed visually.

Based on the evolution of torque, force, temperature and the recordings, this process was divided into four main stages. The process starts in stage I_a, a maximum contact stress between the mechtrode and the substrate reached an equilibrium resulting in a plateau for the torque. The temperature of the mechtrode and substrate were gradually rising. An almost equal build up in the axial force that the press failed to keep constant, is observed. After 20.5 seconds, the process continued to stage I_b, the sound of the mechtrode suddenly changed from squeaky to a grinding noise. The interface temperature had reached its first critical temperature point (T_{cr1}) at which the maximum contact stress rapidly increased. Resulting in a rapid increase of the torque at the same time a small increase of the temperature and force is observed.

At 24.5 seconds, the process entered stage II, the interface temperature reaches a second critical point (T_{cr2}). The start of local plastic deformation at the interface was observed. A small collar appeared at the mechtrode's outer edge and continued growing. The torque gradually decreased with increasing temperature and a constant axial force was observed. The generate heat, was still big enough for the temperature at the thermocouples to rise, but more slowly.

After 27.5 seconds, stage III was reached, macro plastic deformation was seen. The applied torsion and force showed a drop and gradually decreased over time. The inside thermocouple showed an instant levelling. The outside thermocouple shows a few seconds later the same behaviour. Finally the process was stopped manually at 34 seconds, the mechtrode made approximately 2.5 rotation before it was slowed to a halt. The gradual slowing of the mechtrode resulted in a small peak of the torque at the end of the process. The final product of the experiment can be seen in Figure 3.5.

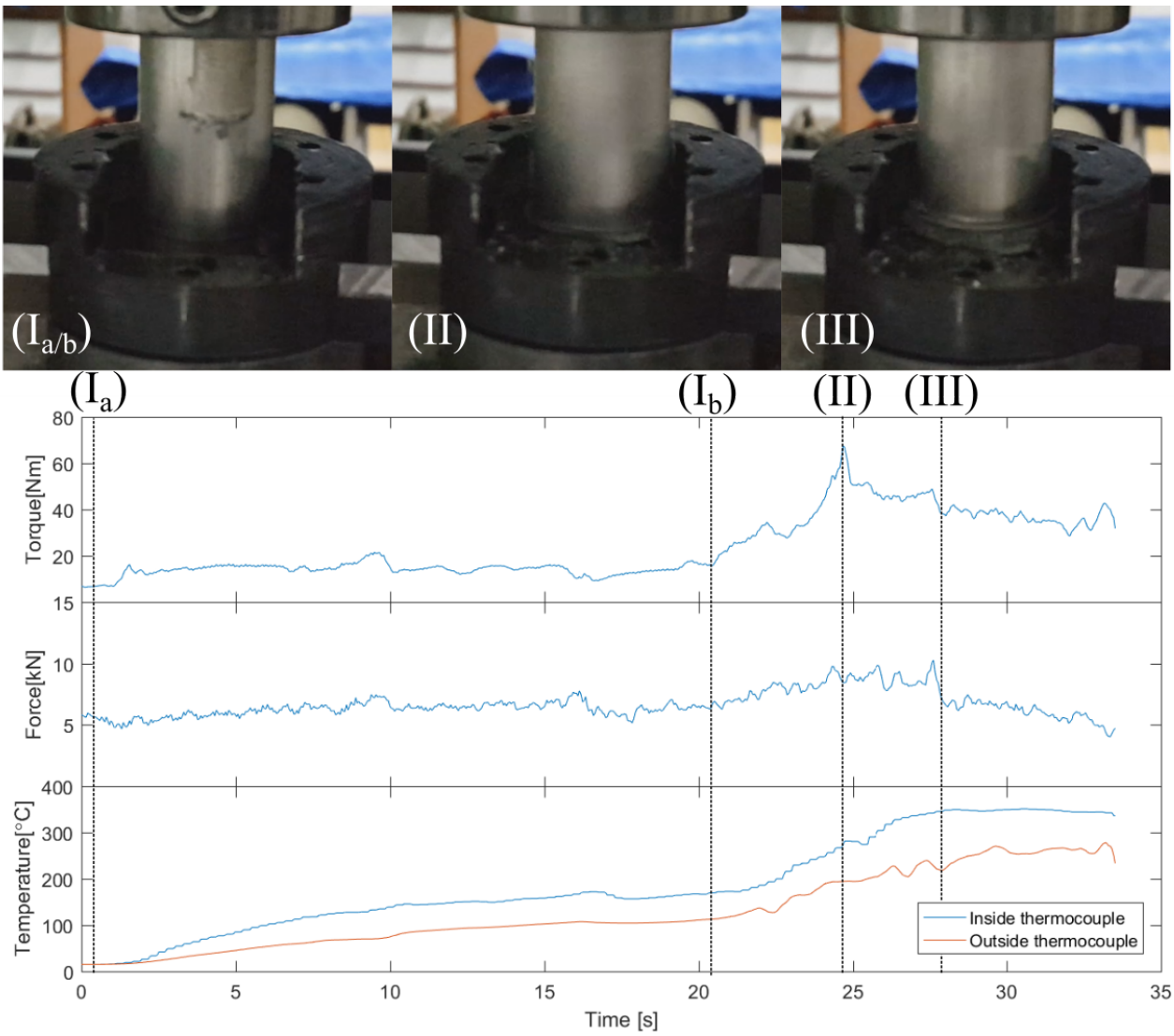

Figure 3.4: *Test 44 force at 5kN, rotation speed at 450RPM and the temperature until the maximum value. Note: the snapshot of stage III is from a later time step to enlarge the deformation area for clarification reasons.*

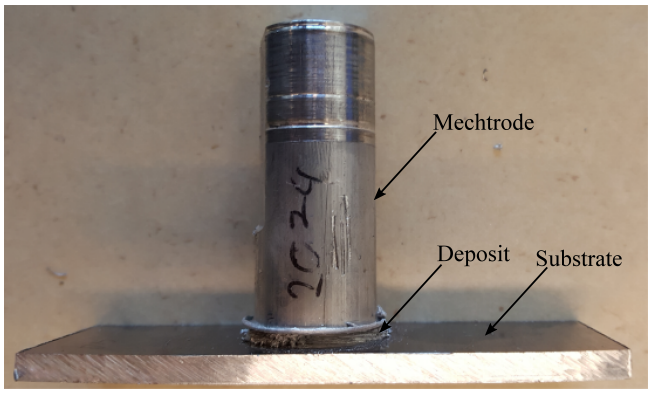

Figure 3.5: *Finished sample of Test 44. Note the deposit between mechtrode and the substrate and the collar that has formed around the edge of the mechtrode.*

The influence of the rotation speed

To present the influence of the rotation speed on the process Test 1, 10 and 12 are used as an example. Note due to the change between the rotation speed set and the other sets, the examples had to be part of the same set. Test 44 could therefore not be used as reference in the investigation of the influence of the rotation speed. Figure 3.6 shows the results of these tests.

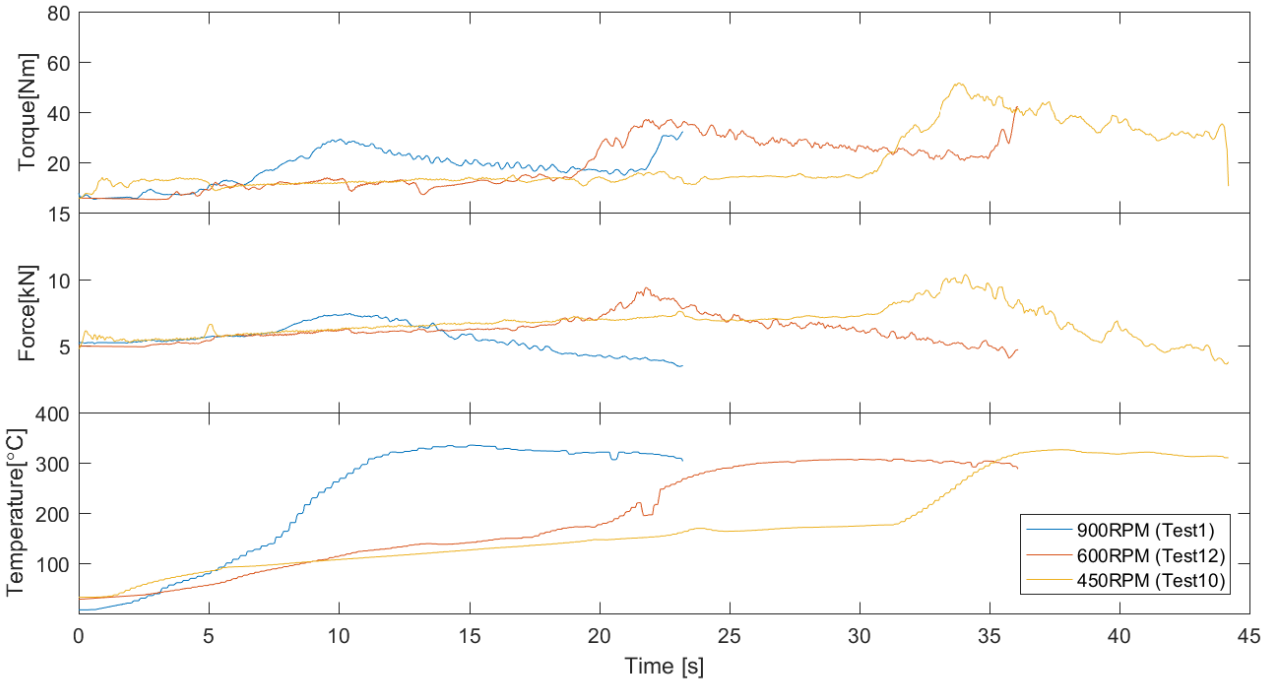

Figure 3.6: *The torque, axial force and temperature of Test 1, 10 and 12 as function of time with F_0=5kN. The experiments were performed past the maximum substrate temperature. Note that all the stages occur in each test.*

Figure 3.6 shows that all stages for each rotation speed are present, but take less time to develop to the next stage. For example stage I_a takes approximately 30, 18 and 5s for a rotation speed of 450, 600 and 900RPM. A higher rotational speed also reduces the maximum torsion, with a maximum torsion of approximately 50, 40 and 35Nm respectively. Finally the maximum force shows a similar drop with a value of approximately 10, 8, 7kN. In Chapter 4 the influence of the rotation speed on the process will be investigated further.

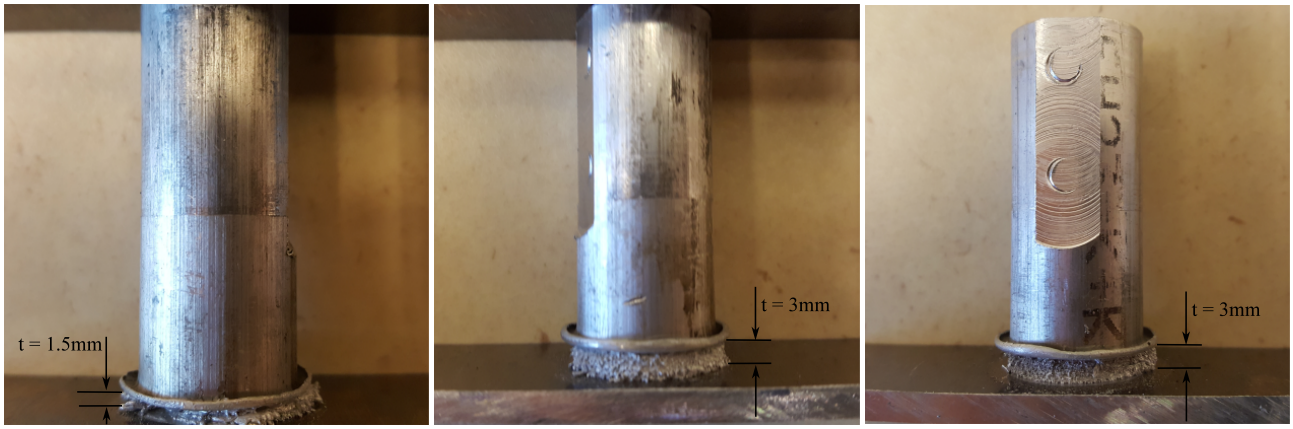

(a) (b) (c)

Figure 3.7: *The sample result of a changing rotation speed: (a) 450 RPM (Test 10), (b) 600 RPM (Test 12) and (c) 900 RPM(Test 1). Note clad layer thickness of (a) in comparison to (b) and (c) is caused by difference of the run time after the maximum temperature was reached and is not related to the rotation speed.*

When the samples were studied in Figure 3.7, the sample of the 450RPM rotation speed showed a lower thickness than the others. The cause of the lower thickness was due to a shorter experimental time after the maximum torque had been reached rather than the difference in rotation speeds, see Figure 3.6. The relation of coating thickness found by J. Gandra et al. [30] of Figure 2.14 in Chapter 2, could not be confirmed in these experiments. Furthermore, no other difference such as the flash or interface structure caused by higher rotation speeds was found.

The influence of the starting axial force

To present the influence of the axial force Test 43, 44, 50 and 51 were used as an example, because these experiments were operated beyond the maximum temperature and therefore gave a clear view of the whole process in comparison to the other tests. Other test with higher axial forces gave the same trend but were left to prevent loss of overview.

Figure 3.8 shows an that increase of F_0 shortens the length of the stages. For example the length of stage I_a is approximately 20.5s for the 5kN test while it is approximately 10s for the 7.5kN test. If F_0 is 14kN or higher, a special situation occurs and stage I_a is skipped entirely, see the 14kN and 25kN test. Higher F_0 also cause a higher torsion peak. In the lower F_0, the axial force increases till stage II is reached, see Test 44 and 50 in Figure 3.8. The force at the 14kN test remains constant till stage II is reached and for higher F_0 the axial decreases from the start of the experiment, see Test 43 and 51 Figure 3.8. Finally higher F_0, cause a higher maximum temperature in the substrate, but also decrease after the maximum has been reached.

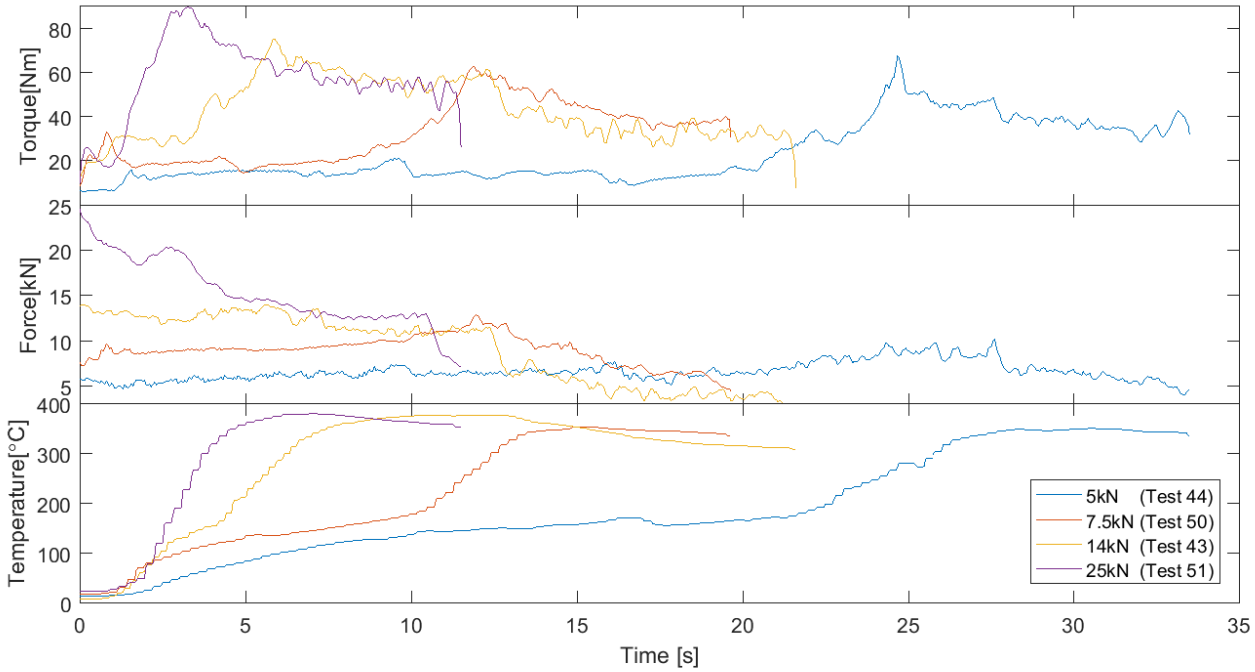

Figure 3.8: *The torque, axial force and temperature of Test 43, 44, 50 and 51 with ω = 450RPM. These experiments were performed past the maximum substrate temperature.*

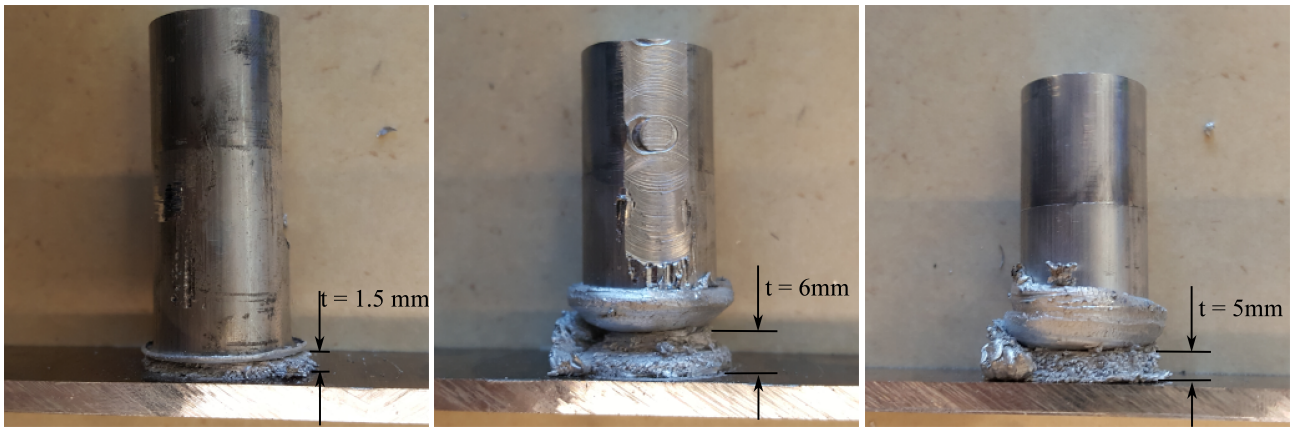

Figure 3.9: *The sample result of changing starting axial force: (a) 7.5 kN(Test 50), (b) 14kN (Test 43) and (c) 25kN (Test 51). Note the difference in clad layer thickness of each sample that is caused by the difference in axial force.*

When the samples are studied in Figure 3.9, a clear distinction could be made for higher F_0 samples. With higher F_0 a greater deposit thickness and a bigger flash was observed. This was not caused by a longer experimental time after the maximum torque had been reached, because the 7.5 and the 25kN F_0 experiment had approximately the same experimental time after the maximum torque had been reached, while still a greater thickness and a bigger flash was observed for the 25kN test. Note the reason that the thickness of the 14kN test is thicker than the 25kN is caused by a longer experimental time after the maximum torque had been reached.

Chapter 4

The thermo-mechanical model

This chapter is dedicated to the thermo-mechanical model. To get a true understanding of the bonding mechanisms a temperature distribution must be known. In the experiments done in previous chapters a series of thermocouples was installed to get a global view of the temperature distribution. However, considering the high heat flux the experiments were operating at, the values of the thermocouples cannot be considered representative for the interface temperature of the mechtrode and the substrate. Comsol 5.2 was used to create a thermo-mechanical model to solve this heat transfer problem. To see if models values are accurate the model has been checked for convergence and a comparison has been made with the analytical solutions in appendix D.
In the first section of this chapter the measured torque input will be used to predict the temperature distribution in the whole sample. The section will start with the conversion of the measured torque into the heat input that is later used in the model. Next the axisymmetric thermo-mechanical model will be introduced. Following with an explanation what type of boundary condition are applied and how the mesh is constructed. After that, the heat input will be implemented as zero and first order heat flux. A control based on the thermocouple measurements will determine the best suited order for the heat flux. Finally the effective radius of the heat flux will be investigated based on a cross section of the test 44 and the simulated temperature of the thermo-mechanical model versus the thermocouple readings. The data of the temperature distribution will later be used in chapter 5 to explain the bonding quality.
The second section of this chapter will focus on the bonding process. This will start with an investigation of the simulated temperature distribution at each stage to explain the phenomena that occur. Subsequently the failure mode of the mechtrode is researched to investigate where and why the material plastically deforms. Following with a investigation in the friction coefficient to see why and when the sticking phenomena occurs. Finally an attempt to predict the heat flux is made by using the analytical equations of H. Schmidt [33] and the findings in previous subjects. The findings will be summarized in a general explanation of the bonding process. The chapter will close off with a conclusion and discussion.

4.1 Prediction of the temperature distribution

Heat input

In chapter 3 test 44 was used as reference. In this section the filtered data of test 44 will be used to generate a heat input. At the test the substrate was fixed to an arm that enabled the measuring of the torque applied on the substrate. Due to the relative small diameter of the mechtrode, the energy that was dissipated through plastic deformation compared to the total work was negligible. Therefore the assumption is made that all work is converted into heat. With the measured torque and equation 4.1 the amount of heat can be determined, as is shown in Figure 4.1.

$$Q_{total} = M \cdot \omega \tag{4.1}$$

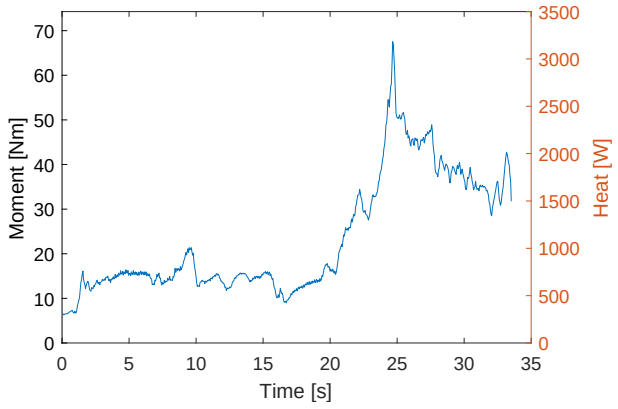

Figure 4.1: *The measured torque converted into heat*

Comsol model

In the thermo-mechanical model the most important parts of the setup have been considered. The model consist out of the mechtrode mounted in the adapter. The mechtrode is in contact with the substrate that is clamped in between clamp part 1 and the arm. The arm is also in contact with clamp part 2. In Figure 4.2 (a) the schematic of the model is shown. Here, 1,3,5,6 are simulated as AISI 1006 Carbon Steel, 2 and 4 are simulated as aluminium 2024-T351. The Arm is not in direct contact with the heat flux and the thermal conductivity of the arm is relatively low compared to aluminium, therefore it is assumed that influence of the axis symmetry, instead of the rectangular shape of the Arm, can be neglected. However these conditions are not the case for the substrate, where the thermal conductivity is high and the substrate is in direct contact with the hear source. To correct this the volume of the substrate in the model is taken equal to the volume of the substrate in reality, resulting in an effective radius of approximately 30mm.

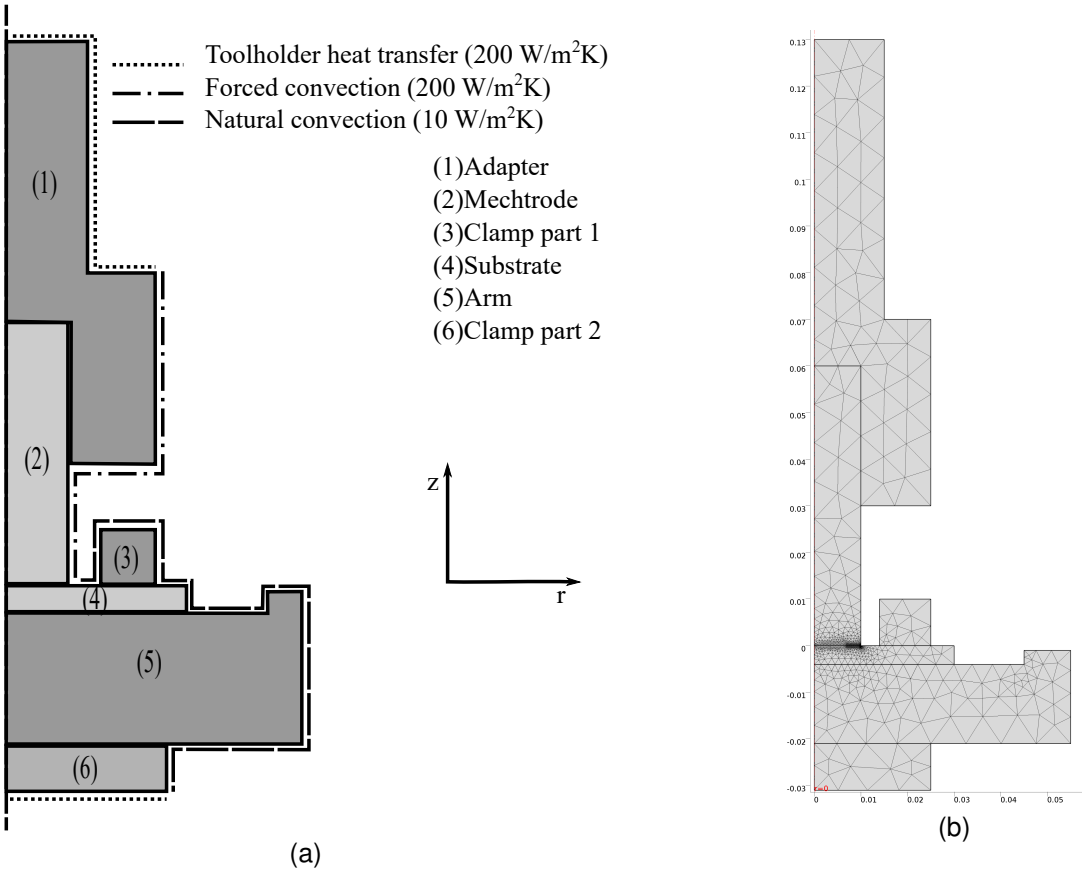

Figure 4.2: *2D axisymmetric thermo-mechanical model: (a)Schematic overview (b) Distribution of elements through the model. Note the relative small element size near the interface of the mechtrode with the substrate.*

Boundary conditions

The boundary conditions of the model are different per location as is shown in Figure 4.2 (a). First the adapter (1) and the mechtrode (2) are rotating at angular velocity ω, therefore they are exposed to forced convection instead of natural convection. The forced convection is estimated at $200W/m^2K$[34]. The influence of the different diameters of the adapter (1) and the mechtrode (2) is considered negligible, due to the distance and the high magnitude of the heat source. Adapter(1) and clamp part 2(6) are both in contact with the rest of the experimental setup. To simulate this, a heat transfer coefficient of $200W/m^2K$ is used, comparable to the value used by Dickerson et al. [35] for non-ideal thermal contact of tool holders in FSW. The rest of the boundaries of the model are considered under the influence of natural convection with a value of $10W/m^2K$, as mentioned by Lohwasser and Chen [32]. The ambient temperature is set at 293.15K.

Mesh

The overall element size is set at fine with an average size of 8.53mm. The mesh size is locally refined with 24 elements at the interface of the mechtrode and the substrate. A small fillet of 0.1mm was added at the right corner of the mechtrode to prevent sharp corners that cause infinite gradients. The result of this is shown in Figure 4.2. The convergence was checked in appendix D.

Heat flux

The heat that is generated at the contact interface of the mechtrode with the substrate has been determined as Q_{total}. However in order to implement this in the thermo-mechanical model an expression of the heat along the interface needs to be found. Two distributions are considered. A uniform distribution, or zero order and a first order distribution, illustrated in Figure 4.3.

Figure 4.3: *Schematic of the heat flux distribution with thermocouple inside (T_{ci}) at (-4, 0)mm and thermocouple outside (T_{c0}) at (-4, 8)mm: (a) zero order, (b) first order*

The heat flux conditions of thermo-mechanical model will be valid till the moment stage III starts. In chapter 3 for test 44 this point has been determined at 27.5 seconds. The reason for this is that in stage III the deposit is formed. When the deposit is formed the heat source is no longer in contact with the substrate but with the deposit instead. It is chosen to only model the stages before that, because the goal of this thesis is find the bonding behaviour of the starting phase.

When a cylindrical coordinate system is used, with r the radius and θ the rotation. The expression of heat flux q(r) along the contact interface can be calculated as follows:

$$Q_{total} = \int qdA = \int_{\theta}\int_{R} qrdrd\theta \tag{4.2}$$

$$q = q_0 \quad for \quad 0 \leq r \leq R: \qquad Q_{total} = \pi R^2 q_0 \quad \Rightarrow \quad q_0 = \frac{Q_{total}}{\pi R^2} = \frac{M\omega}{\pi R^2} \tag{4.3}$$

$$q = q_1 r \quad for \quad 0 \leq r \leq R: \qquad Q_{total} = \frac{2\pi R^3 q_1}{3} \quad \Rightarrow \quad q_1 = \frac{3Q_{total}}{2\pi R^3} = \frac{3M\omega}{2\pi R^3} \tag{4.4}$$

The result of the different order heat flux on the temperature distribution at the location of the inside and outside thermocouple is shown in Figure 4.4.

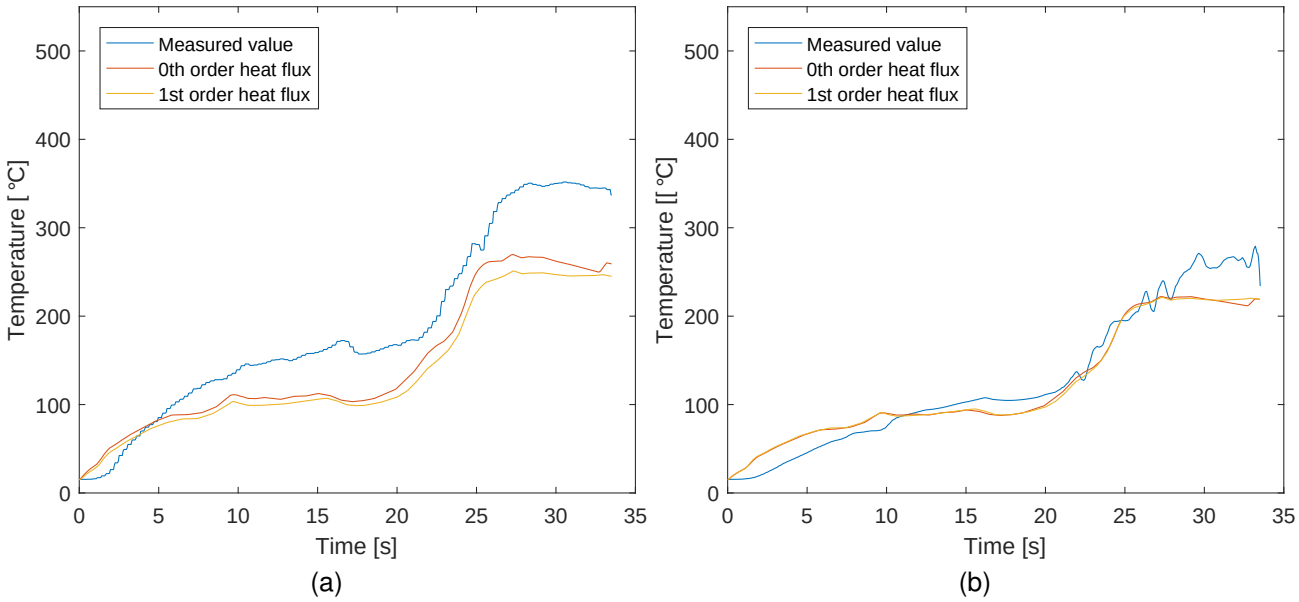

Figure 4.4: *Effect of different heat flux on the temperature distribution:(a) inside thermal couple (b) outside thermal couple*

When the first and zero order heat flux are compared to each other it is clear that the zero order causes a higher temperature than the first order for T_{ci}, while for T_{co} the first order has a marginal higher temperature result than the zero order. An explanation for higher temperature for the zero order at T_{ci}, is that the flux is higher on the inside for the zero order than the first order. For the T_{co} this is the opposite as a result that the temperature is highest for the first order. The difference of the magnitude can be explained that the T_{co} is not placed at the absolute outside and therefore not at the maximum point of the flux of the first order. Another explanation is that the aluminium of the substrate past the mechtrode radius acts as a heat sink and therefore the outside thermocouple is less sensitive for heat flux fluctuations. For further study it is chosen to only investigate the zero order heat flux further because it came closest to the real inside thermocouple values and explorative studies at higher rotation rates or axial forces showed an even more positive result for the zero order heat flux.

Effective radius

When the simulated heat flux is compared to the measured values it follows the same trend line, but is also below the measured values. A reason for this could be that the model uses a wrong effective radius. The effect of a smaller effective radius is that a larger flux will be concentrated on a smaller area resulting in higher temperatures at the thermocouple locations. When the cross section of test 44 in Figure 4.5 is investigated, the bonding width is smaller than the actual width of the mechtrode suggesting that the effective radius is also smaller than the actual radius. In Figure 4.6 zero order heat fluxes have been tried with different radii.

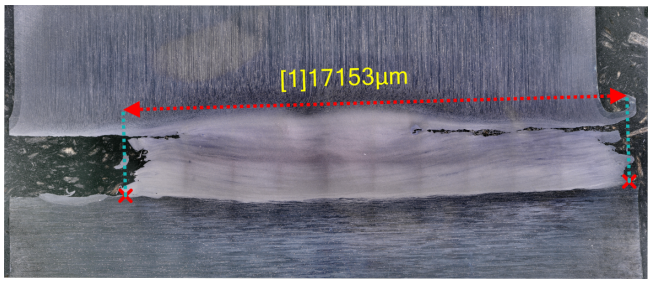

Figure 4.5: *Cross section test 44 force 5kN stopped after maximum temperature was reached. The top of the sample is the mechtrode, the middle the deposit and the lower part the substrate. The effective radius is determined as the thickest point of the deposit.*

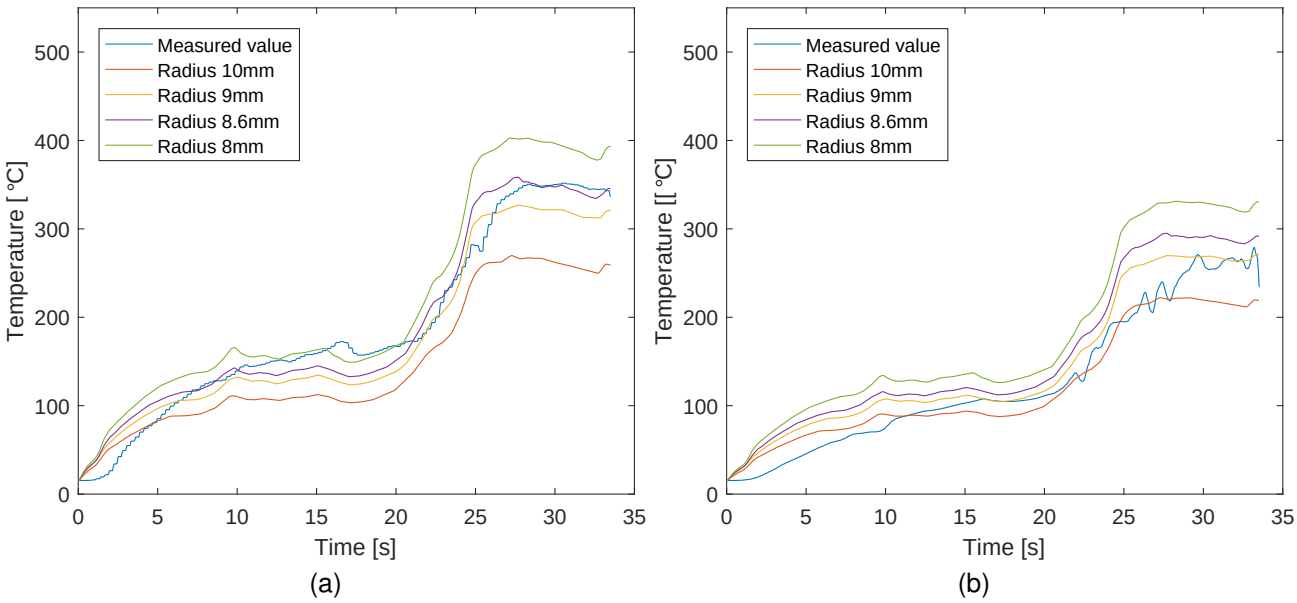

Figure 4.6: *Effect of effective radius R:(a) on the inside thermocouple, (b) on the outside thermocouple*

Figure 4.6 shows that the effect of the radius on the temperature distribution is substantial. For the T_{ci} temperature distribution the best simulated result is with an effective radius of 8.6mm, see Figure 4.6 (a). For the T_{co} temperature distribution this value is around the 9mm,see Figure 4.6. Values that correspond to the measured bonding width of the cross section of test 44 , see Figure 4.5. At the correct effective radius the model is able

to predict the temperature distribution accurately at the point of maximum temperature. For an effective radius of 8.6mm the model is able to predict the maximum inside temperature with an error of less than 0.1 %, the maximum outside temperature is predicted with an error of less than 3 %. Notable is that the accuracy is less for the start and plateau. The model does not hold the natural lag into account. The model assumes a heat flux the moment a torque is measured, while in reality the setup first elastically deforms before all the torque is converted into heat causing a natural lag. In the graphs this would result in graph displacement to the right, fitting the simulated temperature distribution of the T_{co} to the measured value. For the T_{ci} temperature distribution proportional bigger error at the plateau can not be explained by a graph displacement and is caused by the general inaccuracies of the model compared to the measured situation. Concluding the model is a reasonable first order approach to the heat transfer problem. A smaller effective radius is convincingly explained but the other effects such as starting effects and vibrations are neglected.

4.2 Mechanism of the bonding process

In previous section the thermo-mechanical model was used to predict the temperature distribution for the whole sample. In this section the thermo-mechanical model will be used to explain the mechanism of the bonding process during the starting phase, of friction surfacing.

Temperature distribution at each stage

In chapter 3 four stages were introduced to describe the bonding process. The thermo-mechanical model allows to investigate the temperature distribution of these stages. In Figure 4.7 the temperature distribution is plotted for each stage. The isoline of stage I_a(7s) and I_b(20.5s) are relatively close together, suggesting that the rise of temperature in that time interval rises relatively little. In Figure 4.8 the heat flux and temperature as function of time are plotted also the temperature distributions of the respective time of each stage has been added. In the temperature distribution of stage I_a and I_b it can be seen that temperature gradients for the surrounding material are higher than for the contact surface area. In section effective friction this phenomena is explained further.

The temperature rises till the maximum interface temperature is reached, for test 44 this is a temperature of approximately 425 °C, see at 0mm from the centre in Figure 4.8. The maximum interface temperature is reached at exactly the same moment stage II begins. Explaining that the material starts to fail at this point. Where the material will start to fail will be researched further in this chapter. From the stage II temperature distribution it can be seen that the mechtrode has a overall higher temperature than the substrate, because the substrate has more direction to conduct the heat to. This behaviour continues in stage III. There it was observed that most of the plastic deformation is initiated at the mechtrode. The shearing plane of the plastic deformation happens at the point were the material is weakest, in the situation of stage II and III were the material reaches the highest temperature. Once the plastic deformation starts the substrate is able to conduct more heat from the shearing plane than the mechtrode, thus the location of the weakest material moves in the direction of the mechtrode resulting in a rising deposit. The drop of the heat flux shows a change in the heat generation conditions and will be research further in this chapter.

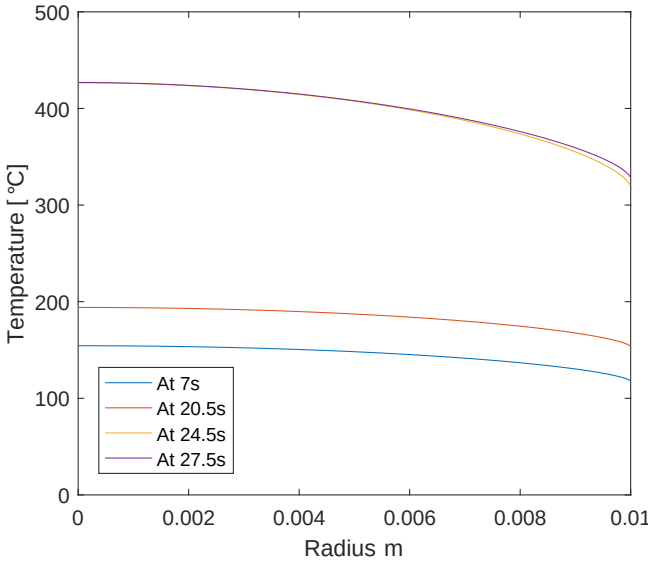

Figure 4.7: *The contact surface temperature for the whole contact surface at the stage time steps.*

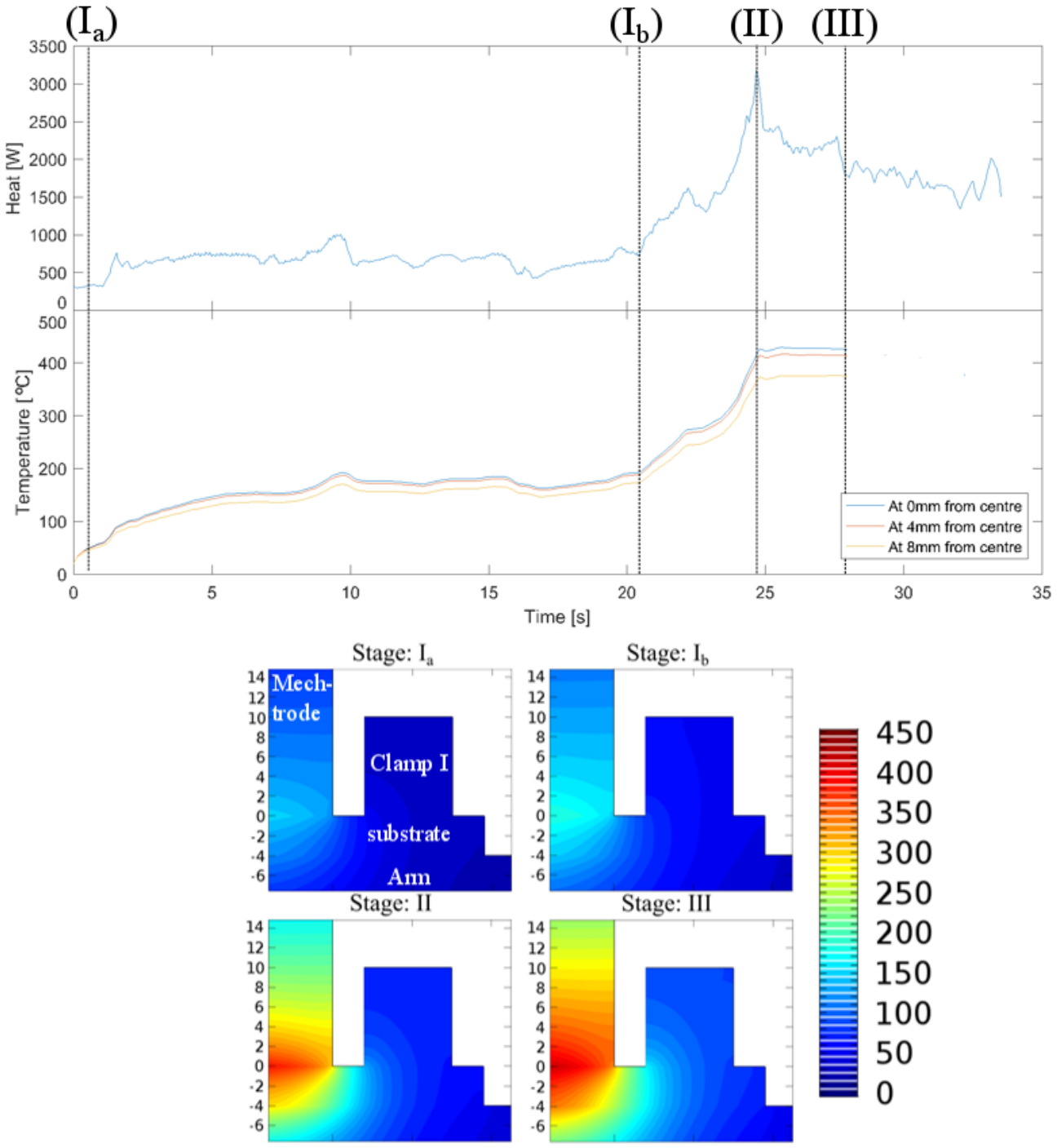

Figure 4.8: *Heat flux and surface temperature plotted over time at three location measured with stages marked and investigated in contour plots: Stage I_a simulated at 7 seconds, stage I_b at 20.5 seconds and II and III at 24.5 and 27.5 seconds respectively.*

Failure mode

From the video observation and the temperature distribution it was concluded that plastic deformation was for the major part initiated at the mechtrode. The mechtrode can be viewed as shaft with a torsion applied on. The shear stress distribution that occurs through the whole shaft due to torsion is illustrated in Figure 4.9 and can be described as:

$$\tau = \frac{Mr}{J_t} = \frac{2Mr}{R^4\pi} \tag{4.5}$$

Where τ is the shear stress in the material, R the radius of the mechtrode, r the radius of the point that is investigated and M the highest measured applied torsion. Note that in the thermo-mechanical model and the

cross section an effective radius was found, therefore a range of radii will be investigated starting form the lowest effective radius till the true radius of the mechtrode.

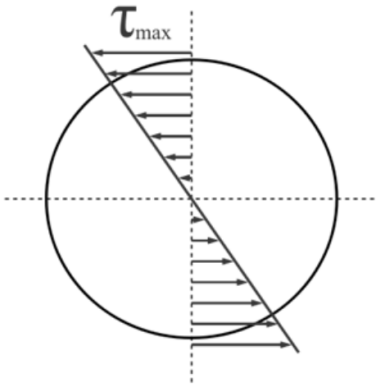

Figure 4.9: *Shear stress distribution of the mechtrode caused by the torsion*

Notable is that the distribution is only valid for the elastic range. It will therefore be used to determine the transition point from elastic to plastic deformation. In an isothermal situation the failure would start at the outer edge. However, in this case the difference of temperature between the centre and outer edge, at start of plastic deformation, is up to 100 °C, as can be seen in Figure 4.7. From Figure 2.7 in chapter 2 it can be seen that the flow stress of aluminium is highly dependant of the materials temperature. Therefore a check has to be made to verify that the initial failure starts at the outer edge. Using Von Mises in equation 4.6 and the initial axial force, the shear yield stress can be determined, as is shown in Figure 4.10(a).

$$\tau_{contact} = \tau_{flow}(T) = \sqrt{\frac{\sigma_{flow}(T)^2 - \sigma_{33}^2}{3}} = \sqrt{\frac{\sigma_{yield}(T)^2 - (\frac{F}{\pi R^2})^2}{3}} \tag{4.6}$$

An expression can be made of the maximum allowable shear stress as function of the radius of the mechtrode, using the surface temperature distribution at the time step of the plastic deformation from Figure 4.7.

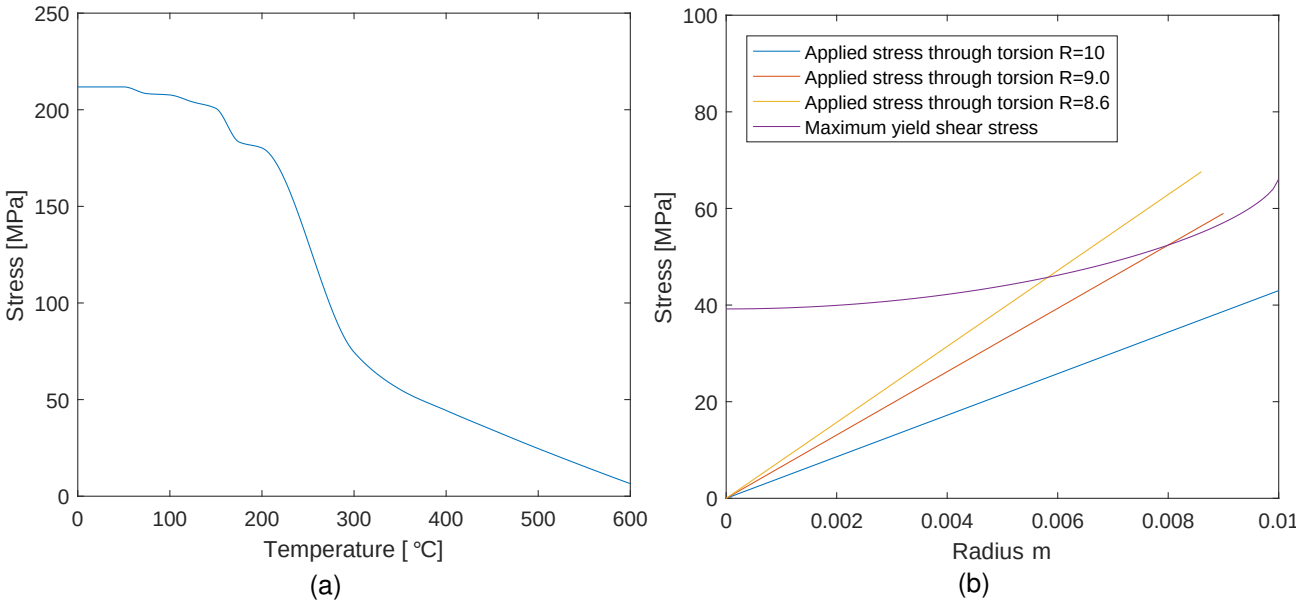

Figure 4.10: *(a)The maximum allowable shear stress of the aluminium 2024 under an axial load of 5kN (b) the maximum allowable shear stress of the mechtrode respectively to the contact surface temperature versus the applied torsion stress of an assumed shaft.*

In Figure 4.10(b) the applied stress for different effective radius and the maximum flow stress are plotted as function of the radius of the mechtrode. It can be seen that according to the Von mises criteria, the temperature distribution and the literature findings of the yield stress of aluminium 2024, the stress distributions of

an effective radius of 10mm applied stress does not pass the allowable maximum shear stress. The stress distributions of an effective radius of 9mm passes the allowable maximum yield shear stress at approximately 8mm with a minimal margin. And the stress distributions of an effective radius of 8.6mm passes the allowable maximum yield at approximately 6mm. From these findings it can be concluded the mechtrode would not plastically deform at the highest measured torque if the effective radius is equal to the mechtrode's radius. The figure shows that plastic deformation would occurs at an effective radius of 9mm, but considering the margin it shows and the inaccuracies introduced by all the assumptions it is no conclusive prove. However, the stress distribution of the effective radius of 8.6mm shows a rapid increase in the margin, suggesting that the effective radius should be somewhere in between that range. The stress distribution for the effective radius of 8.6 and 9mm shows that plastic deformation is initiated at the outer edges.

Effective friction coefficient

In order to determine the mechanism of the bonding process, the behaviour at the contact area needs to be known. At the contact area frictional and sticking forces cause the heat to be generated. To see what is happening at the interface the friction coefficient is investigated. However, because it is unknown when the frictional and when sticking forces occur exactly, only the effective friction coefficient can be determined. From the torque measurements the effective friction can be determined as follows:

$$M = \int_A r\tau_{contact} dA = \int_{2\pi}\int_R r^2 \tau_{contact} dr d\theta \tag{4.7}$$

$$\Rightarrow \frac{2}{3}\pi R_{eff}^3 \tau_{contact} = \frac{2}{3}\pi R_{eff}^3 \sigma_{33}\mu_{eff} \tag{4.8}$$

$$\Rightarrow \mu_{eff} = \frac{3M}{2\pi\sigma_{33}R_{eff}^3} = \frac{3M}{2FR_{eff}} \tag{4.9}$$

In Figure 4.11(a) the effective friction coefficient and the average surface temperature according to the thermo-mechanical model as function of time have been plotted. The graph shows that at approximately 20 and 25s the behaviour of the friction coefficient changes, the average surface temperature also changes. At approximately 33s the effective friction coefficient changes but no impact is seen on the average surface temperature. This peak is caused by stopping the experiment and has same explanation as for the torque in chapter 3. From the graph the two critical temperatures T_{c1} and T_{c2}, see chapter 3, can be determined. The first is the average surface temperature T_{c1} when the friction coefficient suddenly rises. This temperature is approximately 160 °C when stage I_a transitions into stage I_b. The second critical temperature is at approximately 380 °C. When stage I_b changes into stage II. A sudden drop of the effective friction coefficient can be observed at 24.5s.

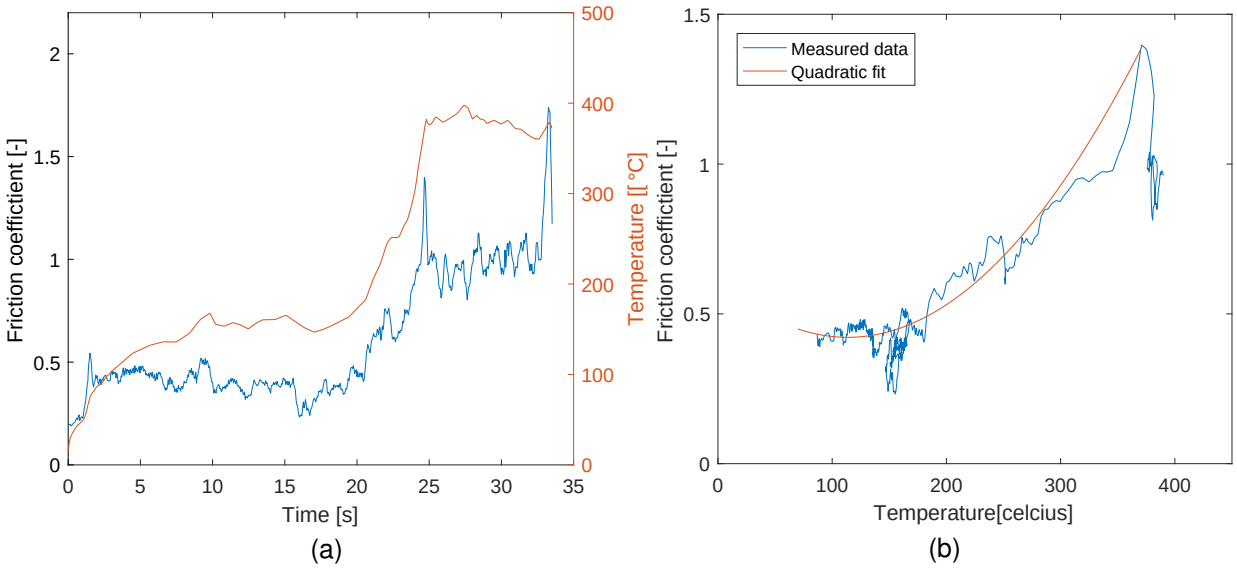

Figure 4.11: *Effective friction coefficient μ:(a) versus time, (b) versus average surface temperature*

In Figure 4.11(b) the effective friction coefficient is plotted versus the average temperature. The effective friction coefficient is taken between 1.5 and 27.5s to exclude start and ending effects. The effective friction coefficient shows a disturbance at approximately 160 °C, mainly caused by the long duration of stage I_a and the temperature plateau, producing a lot of data for the same temperature range. In general the effective friction

coefficient follows a quadratic path, see quadratic fit, suggesting that not the sticking phenomena is causing the sudden rise of temperature. At 380 °C the friction coefficient shows a relatively big drop, suggesting a change of the interface condition. The change of the interface condition will be investigated in the next section.

Analytical heat flux

In chapter 2 an analytical expression for the heat flux was derived, see equation 4.10. This equation allows the prediction of the heat flux if the initial condition, R, ω, F, σ_{yield}, μ and the slip/stick-conditions are known.

$$Q_{stick/slip} = \delta Q_{stick} + (1-\delta)Q_{slip} = \frac{2\pi}{3}\omega R(\delta\sqrt{\frac{\sigma_{yield}(T)^2 - (\frac{F}{\pi R^2})^2}{3}} + (1-\delta)\frac{F}{\pi R^2}\mu) \tag{4.10}$$

The equation will be implemented in the thermo-mechanical model to see if the equation is able to predict the heat flux of FS properly. However the thermo-mechanical model is relatively simple and is only focused on the heat transfer physics. Therefore it is not able to calculate the force equilibrium caused by the thermal expansion. Tests with changing axial force will be difficult to implement in this model. To circumvent a complicated implementation of analytical expression that simulate the rise in axial force that is also likely to cause high inaccuracies in the model, it is chosen to use Test 43 to compare analytical expression to the measured heat flux. Test 43 has an almost constant force until the plastic deformation occurs. Tests that have no constant axial force before plastic deformation is initiated, are left for further research. The measured and simulated results of Test 43 can be seen in Figure 4.12.

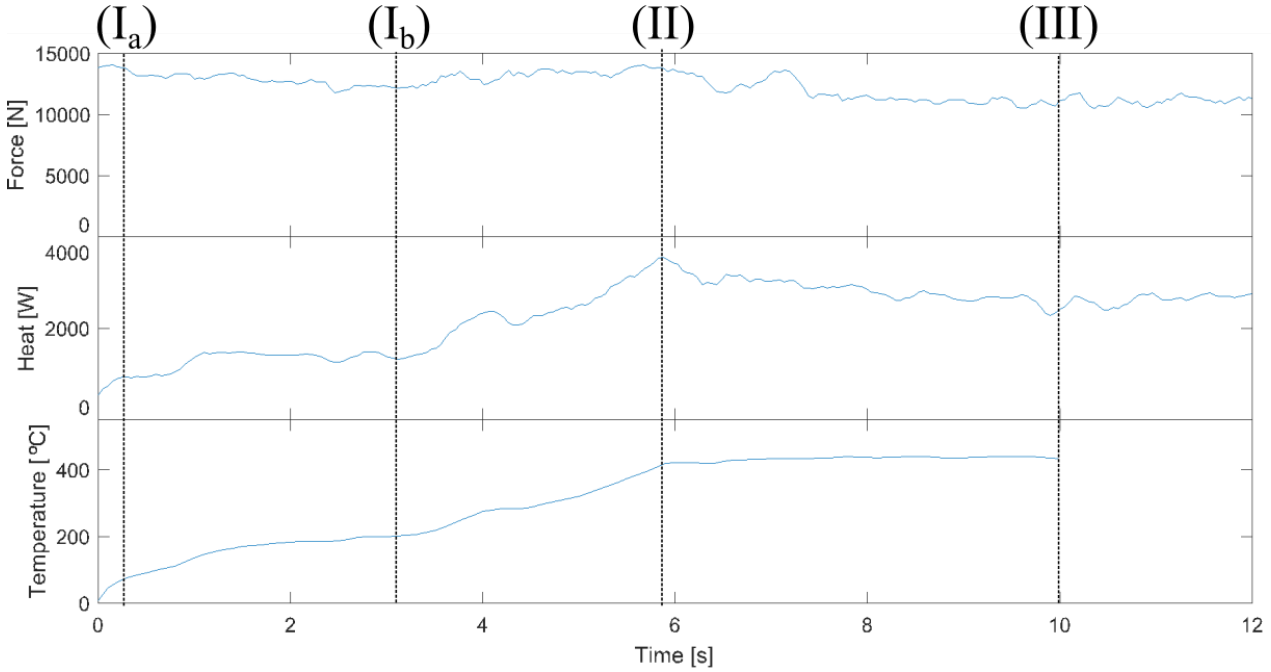

Figure 4.12: *The measured force, calculated heat and the simulated average surface temperature of test 43 divided in the four stages: I_a at 0.4s, I_b at 3.1s, II at 5.95s and III at 10s.*

Each stage of the FS process can be assigned a slip/stick condition accordingly. The first two stages of the process show no sign of plastic deformation, also the frictional stresses are lower than the allowable yield stress of the material at that temperature, therefore a sliding condition is assumed. For Stage II a slip/sticking condition is assumed because local deformation was observed. And finally at stage III a deposit, through macro plastic deformation, is formed between the mechtrode and substrate, thus a sticking condition is assumed. The stick/slip conditions and their respective average temperature are summarized in table 4.1.

Table 4.1: *Interface condition at each stage*

	Interface condition	δ	Average T(°C) Range
Stage $I_{a/b}$	Sliding	0	0-420
Stage II	Sliding/sticking	0 $<\delta<$ 1	420-430
Stage III	Sticking	1	$\leq$ 431

Literature does not provide a friction coefficient that describes the friction coefficient under these conditions for different temperatures, therefore the experimental values of test 43 will be used to describe the friction coefficient temperature relation. With the assumption that full sliding happens till 420 °C the friction coefficient is equal to the effective friction coefficient. A second order fit is applied at the result to improve continuity.

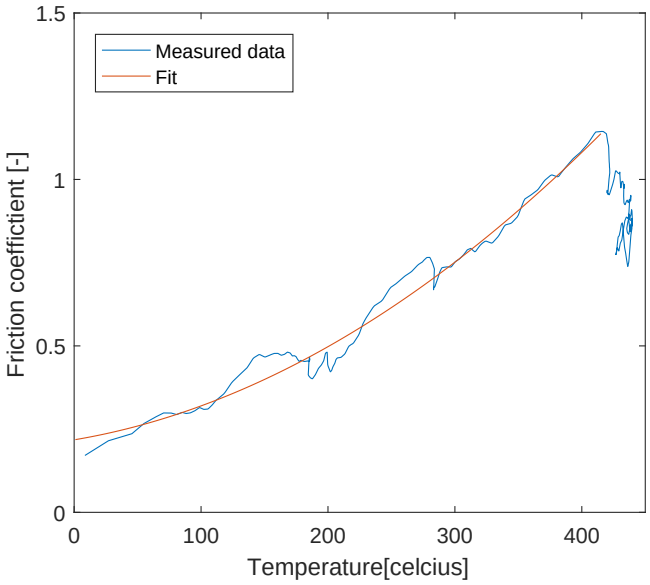

Figure 4.13: *The friction coefficient of test 43 plotted versus the simulated average surface temperature and the second order fit that is used in the analytical heat flux*

At stage II it is assumed that a sliding/sticking condition is applied. However, it is still unknown what the slip/stick ratio δ is. For that three situations are tested. The first is an instant change of slip to stick with δ=1, the second is partial slip-sticking condition with δ=0.5. And finally the partial slip-sticking condition with an exponential decline of δ. The results are shown in Figure 4.14.

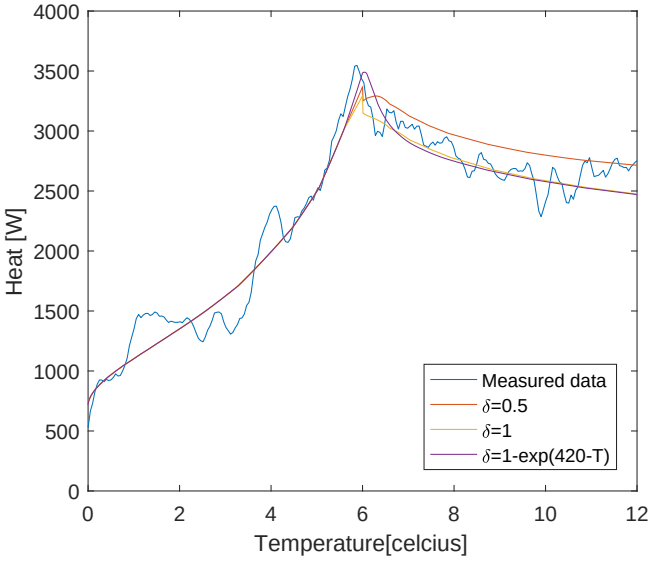

Figure 4.14: *The friction coefficient of test 43 plotted versus the simulated average surface temperature and the second order fit that is used in the analytical expression*

When the different analytical heat fluxes are tried in the thermo-mechanical model, stage I_a and I_b of the analytical heat fluxes follows accurately the measured value. This is not surprising as the measured values were used as input. However, stage II and III show also a very accurate result in comparison to the measured values. Suggesting that the general assumptions of the stages, sliding, partial sliding/slicking and sticking, are accurate for the real situation. When the slip/stick ratio of stage II are investigated, it can be noted the most accurate is the δ with the exponential decline. The δ with the exponential decline allows a small rise of the heat

flux peak when stage II has been entered, approximating the measured peak with an error of approximately 1%, while for the δ=0.5 this rise is smaller and for the δ=1 non-existent. The δ with the exponential decline also shows a natural transition between the stages, while the others show an instant drop. Concluding that stage II is characterized by a exponential temperature dependant slip/stick-condition rather than a fixed value.

The bonding process

The bonding process can now be fully described based on the observation of the measurements and created models. In Figure 4.15 a scheme is illustrated of the bonding process. The process starts by entering stage I_a. The mechtrode is pushed on the substrate with axial force F and rotation speed ω. The movement creates a dynamic friction that generates heat. The dynamic friction is dependant of the surface made with the contact asperities i.e. the effective surface. The heat generated by the frictional stresses, lowers the shear stress of the materials and causes local deformation that destroys the peaks increasing the effective surface. The rotational causes on a micro scale in the first milliseconds more heat on the outside than on the inside. Outside edges therefore deform more easily resulting in a effective radius contact for the contact surface. An increase of the effective surface results in an increase in the friction coefficient, explaining the rise of the friction coefficient in stage I_a and I_b. For lower axial forces the heat flux is to low the temperature gradients are to high and the increase of the contact surface temperature goes relatively slow. The temperature of the surrounding material needs to be saturated, to lower the temperature gradients at the contact area. When an average surface temperature of 160 °C is reached, most of the surrounding material is saturated to lower the temperature gradients enough for the process to enter stage stage I_b. In stage I_b the average contact surface temperature rapidly increases, resulting in higher friction coefficient. The higher friction coefficient in turn causes a higher heat flux. This process continues until the material maximum allowable stress is lower than the applied the stress through friction at an average surface temperature of T_{C2}. The process enters stage II the mechtrode starts to deform at the outer edge of the effective radius. The heat is now partially generated by frictional forces and partially by plastic deformation. The part of the plastic deformation grows till the plastic deformation happens at the entire contact surface, thus entering stage III. In stage III a deposition is formed between the mechtrode and the substrate, because the substrate is more able to conduct heat away from the contact area. And finally flash is formed at the etches of the mechtrode due to the lack of lateral confinement.

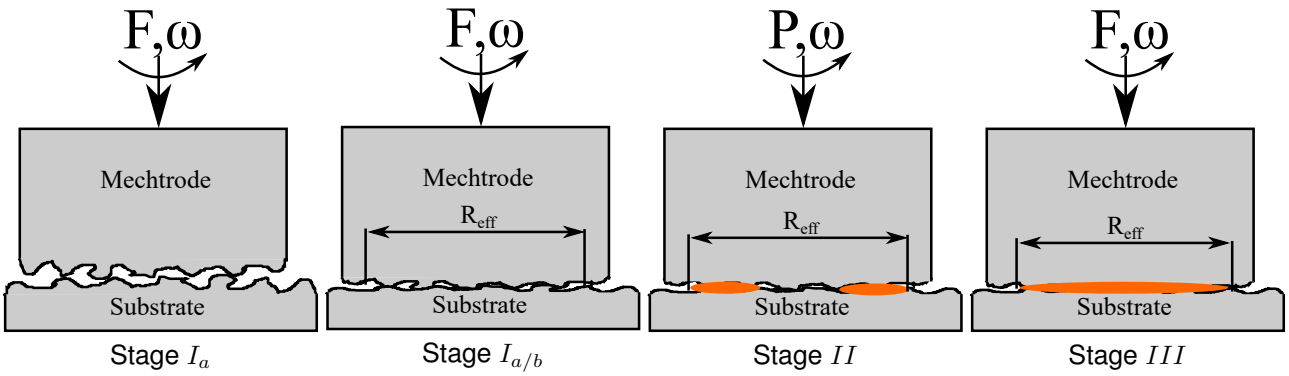

Figure 4.15: *Schematic of the bonding process not the change in asperities and later on the location of the plastic deformation.*

4.3 conclusions

It is possible to create an accurate model that shows representative temperature flow in the substrate with torque measurements as heat source input. However, other effects such as starting effects and vibrations are neglected. A uniform heat distribution is the most likely form of the two heat distribution tested according to the readings in the temperature flow. It is reasonable to assume an effective radius based on the cross section and the values of the temperature flow of the model. For this setup in combination with a uniform heat distribution the effective radius between 8.6mm and 9mm generated the most accurate result in comparison to the measurements of the thermocouples for test44.

For the bonding process the simulated temperature distribution showed that the heat conducting to surrounding material is a cause for the plateau forming in stage I_b and that the rise of the deposit in stage III is caused by the difference of heat conduction between the substrate and mechtrode. The failure mode showed that plastic deformation is initiated at the outer edges of the mechtrode effective radius. The friction coefficient showed

that sticking only occurs at stage II. Therefore the rise of the temperature in stage I_b is solely caused by a lack of heat flux versus the conducting material. Finally it is possible to create an analytical expression that is able to predict the heat flux accurately, using the initial conditions, with a test for a constant force and accurate input for the friction coefficient. The analytical expression versus the measured showed that stage II is best fitted with slip/stick condition that has a exponential decline. Assuring a smooth transition from the sliding to the sticking condition.

Chapter 5

Post experiment testing

One of the goals of this study is to find the optimal parameters that give the best quality in the bonding. The quality of the bonding has been tested with tensile and hardness tests. This chapter will start with the microscope and hardness test and end with the tensile tests. Each test will start with an explanation of the test setup, the results and later on the interpretation of these results.

5.1 Microscope study and hardness tests

FS is a mechanical heat generated deposition process it influences the original substrate and mechtrode material structure. The microscope study and hardness test will investigate the microstructure of the bonding through the hardness and visual image of the microscope pictures. In this section two of the parameters sets will be researched: the axial force, see Table 5.1 and the maximum temperature at the thermocouples, see Table 5.2. This section will start with the sample preparation. Subsequently the influence of the FS process on microstructure will be explained based on the microscope image and hardness results of Test 60, a test that is present in Table 5.1 and 5.2. Later the influence of the axial force in the FS process on the bonding quality will be investigated. Finally the influence of the substrate temperature on the bonding quality will be investigated.

Table 5.1: *Axial force data set M&H*

Experiment	ω(RPM)	F(N)	T(C°)
Test 60	450	5.000	330
Test 59	450	7.500	330
Test 57	450	10.000	340
Test 58	450	12.500	330

Table 5.2: *Temperature date set M&H*

Experiment	ω(RPM)	F(N)	T(C°)
Test 49	450	5.000	230
Test 40	450	5.000	240
Test 41	450	5.000	280
Test 38	450	5.000	300
Test 60	450	5.000	330
Test 44	450	5.000	350

Sample preparation

For the microscope study and hardness test the samples needed to be prepared. First the samples were cut in half, with a diamond saw with coolant, in a size of approximately 20x8mm to fit embedding. Subsequently, the samples were embedded in Phenolic hot mounting resin in a Struers LaboPress-3 machine at a force of 40kN with a heating time of 6 min and a dwelling time of 6 min. Unfortunately, the embedding was performed at 180 °C. In literature it was found that the gp-zones of ALCu-precipitates start to disappear at approximately 100 °C [19]. In other literature no difference in hardness could be found for samples of 2024-T4 till 177 °[14]. Thus literature states that the thermal embedding is likely to cause an effect on the microstructure but was not conclusive about the exact effect of it. Hence, the extra thermal treatment should be taken into account while analysing the results of the samples.

After embedding the samples were mechanically ground using grit silicon papers up to grade 4000. Polishing was performed in three steps with a final polishing step using a colloidal silica suspension with a particle size of approximately 0.04 μm. And finally the samples were etched by 50% NaOH etchant at approximately 70 °C for 10s for microstructure observation. The bonded interface and the grain structures near the interface were examined with an Keyence optical microscope VH-Z100UR with an magnification up to 1000X. Vickers hardness measurements were performed with a LECO LM100 automatic micro-hardness measuring device employing a 0.981N load for 15s.

Influence of FS on the microstructure of the samples

In FS the hot working of the mechtrode tip generates heat which is conducted along the mechtrode and substrate, pre-heating the material and enabling its plastic deformation. This enables three zones in the workpiece: a thermo-mechanical effected zone(TMAZ), in this zone the material is influenced by the mechanically induced shear and heat, a heat effected zone(HAZ), in this zone only the heat is effecting the material structure and

finally the base material (BM), in this zone the penetration of the heat is too low to cause change in the material structure. The effect of incomplete metallurgical bonding is thought to be associated with local variation in the axial force throughout the coating layer during the process.

The heat induced by the FS process creates a time dependent temperature distribution that is different along the mechtrode's axial direction. Therefore the influence on material depends on the distance to the contact area. Hardness test have been taken along the mechtrode's axial direction to investigate the influence. Figure 5.1 shows a cross section of the mechtrode and the substrate, depicting the result of the transformation in the material structure caused by the FS process. The top part of the cross section is the mechtrode, the high contrast shows the TMAZ and the lower part is the substrate. High magnification images of interesting sites at the TMAZ have been added in Figure 5.2. The simulated temperature distribution of test 60, at the highest temperature, can be seen in Figure 5.3.

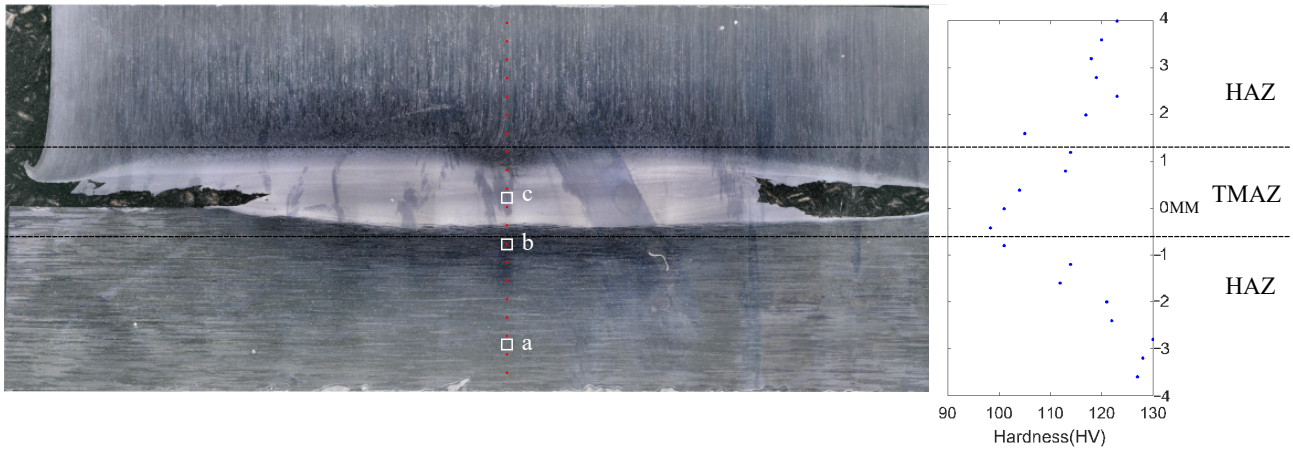

Figure 5.1: *Cross section of Test 60 (parameters:450RPM, 5kN and 330° C). The cross section can be divided into two section. The HAZ and a TMAZ. Note Test 60 has the same parameters as Test 44, only was stopped just before flash formed*

At the top of the mechtrode it is observed that boundaries of the grains are preferential aligned along the axial direction of the mechtrode. When distance decreases to the contact area the size of the grains decreases and the preferential direction changes to shear direction of the FS process. The bottom of the substrate shows anisotropic grains aligned with the roll direction of the fabrication of the plate material, similar to the received material, see magnification in Figure 5.2(a). The bottom part of the magnification in Figure 5.2(b), is characterized by a structure of coarse grains aligned in the roll direction. The top part of the image shows grain refinement which shows the transition to the TMAZ. Figure 5.2 (c) show a magnification in middle of the TMAZ. In the TMAZ the interaction of the thermo-mechanical process experienced in the TMAZ leads to a dynamic recrystallization of the processed material,leading to nucleation and the growth of a new set of finer grains, as can be seen in Figure.

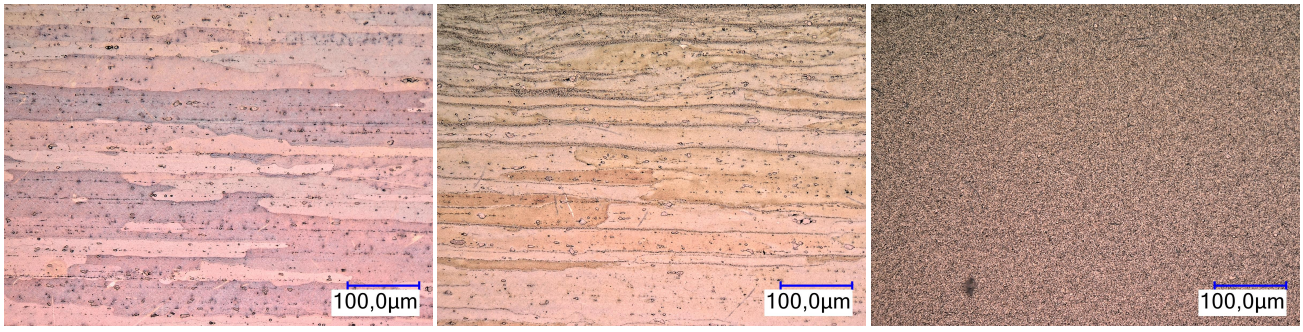

(a) (b) (c)

Figure 5.2: *Zoomed in cross sections of the HAZ (a), HAZ (b) and the TMAZ (c) of Test60*

The hardness of the FS with aluminium 2024 shows a similar trend in the distribution as found by J. Gandra et al. [28] for FS with mild steel. But shows that only the HAZ and the TMAZ zone are present. In the simulated temperature distribution it can be seen that at the peak temperature of test 60, no temperature is below 177

°C at the central axis. Therefore, according to study of Y.S. Sato et al. [25], no BM zone could be present on the central axis.

The HAZ of the substrate shows higher hardness values the father it is from the contact surface in comparison to the HAZ of the mechtrode. This is caused by the temperature distribution that has a higher penetration in the mechtrode than the substrate, see Figure 5.3. The hardness values of the HAZ are comparable to the values found by Y.S. Sato et al. [25] in Figure 2.6(b) at approximately 200 °C. The return of hardness to 140HV for temperatures between approximately 250 and 320 °C has not been observed in the hardness distribution of Test 60.

The TMAZ shows hardness values between the 100 and 115 HV. In the study of Y.S. Sato et al. [25] this hardness shows the zone has been heated 373 and 423 °C a value that agrees with the simulated temperature Figure 5.3.

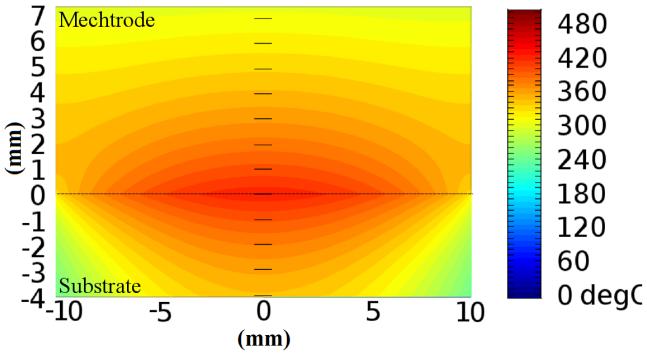

Figure 5.3: *The simulated temperature contour plot of test 60 at the highest temperature. Note: no temperature is below 177° C at the central axis.*

Influence of the axial force on the bonding quality

The experiments of Chapter 3 and the results of chapter 4 showed that higher axial forces resulted in a higher heat flux and temperatures. In this subsection the influence of the axial force on the bonding quality shall be investigated. The experiments that are investigated are performed with an axial fore of 5, 7.5, 10 and 12.5kN, see Table 5.1.

Due to loss of data the temperature distribution could not be simulated for each test of the axial force set. Therefore it was chosen to simulate the lowest axial force in the experimental set and the axial force closest to the highest axial force in the experimental set, the result can be seen in Figure 5.4. In the figure it can be observed that the 14kN axial force creates higher temperatures around the contact. The high temperatures are also more concentrated around the central axis of the mechtrode, leaving lower temperatures at the edges of the mechtrode than the 5kN axial force temperature distribution. In Figure 5.5 the cross sections and hardness results of different axial forces are shown. The hardness was tested in the middle of the TMAZ and 2mm upwards and downwards. The averages of the hardness results are given in Figure 5.6.

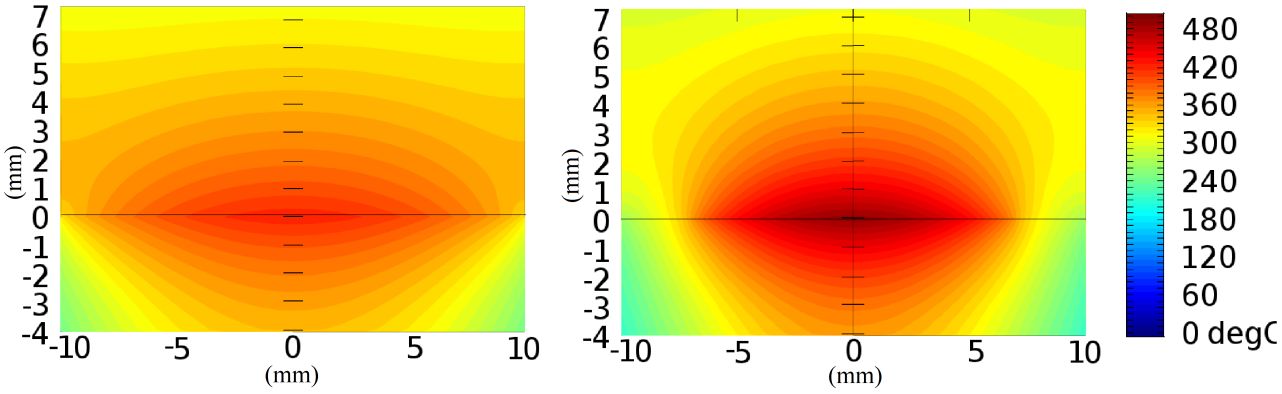

Figure 5.4: *The simulated temperature of test 60 at axial force of 5kN (left) and the simulated temperature of test 43 at axial force of 14kN (right). Note: the difference in heat flux and effective radius.*

The cross sections in Figure 5.5 show no substantial difference in the thickness of the TMAZ zone. In Chapter 3 a higher axial force resulted in more flash and plastically deformed material. An explanation for this is that these experiments were stopped just before the overall plastic deformation. Resulting in the same thickness in the cross sections.

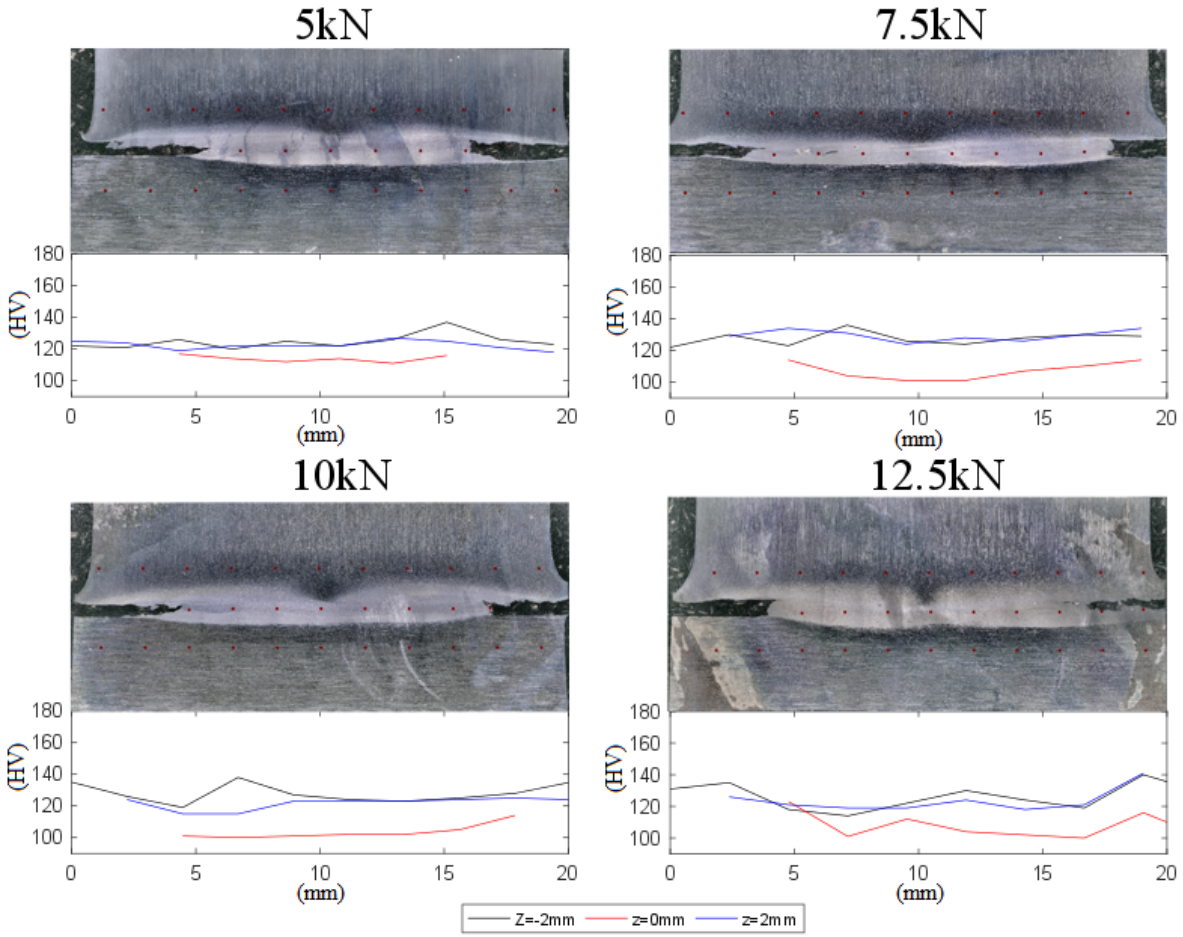

Figure 5.5: *Hardness test results of the experiments operating at and axial force of: 5kN(a),7.5kN(b),10kN(c) and 12.5kN(d).*

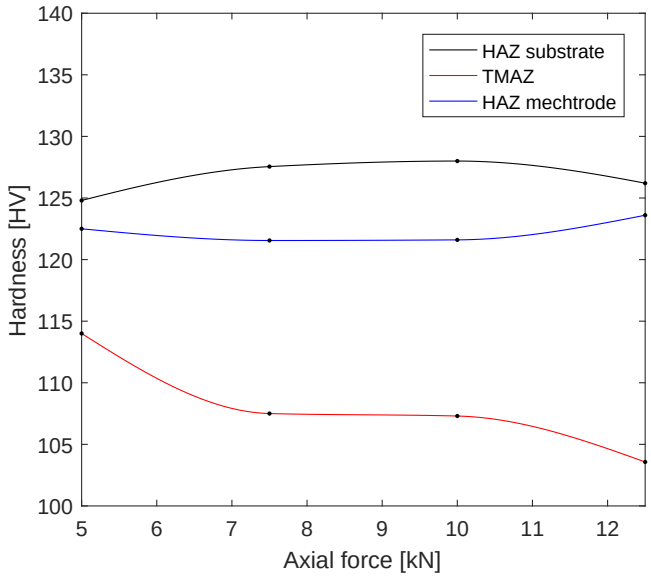

Figure 5.6: *Average values of the axial force set. The average hardness of the HAZ shows minor influence by the axial force. The average hardness of the TMAZ reduces for increasing axial forces.*

The hardness distribution shows the average hardness of the HAZ is between 120 and 130HV, see Figure 5.6.The simulated temperature distribution of Figure shows that at 2mm from the contact interface, the tem-

perature range is approximately between 320 and 370 °C for axial force between 5kN and 14kN. A range that according to Figure 2.6 shows no change of hardness. The absolute hardness of the HAZ is still approximately 20HV lower than Figure 2.6. An explanation could be that this is caused by the reheating in the embedding. Only the 12.5kN axial force experiment shows higher hardness at the edges, that can be explained by the lower temperatures at the edges for higher axial forces as can be seen in the contour plot of 14kN in Figure 5.4

The TMAZ zone shows a decrease for the hardness at increasing axial forces, see Figure 5.6. The temperature distribution of the 14kN case shows that in the core of TMAZ reaches temperatures above the 423 °C. The study of Y.S. Sato et al. [25] suggest that at that temperature some of the initial hardness of the material should return through the solving and natural ageing of the precipitates. However, no return to the initial hardness of 140HV has been observed in these test. An explanation for this could be that the simulated temperature distribution of 14kN case is an overestimation for the 12.5kN case and therefore the temperature for solving the precipitates has not been reached yet.

Influence of the surface temperature on the bonding quality

The experiments showed a higher surface temperature creates more chance for the mechtrode material to bond to the substrate. Another effect is that higher surface temperatures also create a higher risk in precipitate growth and therefore a decrease of hardness. In this subsection the influence of the surface temperature on the bonding is investigated. The different experiments are divided in their respective thermocouple temperatures 230, 240, 280, 300, 330 and 350 °C, see Table 5.2.

Figure 5.7 and 5.8 shows the cross sections, the temperature distribution and the hardness results of each test of Table 5.2. In Figure 5.9 the average hardness results of the temperature set are shown. The cross sections show that till 280 °C the mechtrode was not embedded in the sample, this was caused by the bond that was to weak to hold the mechtrode and the substrate together. The figure show that an increase of the substrate temperature results in an increase of the TMAZ. The cross section of 350 °C shows an asymmetry of the TMAZ versus the substrate and the mechtrode. When the FS process enters stage III global plastic deformation is occurring around the contact area. The plastic deformation results in a inhomogeneous shear behaviour causing the mechtrode to vibrate. Stopping the process in stage III could therefore bond the mechtrode asymmetrically to the deposit.

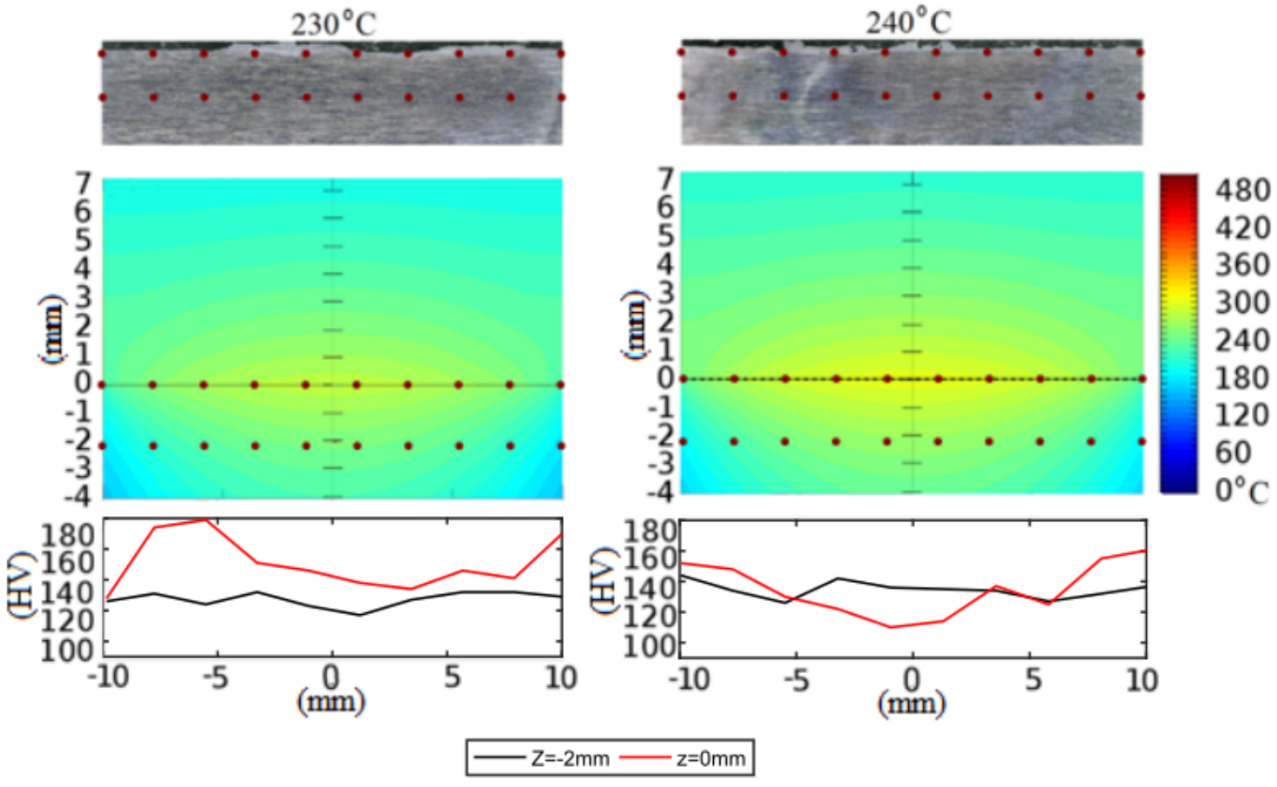

Figure 5.7: *The results of the hardness tests and simulated temperature distributions for the samples with measured a temperature of 230 °C and 240 °C. A cross section has been added at the top for clarification. The red dots show the locations of the hardness measurements.*

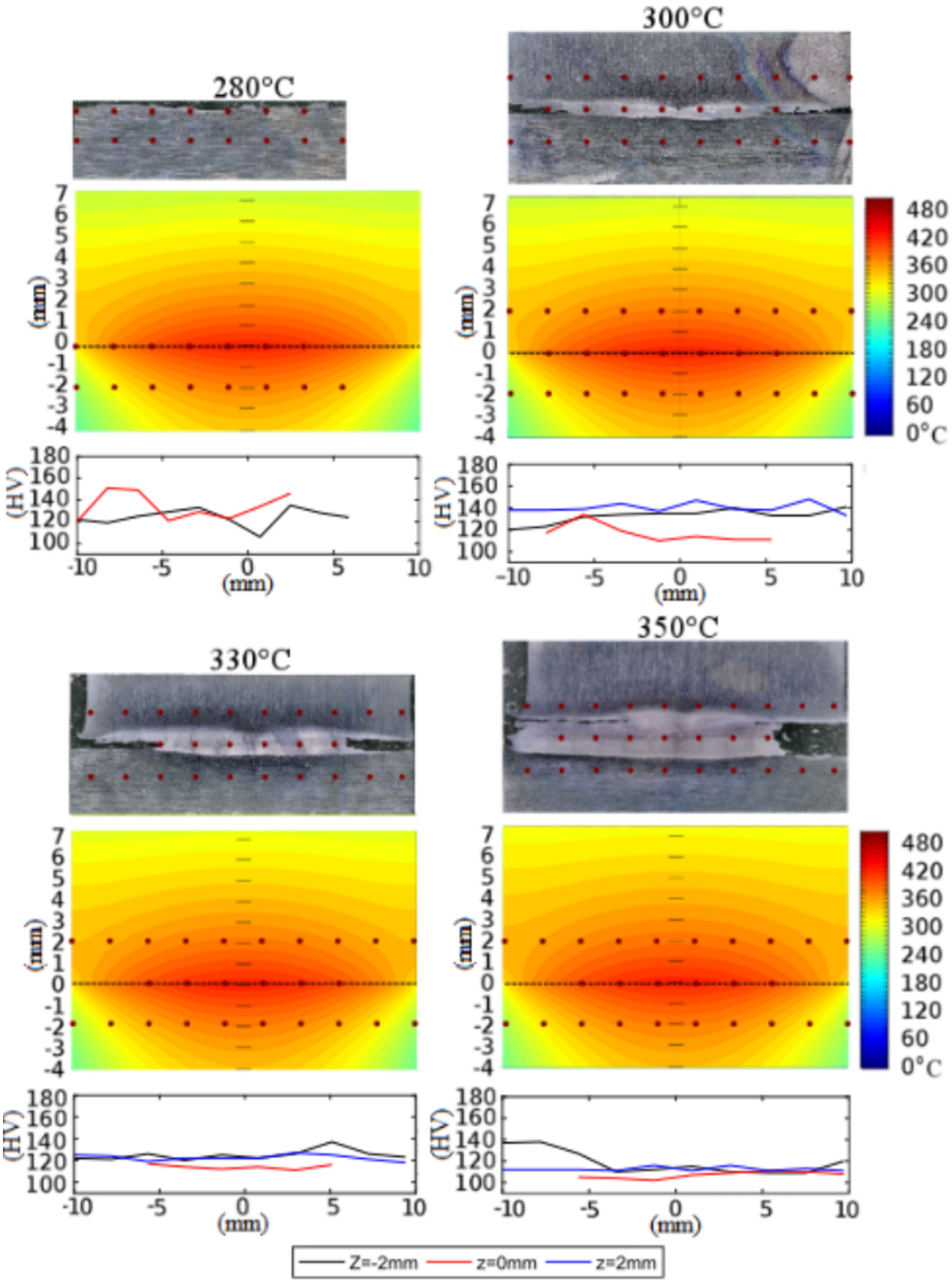

Figure 5.8: *The results of the hardness tests and simulated temperature distributions for the samples with measured a temperature of 280 °C,300 °C, 330 °C and 350 °C. A cross section has been added at the top for clarification. The red dots show the locations of the hardness measurements.*

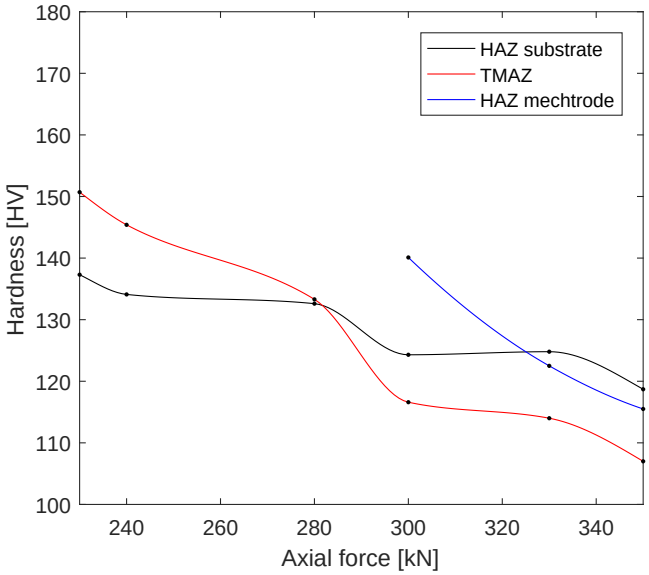

Figure 5.9: *Average values of the axial force set. The average hardness of the HAZ shows minor influence by the axial force. The average hardness of the TMAZ reduces for increasing axial forces.*

The hardness results of 230, 240 and 280°C experiments show that the TMAZ (the red line) has a higher hardness than the BM of 140HV at certain locations, see Figure 5.8 and 5.9. The embedding material has a hardness of approximately 70HV and could therefore not be causing the increase of hardness. An explanation could be that no hardness is lost due to precipitate growth, because the surface temperature is to low and short for precipitates to grow. The extra hardness is gained through the grain refinement process of the TMAZ. The higher substrate temperatures of 300, 330 and 350 °C show that the TMAZ has lower values than the BM and decreases with increasing temperature to approximately a value of 107HV. This behaviour can be explained with the growth of the precipitates. The increasing temperature at the contact area, see respective temperature distribution at z = 0mm, and the increasing time of the experiment cause precipitate growth. Larger precipitates reduce the hardness of the material.

The HAZ (the blue and black line) shows a gradual decline for all the experiments in the set with rising temperature until a hardness of approximately 115 HV has been reached. At that point higher surface temperature show no more influence on the hardness distribution in the HAZ. The decline is caused by the heat penetration of the process. The higher surface temperature experiments had a relatively longer experimental time and higher heat generation therefore heat penetration was higher in these samples. A higher heat penetration also causes a larger HAZ, but that has not been investigated. The increase of the TMAZ would move the HAZ therefore all the hardness tests have been taken at the start of the HAZ of 350 °C at 2mm from the middle of the TMAZ.

5.2 Tensile tests

Each parameter investigated created a different quality of bonding. One of the properties that determine the quality of the bonding is the tensile force. Uniaxial tensile tests have been performed to investigate the quality of the bonding. The data sets tested with the tensile test were the rotation speed, axial force and surface temperature according to Table 3.1, 3.2 and 3.3 in Chapter 3.

Special equipment has been manufactured for the samples to be tested uniaxially. The equipment allowed clamping of the sample without hitting the collar, see Figure 5.10. Before the start of the tensile test the mechtrode would be bolted to the top adapter. The substrate would still be hanging freely. The substrate would be slowly moved towards the bottom adapter. The tensile test would begin once a pretension of 25N was measured. The adapters are steel blocks with a length of 50mm and a width of 40mm. The top part has a hole of 13mm. A bolt with with washer was used to connect the sample to top adapter. The bottom adapter has a hole of the 28mm to prevent hitting the biggest flash of the samples. Teeth were added on both steel parts to enlarge grip and prevent slip between the adapters and machine clamp.

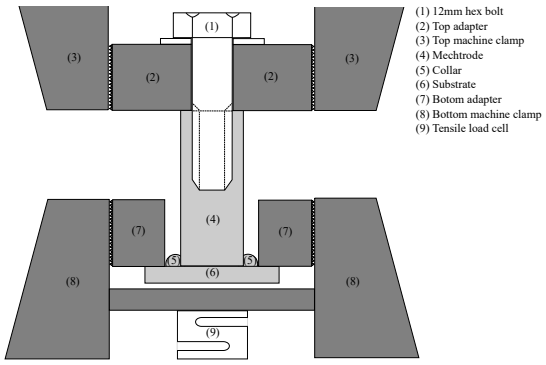

Figure 5.10: *Side view: tensile test setup*

The tensile test have been performed on a Zwick Z100 tensile test machine. The test were performed at 22 C°with a displacement of 4mm/min, the stop for break was set at 80%(when the tensile force is 80% lower the machine assumes it is broken and stops the progress).

Failure mode

Three different types of failure have been observed. The first failure type was between the mechtrode and the deposit (Figure 5.11(a)), the second in the deposit (Figure 5.11(b)) and the third in the deposit and substrate (Figure 5.11(c)). The first failure mode will be filtered out for the investigation of the parameters, because it will under estimate the results of the parameters. Furthermore, tensile tests with an extreme low value have also been filtered out, because the failure was suspected to be initiated from pre-existing cracks.

(a) (b) (c)

Figure 5.11: *Microscope stitched images of the three failure modes of the bonding. On the images the deposit and substrate are shown. Note: that the image of figure c is overexposed the edges of the image should be similar to the other images. The middle of figure c is a hole.*

Influence of the parameters on the ultimate tensile force

In Figure 5.12 the results for the tensile tests of the rotation speed set, axial force set and substrate temperature set are shown. A higher rotation speed shows a decline in the ultimate tensile force(UTF) of the bonding directly after 450 RPM. The reason for this is that higher rotation speeds cause more vibrations in the bonding process resulting in a more unstable bonding process. Therefore the chance for voids and cracks in the deposit is more for higher rotation speeds resulting in a lower the UTF.

At the axial force set the tensile force first has a marginal rise, than levels and finishes with a steep drop. No process explanation could be found for the marginal difference in the ultimate tensile force of the 5kN and 7.5kN test. The difference is more likely to be caused by the scatter of the data and the small data pool. The steep drop of the ultimate tensile force can be explained by the process stability. When the axial force was higher than 10kN the process was notable more unstable. Therefore more voids and cracks could be formed resulting in a lower UTF.

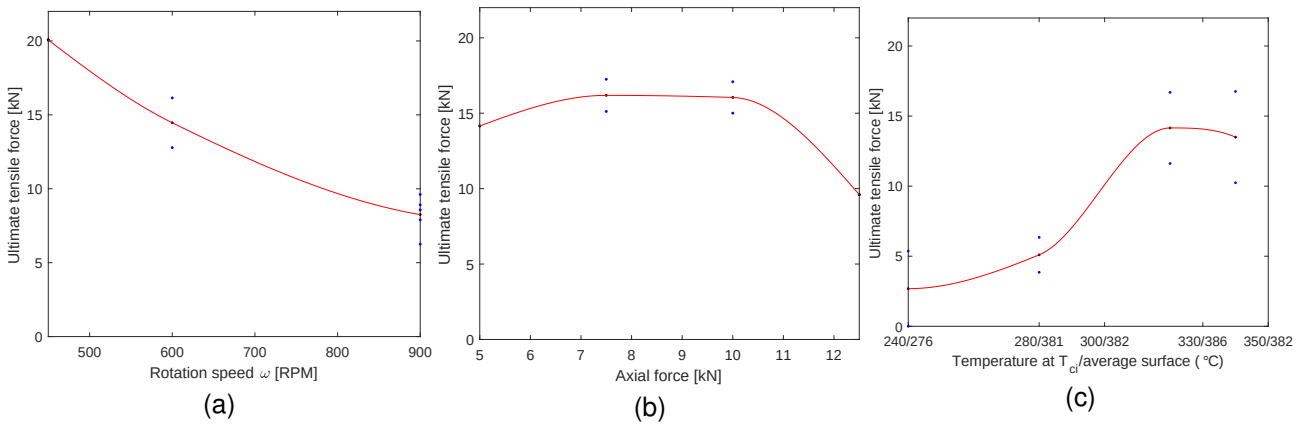

Figure 5.12: *Ultimate tensile strength versus: (a) the rotation speed (F=5kN till the maximum temperature), (b) applied axial force(ω=450RPM till the maximum temperature) and (c) the maximum temperature at the thermocouple location(F=5kN ω=450RPM)*

For the substrate temperature the ultimate tensile force shows a minimum temperature that is required for bonding to be initiated in the bonding process and an absolute maximum that can be reached with the bonding process. The tensile force shows an exponential rise in the beginning, has a maximum just before the temperature of global plastic deformation is reached and then shows a small decline before the maximum temperature is reached. Higher substrates temperature have a higher contact surface temperature but also more time for the bonding process because those experiments were stopped later. This allowed the true bonded surface to rapidly increase explaining the exponential rise. The small drop after the maxim ultimate tensile force can be explained by global plastic deformation at the substrate temperature of 350 °C. The global plastic deformation allows for a more inhomogeneous bonding resulting in a lower ultimate tensile force than the substrate of 330 °C that is still in stage II. Notable is that the maximum temperature of the contact surface is almost reached when the temperature at the thermal couple location is still at 280°C. This shows that in the bonding process it is not only important to reach a certain contact area temperature, but a certain amount of time is needed to maximize the bonding UTF.

Chapter 6

Discussion

The goal of this study is to understand the bonding process of aluminium 2024-T351 onto aluminium 2024-T351 and to find the parameters that give the optimal bonding. So that this information could be used to improve the design of the new Solid State Additive Manufacturing(SSAM) process. The main variables that influence the bonding are the process and tool design parameters. This study focused on the process parameters rotation speed and axial force. The influence of the surface temperature was also thoroughly investigated. The influence of these parameters have been analysed experimentally, numerically and analytically to study the effects on the Friction Surfacing (FS) heat generation, bonding process and bonding quality.

6.1 The bonding process

The experiments showed that the transient part of the bonding process can be divided into four stage. Stage I_a, the process is started shortly after the temperature and the axial force reach a plateau. Stage I_b, both the temperature and the applied torque suddenly rises. Stage II, local plastic deformation at the mechtrode has been observed, a peak has been reached at the applied torque and is starting to drop and the temperature is starting to level off. Stage III, the temperature is levelled and plastic deformation is observed around the whole contact surface.

The thermo-mechanical model showed that the transition of stage I_a to I_b is caused by the temperature saturation of the surrounding material, causing lower temperature gradient, and a gradual rise of the friction coefficient versus temperature. Resulting in a sudden rise of the temperature. The calculated effective friction coefficient versus the simulated average temperature of the contact area supports this theory with the lack of sudden rise at the temperature of the contact area between stage I_a to I_b, see Figure 4.11. The reason why the transition happens at a surface temperature of approximately 160 °C and if this happens at the same temperature when the initial condition are changed e.g. the geometry or the material, has not been researched in this thesis and is left for further research.

The rise of the friction coefficient and thus the heat flux in stage I_a and I_b can be explained based on the effective contact surface. The friction coefficient is dependent of the surface made with the contact asperities. The heat generated by the frictional stresses, lowers the shear stress of the materials and causes local deformation that destroys the peaks increasing the effective surface. An increase of the effective surface results in an increase in the friction coefficient, explaining the rise of the friction coefficient stage I_a and I_b.

In stage II, the start of local plastic deformation was observed at the moment the torsion showed a peak maximum. The peak could be well approximated by an analytical equation combining Coulomb's law of friction and the flow stress of the material with a slip/stick coefficient used by D. lohwasser et al.[32] and H. Schmidt et al. [33]. By assuming an exponential decline in the slip/stick coefficient, the absolute value of the peak could be accurately predicted. The peak did show a small lag in comparison to the the real peak. An explanation for this could be that stage II is reached a fraction earlier than was observed with the camera recordings.

The analytical equation showed that stage III can be really well approximated by the global plastic deformation using the flow stress values found in literature. However, for the flow stress the biggest strain rate(between 10 and 100s^{-1}) and strain(0.5) was assumed. While this is the case for the tested rotation speed, this could be different if lower rotation rates are tested in the future and should be considered.

6.2 Numerical solutions

The thermo-mechanical model showed that an accurate temperature distribution using the torque determined from the experiment as input is possible. However, the accuracy of the distribution has been solely checked with the thermocouples values. During the experiments it was observed that the thermocouples did not always made full contact with the substrate. This could lead to inaccuracies of the simulated temperature distribution because these are used as a control. This will be discussed later in this section.

In the model two different types of heat distributions have been tested. It is possible that the real heat distribution is different. However, the effect between the two tested heat distribution was marginal in the temperature distribution result, so it is expected that using a different type of heat distribution will hardly lead to more accuracy and will therefore be an unnecessary precaution.

On the other hand, the radius the heat was applied on did show a major influence. A difference of 2mm in radius could cause a difference in the simulated temperature of approximately 150 °C at the thermal couple location. In the model two different tests have been tried and both showed a relation between the observed radius in the cross sections and the effective radius that caused the best result in the temperature at the thermocouple locations. Note for the outside thermocouple at test 44 a marginal different radius gave better result than for the inside thermocouple. While for test 43 the radius that gave the best result was the same for the inside as outside thermocouple. Aside from the reasons of error already stated in Chapter 4 this could also be caused by inaccuracies of the measurement itself due to an imperfect contact of the thermocouple with the substrate. The peaks of the thermocouple measurements could suggest this. Therefore considering the sensitivity of the temperature towards the effective radius, the circumstance the experiments have been performed at, and the difficulty of defining the radius in the cross sections, more research is needed to validate and find the true relation.

The model allowed the effective friction coefficient to be plotted versus the average contact area temperature. The effective friction coefficient of the 5kN test showed a disturbance at approximately 160 °C before rising further. F. Wideroe [36] showed that sticking friction occurs when aluminium is heated. He found that if the ratio of the normal contact pressure and the characteristic shear strength $\frac{q}{k} \geq 0.7$ sticking occurs. The 5kN test had a ratio, for R=0.0086m, of approximately 0.1 at the point when the average temperature reached 160 °C. Also the tensile test showed that higher average surface temperatures were needed for the mechtrode to stick to the substrate. Finally the 14kN test did not show a similar disturbance. Therefore it is very unlikely that the disturbance followed by a rise of the friction coefficient is caused by a sticking phenomena.

The effective friction coefficient of the 5kN and 14kN test had a maximum of 1.4 and 1.2. Considering the sensitivity towards the effective radius and that both tests had an entirely different effective radius shows that there is a relation between the effective radius, the applied parameters and the effective friction coefficient. However, due that only two tests have been investigated in this way and the circumstances the measurements of the test have been performed at, more research is needed to map the effective friction coefficient versus the changes in parameters.

A difference of the effective friction coefficient of the 5kN and 14kN test is the maximum temperature before the drop is observed. In the 5kN test the maximum temperature is lower than the 14kN test. Considering the Von Mises criterium and the ratio $\frac{q}{k}$ the plastic deformation should occur at a lower temperature for higher axial forces. Therefore it is expected that the drop in the effective friction coefficient should be at lower temperature for the 14kN than the 5kN test. Instead the opposite has been observed. Whether this result is found incidental due to the experimental procedure or it is an occurring phenomena could not be determined yet. To find the explanation of this observed difference more research is needed.

Finally, at this stage the analytical prediction of the heat flux is only possible if tests with a constant force are used in this thermo-mechnical model. For the prediction of heat fluxes in tests with no constant force, the thermal-mechanical model needs to add another physic that allows the calculation of the force equilibrium due to thermal expansion in the mechtrode and substrate. Also the behaviour of the friction coefficient needs to be properly mapped. As stated earlier, too few tests have been analysed to accurately predict the behaviour of the effective coefficient for changing parameters. And therefore friction coefficients found in one test can not be used in the prediction of tests with different parameters.

6.3 The bonding quality

The images of the light microscope showed that microstructure is in a general way similar to the findings of U. suhuddin et al. [31]. Based on the images of the light microscope a distinction could be made between the thermal mechanically effected zone (TMAZ) and the rest of the material. In the TMAZ a finer microstructure was found due to the recrystallization of FS process. A detailed study of the grain boundaries could not be made because the electron back scatter diffraction was not yet operational at the university of Twente. U. suhuddin et al. investigation was only focused on the mechtrode and the deposit and with a different mechtrode material. Considering the new SSAM process a grain boundary study focused on the substrate and deposit with the correct mechtrode material should be performed for a better understanding.

In the hardness distribution the heat affected zone was found. It turned out that the samples were to small for heat to not effect the material therefore no base material(BM) was found. Granda et al. [25] studied the hardness distribution of the FS using 6082-T6 as mechtrode and 2024-T3 as substrate. In their substrate HAZ no hardness lower than approximately 130HV was found. In the samples a substantial lower hardness values of 105HV have been found in the HAZ. An explanation for this is that the mechtrode in this study was stationary therefore the substrate was more exposed to heat thus precipitates grew more resulting in a higher hardness drop than observed in the experiments of J. Granda et al. Another reason is that the material of the mechtrode in this study has the same hardness as the substrate therefore forcing the TMAZ into the substrate. A similar argument could be made for the TMAZ that is observed in substrate in these experiments, while was not noted in the study of J. Granda et al. [25].

M.J. Jones et al. [13] Y.S. Sato [37] studied the hardness distribution of AA2024-T4 using a friction stir welding technique(FSW). In their study the hardness of the HAZ could be as low as 105HV. However, in their TMAZ return of the initial hardness of 140HV, through solving and natural ageing of precipitates, was found. In the samples of this study no return of hardness has been found in the TMAZ. An explanation could be that TMAZ in the samples of this study didn't reach the necessary temperature for precipitated to dissolve.

In this study it was found that higher axial forces generated higher heat fluxes which resulted in higher temperatures at the contact surface. The lower contact area temperature of the lowest axial force initiated the least amount of growth in precipitates resulting in the highest hardness of the axial force set in the TMAZ. However, the simulated temperature contour plot showed that high axial forces should produce high enough temperatures for precipitates to dissolve and to return to the initial hardness of 140HV according to study of Y.S. Sato [37]. No return of hardness has been observed in the higher axial force samples. An explanation is that the simulated temperature distribution in the TMAZ is an overestimation and the real temperature is too low for precipitates to dissolve.

In the tensile test results the influence of the axial force showed a relatively minor differences of the ultimate tensile force (UTF) for lower axial forces and a steep drop for the high axial force samples. The steep drop of the UTF cannot be explained with the drop in hardness only. An explanation for this is that the generation of the flash and deposit during stage II and III is more unstable for higher axial forces than for lower axial forces due to the lack of lateral confinement. Therefore the chance of cracks and voids in the deposit is more likely for higher axial forces resulting in a lower tensile strength. The new SSAM process will have a lateral confinement and therefore it is the expectation that this problem will not occur at higher compressive forces. It is also the expectation that lateral confinement and use of a rotation tool in the new SSAM process will enable high enough temperatures for precipitates to dissolve. Meaning that the lower tensile strength and hardness for higher compressive forces in the FS experiments do not have to hold for the new SSAM process.

For the contact surface temperature the hardness decreased with increasing temperature. The result of the hardness aligned with the precipitation theory found in the literature. However, the UTF showed an increase for an increasing temperature, showing that for the bonding of the mechtrode to the substrate higher temperatures perform better. The best bonding was found at the contact surface temperature just before and at the moment of the global plastic deformation. Because of this, it is impossible to avoid precipitate growth in the FS process. A solution for the new design could be raising the temperature in the TMAZ to allow dissolving of the precipitates, so that initial hardness could be returned through natural ageing. While the HAZ is cooled so that the precipitate growth is minimal.

For the rotation speed, higher speeds resulted in lower tensile strength. An explanation could be that higher rotation speeds create a more unstable process and therefore increase the chance for cracks and voids in the bonding were the failure could be initiated. When the trend line is observed it shows that further research in lower rotation speeds is interesting and could even give better results than seen in this research. In previous research by S. Liu [3] showed bonding is possible for Friction Surface cladding up to a minimum of 250RPM, showing that a potential better operation window is possible.

Attempts have been made to determine the maximum stress during the tensile tests. First, the effective radius was tried in a similar way as in the thermo-mechanical model. The calculated stress with the effective radius failed to give a conclusive result and only created a larger scatter of data. Another attempt was made determining the fracture plane area with microscope pictures. Unfortunately, based on the pictures the fracture plane was hard to see and this only amplified the scatter in the data and no conclusive results could be obtained. The large scatter in the tensile test data and the determination of the bonded area is mainly caused by the experimental process. In the experimental process the substrate is fixed in an arm that has play, this play al-

lows the substrate to vibrate that could result in different bonding strength for the same parameters tested. The mechtrode also failed to stop directly when the experimental process stopped. This could influence the result the bonding for example when different rotation speeds are tested. Finally, the process was stopped manually which resulted that no test was exactly the same. For a better determination of the maximum stresses, the experimental process should be improved first. Although no representative stress could be found, failure mode III showed that the bonding is sometimes stronger than the substrate and therefore the bonding process certainly has a high potential create a high quality bonding.

Chapter 7

Conclusions and recommendations

The bonding process of AA2024-T351 onto AA2024-T341 and the bonding quality has been investigated using a friction surfacing process. The study comprises experimental, analytical and numerical work to see the influence of the rotation speed, axial force and surface temperature on the bonding process and quality. The main conclusions drawn in this study are presented in the first section. The second section will be dedicated to recommendations for future research in this field.

7.1 Conclusions

The bonding process

- The transient part of the bonding process can be divided into four stage. Stage I_a, the process is started shortly after the temperature and the axial force reached a plateau. Stage I_b, both the temperature and the applied torque suddenly rises. Stage II, local plastic deformation starts at the edges of the mechtrode, a peak is reached at the applied torque and is starting to drop, the temperature is starting to level. Stage III, plastic deformation happens around the whole contact surface, the temperature no longer rises and in some cases even declines.
- Stage I_a and I_b is characterized by full slipping. The sudden rise in temperature is caused by the temperature saturation of the surrounding material, causing lower temperature gradient, and a gradual rise of the friction coefficient versus temperature.
- Stage II is a mix of slip and sticking. An analytical equation combining coulomb's law of friction and the yield flow stress of the material was able to describe the slip-stick behaviour in stage II. An exponentially declining slip/stick-ratio gave the best result in predicting the heat flux, due to a gradual transfer from slip to stick conditions.
- Stage III is characterized by full sticking, the rise of the contact area is caused by the substrate that is better in conducting heat away in comparison to the mechtrode.
- An increase of the rotation speed created an increase in the heat flux. The higher heat flux causes all the previously stated stages to take less time.
- An increase of the axial force results in an increase in the heat flux. The higher heat flux causes all the previously stated stages to take less time. For axial forces higher than 14kN the heat flux in the beginning is too high and stage I_a is skipped.

Numerical solutions

- It is possible to create a model that is able to accurately predict the measured temperature at the thermocouples for a FS process, using the measured torque as input.
- The influence of the type of heat distribution is marginal. The best result was found with a zero order distribution.
- The influence of the effective radius the heat was applied on, was substantial. A relation was found between the applied effective radius and the radius of the bonding measured in the cross sections of the bonding.

The bonding quality

- The FS process shows lower hardness values than a FSW process with the same material and parameters.
- Lower axial forces create higher hardness distribution, because higher axial create only enough heat for precipitate growth. Dissolving of precipitates, as happens in FSW, has not been observed.

- Higher axial forces created a drop in the tensile strength of the bonding, because higher axial forces create a more unstable fusion process, due to the lack of lateral confinement, allowing more cracks and voids to appear in the bonding.
- Higher rotation speeds create a lower tensile strength, because higher rotation speeds create a more unstable fusion process allowing more cracks and voids to appear in the bonding.
- The best tensile strength of the bonding is achieved if the surface temperature is high enough for local or global plastic deformation. The surface temperature has to reach at least 360°C for bonding to be set.

7.2 Recommendations

At this stage the research explained the working mechanism of the process and showed the influence of the parameters on the bonding quality. Recommendations have been formulated to extend the current understanding of the process and to translate the FS to the new SSAM process.

- The result of the researched experiments showed a relation between the measured bonded width and the effective radius the heat is applied on in the simulations. However, too few test have been performed to find a conclusive result for this relation. In order to find this relation more test should be performed.
- The friction coefficient has been mapped versus the simulated average surface temperature and showed a lot of similarities between the tests. However, more research is needed for the results to be conclusive and to be used in prediction models for tests with different parameters.
- So far the thermo-mechanical model is only able to make prediction of the heat flux if the tests are performed at a constant force. The thermo-mechanical model needs to apply another physic that is able to calculate the force equilibrium caused by the thermal expansion of the substrate and mechtrode to predict the heat flux for test with no constant applied force.
- Low rotation speeds showed the best result for the tensile strength. In this research the lowest rotation speed was 450 RPM the relation of the tensile strength showed that research in lower rotation speeds could be worthwhile.
- The play of the experimental setup caused vibrations in the experiments that were likely one of the causes for inconsistencies in the bonding quality. In future research setup with a higher stiffness is advised.
- The start and stop procedure had to be performed manually. Hence, none of the experiments in the data sets had the exact same rotation time. The difference of rotation time could have influenced the bonding quality results. Therefore it is recommended that in future research this procedure is automated to produce data with exactly the same rotation time.
- In FS higher compressive forces resulted often in a lower quality of the bonding. This was mainly caused by the lack of lateral confinement. In the new SSAM process the lateral confinement will not be a problem and higher compressive forces could be a solution for enough heat to dissolve the precipitates and increase the hardness of the TMAZ through natural ageing. Therefore the higher compressive force should be reconsidered when research is performed with the new PT setup.
- The prediction of the precipitate growth in the samples in this research has been based on the simulated temperature and the literature research findings. However, the behaviour of the precipitates is very sensitive to thermal history of the sample. Therefore it is recommended that the samples in future research should be investigated with a EBSD and TEM study to explain the behaviour of the precipitates in the different samples.

References

[1] W.E. Frazier. Metal additive manufacturing: A review. *Journal of Materials Engineering and Performance*, 23(6):1917–1928, 2014.

[2] H.A. El-Hafez. Mechanical properties and welding power of friction stirred aa2024-t35 joints. *Journal of Materials Engineering and Performance*, 20(6):839–845, 2011. cited By 10.

[3] S. Lui. Friction surface cladding of aa1050 onto aa2024: Parameter study and process window development. 2016. ISBN: 978-90-365-4270-8.

[4] G.M. Karthik, G.D. Janaki Ram, and R.S. Kottada. Heat-affected zone liquation cracking resistance of friction stir processed aluminum-copper alloy aa 2219. *Metallurgical and Materials Transactions B: Process Metallurgy and Materials Processing Science*, 48(2):1158–1173, 2017. cited By 0.

[5] J. Gandra, H. Krohn, R.M. Miranda, P. Vilaa, L. Quintino, and J.F. dos Santos. Friction surfacinga review. *Journal of Materials Processing Technology*, 214(5):1062 – 1093, 2014.

[6] A.A. Van Der Stelt, T.C. Bor, H.J.M. Geijselaers, R. Akkerman, and A.H. Van Den Boogaard. Friction surface cladding: development of a solid state cladding process. 2014. ISBN: 978-94-91909-09-2.

[7] ALCOA MILL PRODUCTS. Alloy 2024 sheet and plate. http://www.millproducts-alcoa.com/, 2017.

[8] J.R. Davis. *Aluminum and Aluminum Alloys*. ASM international.

[9] Crp Meccanica. Aluminum 2024-t4; 2024-t351. http://www.matweb.com/, 2017.

[10] S. RIDDER F. BIANCANIELLO M. Rosen, L. IVES and R. MEHRABIAN. Correlation between ultrasonic and hardness measurements in aged aluminum alloy 2024. 1985.

[11] P. Carlone and G.S. Palazzo. Influence of process parameters on microstructure and mechanical properties in aa2024-t3 friction stir welding. *Metallography, Microstructure, and Analysis*, 2(4):213–222, 2013. cited By 31.

[12] S.A. Khodir, T. Shibayanagi, and M. Naka. Influence of friction stir welding parameters on microstructure and mechanical properties of aa2024-t3 aluminum alloy. *Ceramic Transactions*, 198:91–96, 2007. cited By 0.

[13] M.J. Jones, P. Heurtier, C. Desrayaud, F. Montheillet, D. Allehaux, and J.H. Driver. Correlation between microstructure and microhardness in a friction stir welded 2024 aluminium alloy. *Scripta Materialia*, 52(8):693–697, 2005. cited By 98.

[14] Y.S. Sato, S. Kurihara, and H. Kokawa. Systematic examination of precipitation phenomena associated with hardness and corrosion properties in friction stir welded aluminium alloy 2024. *Welding in the World*, 55(11-12):39–47, 2011. cited By 2.

[15] S.A. Khodir, T. Shibayanagi, and M. Naka. Control of hardness distribution in friction stir welded aa2024-t3 aluminum alloy. *Materials Transactions*, 47(6):1560–1567, 2006. cited By 5.

[16] Z. Zhang, W. Li, J. Li, Y.J. Chao, and A. Vairis. Microstructure and anisotropic mechanical behavior of friction stir welded aa2024 alloy sheets. *Materials Characterization*, 107:112–118, 2015. cited By 3.

[17] D.A. Porter and K.E. Easterling. Transformation in metal alloys, 1993. Second edition.

[18] R.C. Dorward and S.D. Kennedy. A method of manufacturing aluminum aircraft sheet, September 26 1996. WO Patent App. PCT/US1996/003,390.

[19] J.E. Hatch. *Aluminum: Properties and Physical Metallurgy*. ASM international.

[20] H.K. Khaira. Precipitation hardening. Power point presentation.

[21] MatWeb. Aluminum alloy heat treatment temper designations. http://www.matweb.com/reference/aluminumtemper.aspx, 2017.

[22] A. Lipski and S. Mroziski. The effects of temperature on the strength properties of aluminium alloy 2024-t3. *Acta Mechanica et Automatica*, 6(3):62–66, 2012. cited By 6.

[23] J.D. Seidt and A. Gilat. Plastic deformation of 2024-t351 aluminum plate over a wide range of loading conditions. *International Journal of Solids and Structures*, 50(10):1781–1790, 2013. cited By 16.

[24] Y.V.R.K. Prasad and S. Sasidhara. Hot working guide: second edition. 1997. ISBN:0-87170-598-2.

[25] J. Gandra, D. Pereira, R.M. Miranda, R.J.C. Silva, and P. Vilaa. Deposition of aa6082-t6 over aa2024-t3 by friction surfacing - mechanical and wear characterization. *Surface and Coatings Technology*, 223:32 – 40, 2013.

[26] E.D. Nicholas and W.M. Thomas. Metal deposition by friction welding. pages 87–89, 1986. cited By 0.

[27] A. van Kalken. Friction surfacing of stainless steel on mild steel with a robot. 2011.

[28] J. Gandra, R.M. Miranda, and P. Vilaa. Performance analysis of friction surfacing. *Journal of Materials Processing Technology*, 212(8):1676–1686, 2012. cited By 19.

[29] Mohammed Shariq, Madhulika Srivastava, Rupam Tripathi, Somnath Chattopadhyaya, and Amit Rai Dixit. Feasibility study of friction surfaced coatings over non-ferrous substrates. *Procedia Engineering*, 149:465 – 471, 2016.

[30] J. Gandra, D. Pereira, R.M. Miranda, and P. Vilaa. Influence of process parameters in the friction surfacing of aa 6082-t6 over aa 2024-t3. *Procedia CIRP*, 7:341 – 346, 2013.

[31] U. Suhuddin, S. Mironov, H. Krohn, M. Beyer, and J.F. Dos Santos. Microstructural evolution during friction surfacing of dissimilar aluminum alloys. *Metallurgical and Materials Transactions A: Physical Metallurgy and Materials Science*, 43(13):5224–5231, 2012. cited By 9.

[32] D. Lohwasser and Z. Chen. *Friction stir welding from basics to applications*. Woodhead publishing limited.

[33] H. Schmidt, J. Hattel, and J. Wert. An analytical model for the heat generation in friction stir welding. *Modelling and Simulation in Materials Science and Engineering*, 12(1):143–157, 2004. cited By 326.

[34] Engineersedge. Forced convection; moderate speed cross- flow of air over a cylinder. 2017.

[35] Shi Q.-Y. Dickerson, T. and H. R. Shercliff. Heat flow into friction stir welding tools. 2003. 4th Int. Symp. Frict. stir welding.

[36] F. Widere and T. Welo. Conditions for sticking friction between aluminium alloy aa6060 and tool steel in hot forming. *Key Engineering Materials*, 491:121–128, 2012. cited By 7.

[37] Y.S. Sato, S. Kurihara, and H. Kokawa. Systematic examination of precipitation phenomena associated with hardness and corrosion properties in friction stir welded aluminium alloy 2024. *Welding in the World*, 55(11-12):39–47, 2011. cited By 2.

[38] Yunus A. Cengel. *Heat and mass transfer*, chapter 4, page 251. Mc Craw Hill.

[39] Theo van de Meer. Transport phenomena:instationary diffusion. 2014.

Appendix A

Experiment I

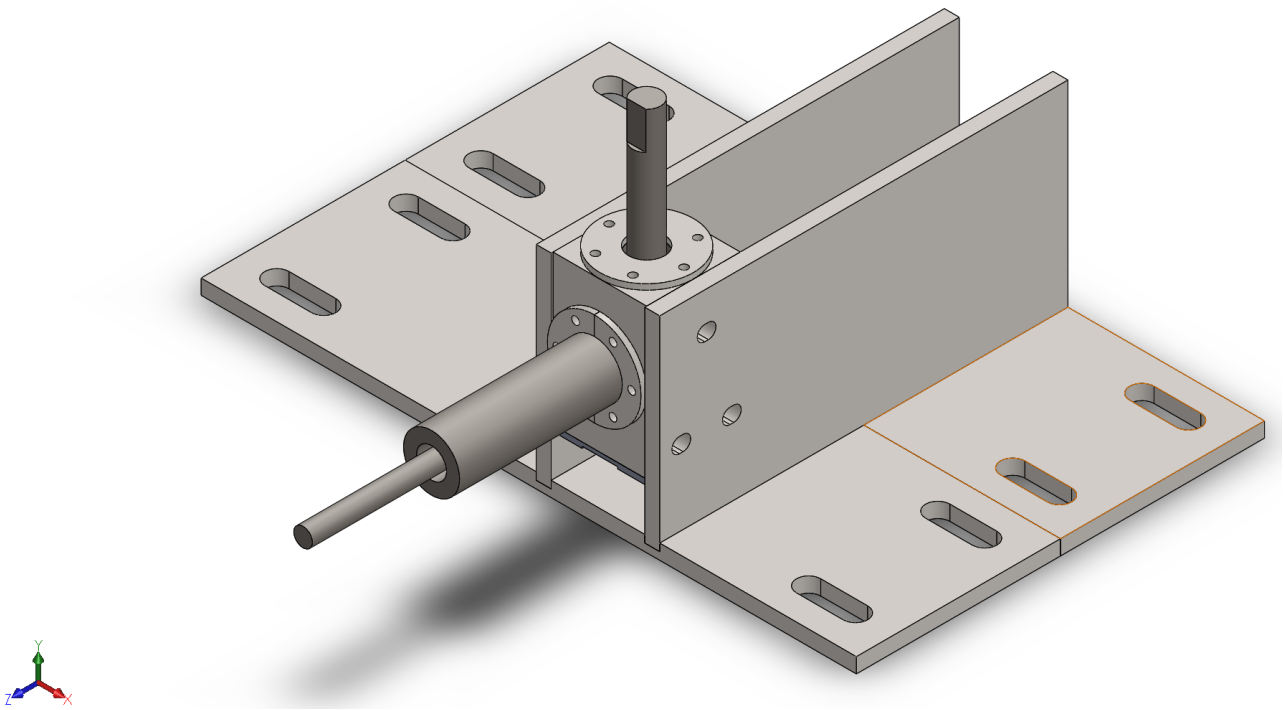

Figure A.1: *The first experimental setup. This experimental setup was used to find the feasibility of semi-continues SSAM.*

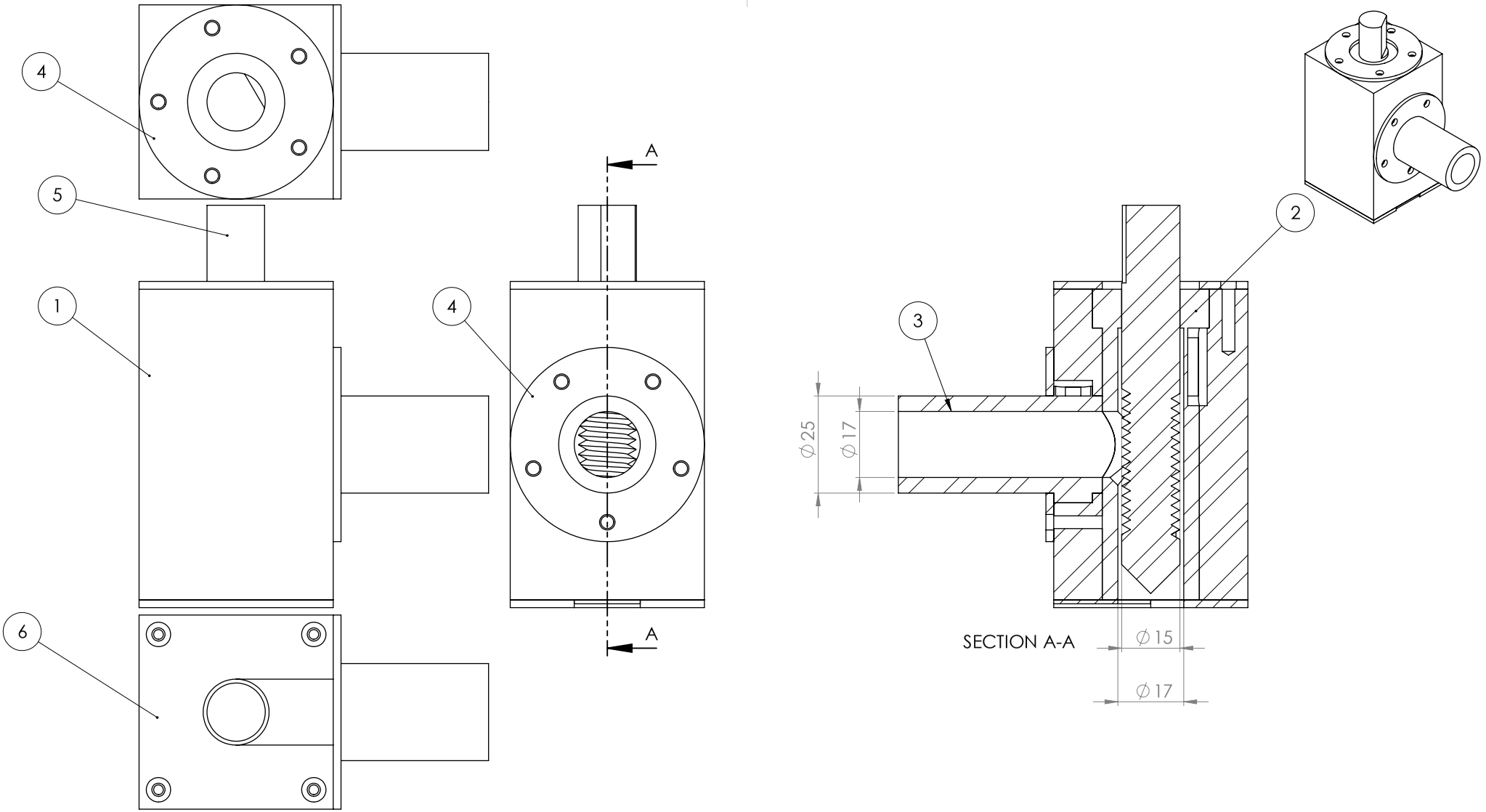

Stuk Nr.	Config I/QTY.	Benaming	Materiaal / Half fabrikaat	Norm of afmeting	Opmerking
6	1	Part6			
5	1	Part5			
4	2	Part4			
3	1	Part3			
2	1	Part1			
1	1	Part2			

PROJECTION METHOD

UNLESS STATED OTHERWISE: TOLERANCES ± 0,5 MM

DRAWN -- DATE 1-6-2016

CHECKED -- SCALE 1:1

MATERIAL -- --

SURFACE FINISH --

TITLE NO NAME

REV. 01

DRAWING NO. --

FILE / PART NAME Opstelling I

A3

UNIVERSITY OF TWENTE.

FACULTY OF ENGINEERING

DIMENSIONS IN MILLIMETERS

SHEET 1 OF 1

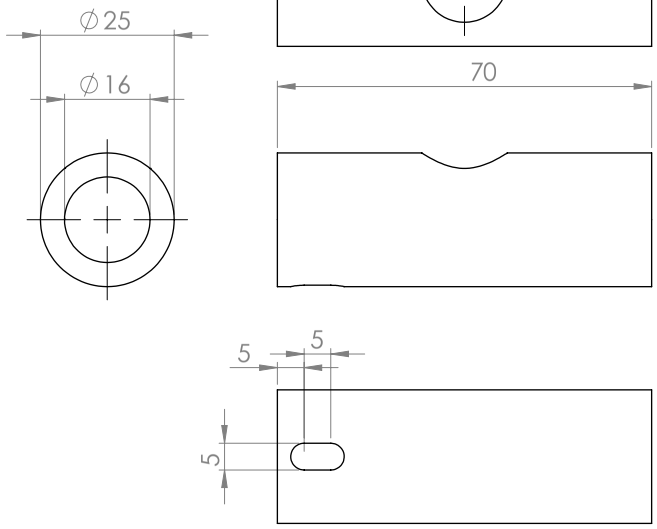

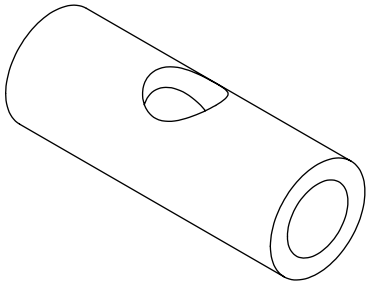

PROJECTION METHOD	UNLESS STATED OTHERWISE: TOLERANCES ± 0,5 MM	DRAWN	--	DATE	6-6-2016
		CHECKED	--	SCALE	1:1
MATERIAL: -- --	SURFACE FINISH: --	TITLE: NO NAME			REV.: 01
UNIVERSITY OF TWENTE.		DRAWING NO.: --			A4
		FILE / PART NAME: Part1			
FACULTY OF ENGINEERING		DIMENSIONS IN MILLIMETERS		SHEET 1 OF 1	

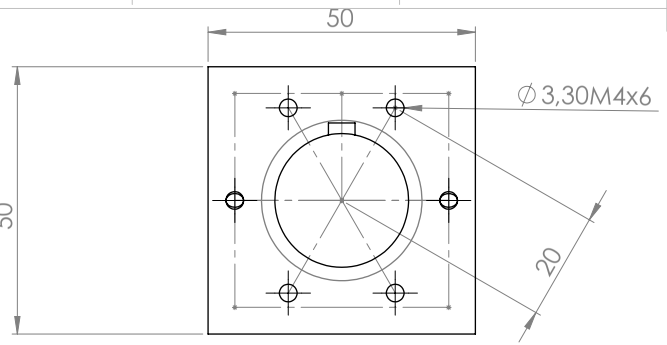

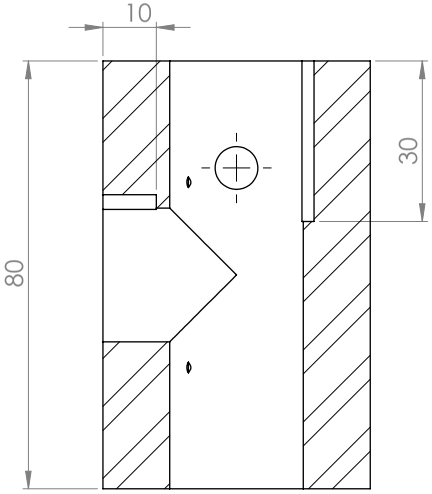

SECTION A-A

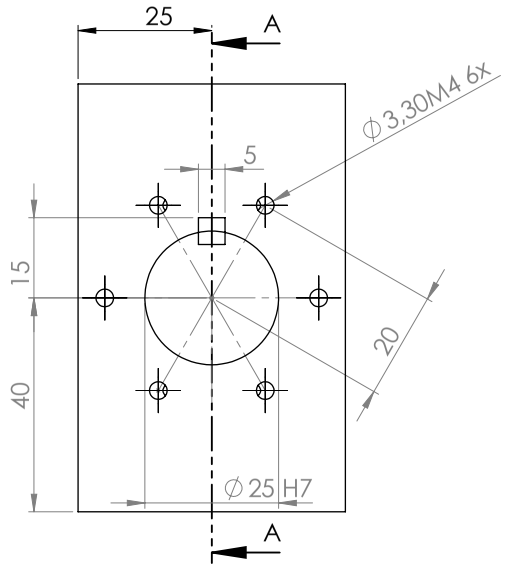

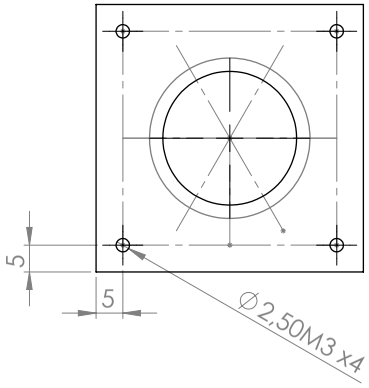

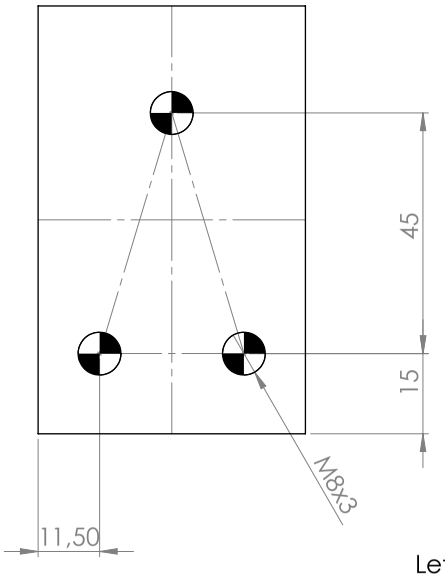

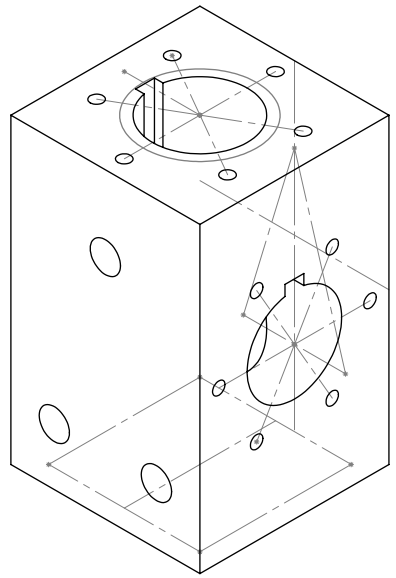

Let op: eerst horizontaal gat boren, dan part 3 erin zetten, dan verticaal gaat boren.

PROJECTION METHOD	UNLESS STATED OTHERWISE: TOLERANCES ± 0,5 MM	DRAWN	--	DATE	6-6-2016
		CHECKED	--	SCALE	1:1
MATERIAL: -- --	SURFACE FINISH: --	TITLE: NO NAME			REV. 01
UNIVERSITY OF TWENTE.		DRAWING NO.: --			A3
FACULTY OF ENGINEERING		FILE / PART NAME: Part2			
		DIMENSIONS IN MILLIMETERS			SHEET 1 OF 1

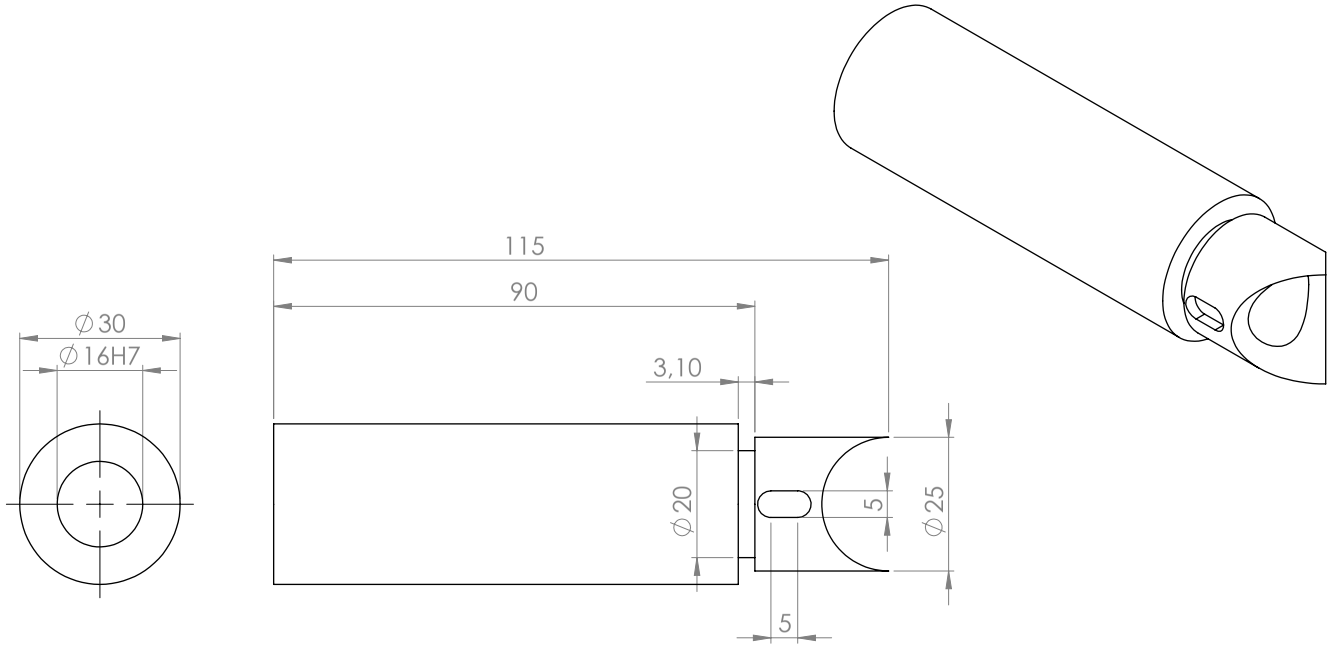

PROJECTION METHOD	UNLESS STATED OTHERWISE: TOLERANCES ± 0,5 MM	DRAWN	--	DATE	6-6-2016
		CHECKED	--	SCALE	1:1
MATERIAL: -- --	SURFACE FINISH: --	TITLE: NO NAME			REV.: 01
		DRAWING NO.: --			
UNIVERSITY OF TWENTE.		FILE / PART NAME: Part3			A4
FACULTY OF ENGINEERING		DIMENSIONS IN MILLIMETERS			SHEET 1 OF 1

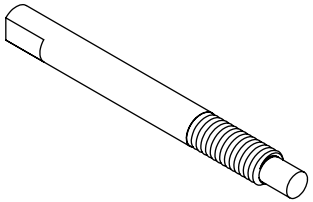

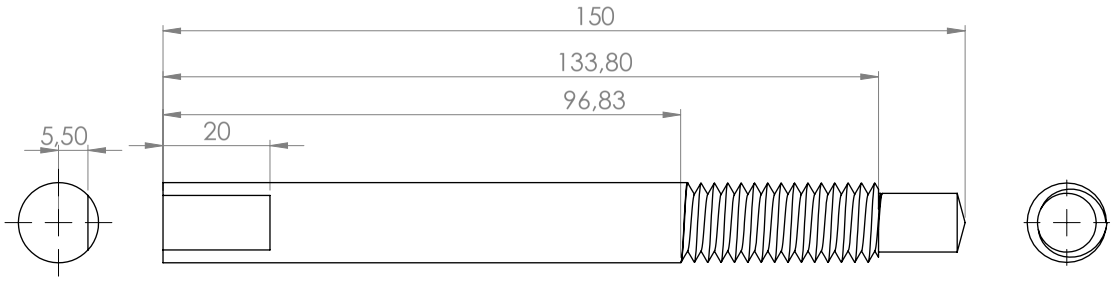

Opmerking:
Schroefdraad zo fijn mogelijk.

PROJECTION METHOD	UNLESS STATED OTHERWISE: TOLERANCES ± 0,5 MM	DRAWN	--	DATE	6-6-2016
		CHECKED	--	SCALE	1:1
MATERIAL: -- --	SURFACE FINISH: --	TITLE: NO NAME			REV.: 01
		DRAWING NO.: --			
UNIVERSITY OF TWENTE.		FILE / PART NAME: Part5			A4
FACULTY OF ENGINEERING		DIMENSIONS IN MILLIMETERS			SHEET 1 OF 1

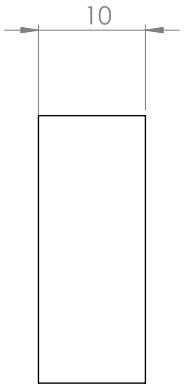

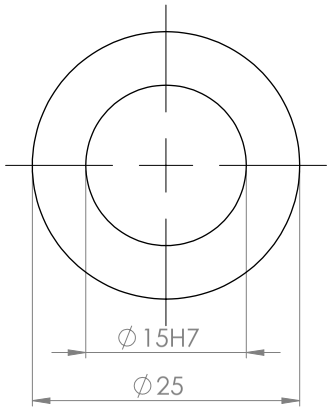

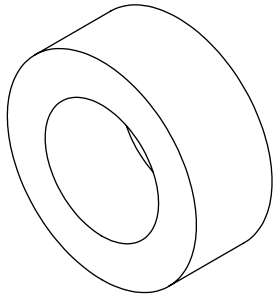

PROJECTION METHOD	UNLESS STATED OTHERWISE: TOLERANCES ± 0,5 MM	DRAWN	--	DATE	6-6-2016
		CHECKED	--	SCALE	2:1
MATERIAL -- --	SURFACE FINISH --	TITLE NO NAME			REV. 01
		DRAWING NO. --			
UNIVERSITY OF TWENTE.		FILE / PART NAME Part8			A4
FACULTY OF ENGINEERING		DIMENSIONS IN MILLIMETERS			SHEET 1 OF 1

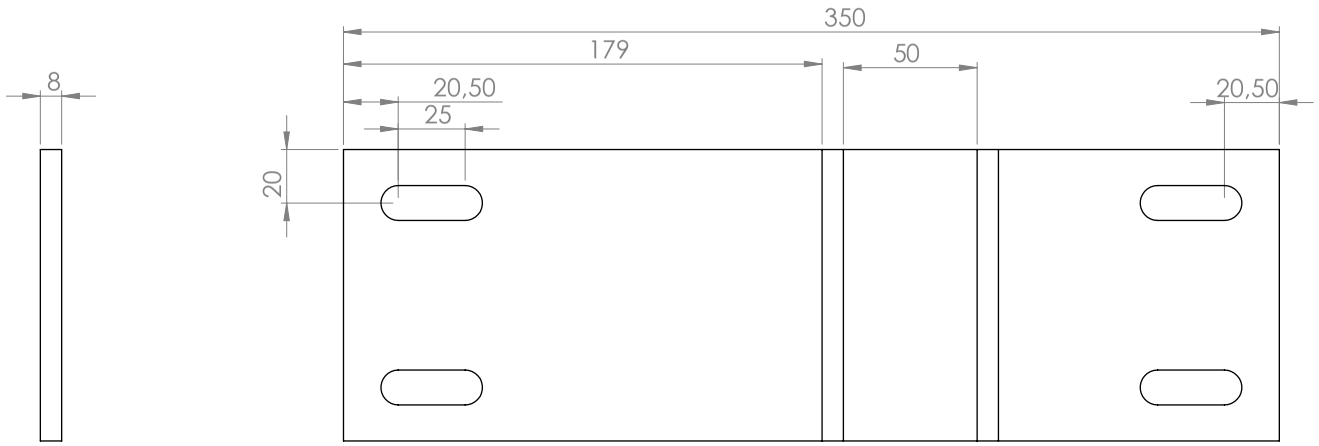

PROJECTION METHOD	UNLESS STATED OTHERWISE: TOLERANCES ± 0,5 MM	DRAWN	--	DATE	6-6-2016
		CHECKED	--	SCALE	1:2
MATERIAL: -- --	SURFACE FINISH: --	TITLE: NO NAME			REV.: 01
UNIVERSITY OF TWENTE.		DRAWING NO.: --			A4
FACULTY OF ENGINEERING		FILE / PART NAME: Part10			
		DIMENSIONS IN MILLIMETERS		SHEET 1 OF 1	

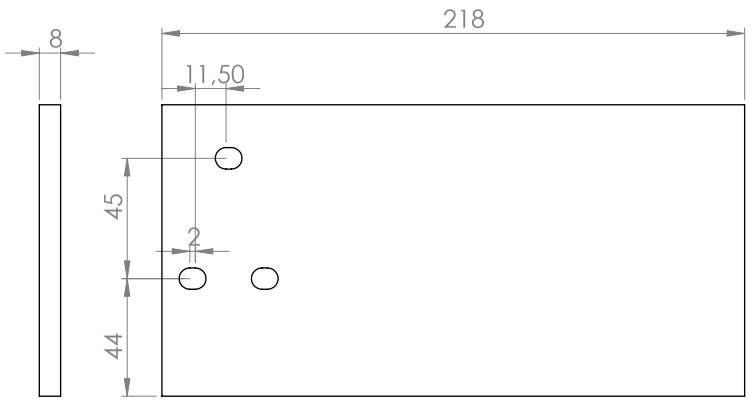

PROJECTION METHOD	UNLESS STATED OTHERWISE: TOLERANCES ± 0,5 MM	DRAWN	--	DATE	6-6-2016
		CHECKED	--	SCALE	1:2
MATERIAL -- --	SURFACE FINISH --	TITLE NO NAME			REV. 01
UNIVERSITY OF TWENTE.		DRAWING NO. --			A4
		FILE / PART NAME Part11			
FACULTY OF ENGINEERING		DIMENSIONS IN MILLIMETERS		SHEET 1 OF 1	

Appendix B

Experiment II

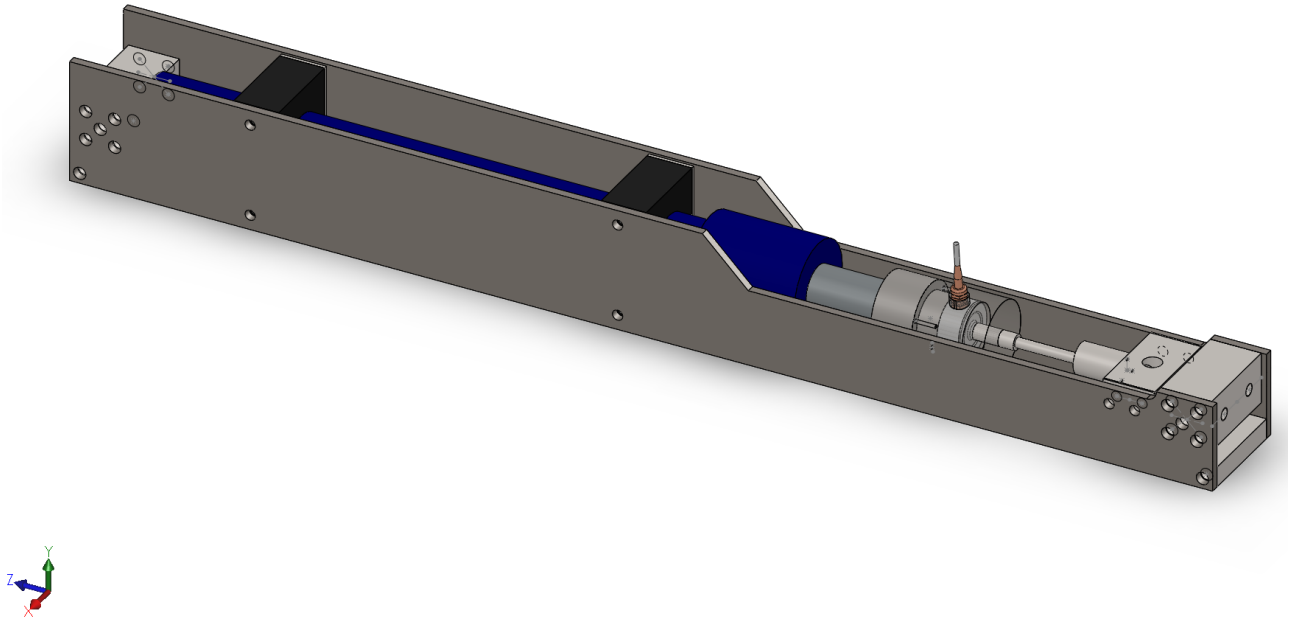

Figure B.1: *The second experimental setup. This experimental setup was used to find the feasibility of semi-continues SSAM.*

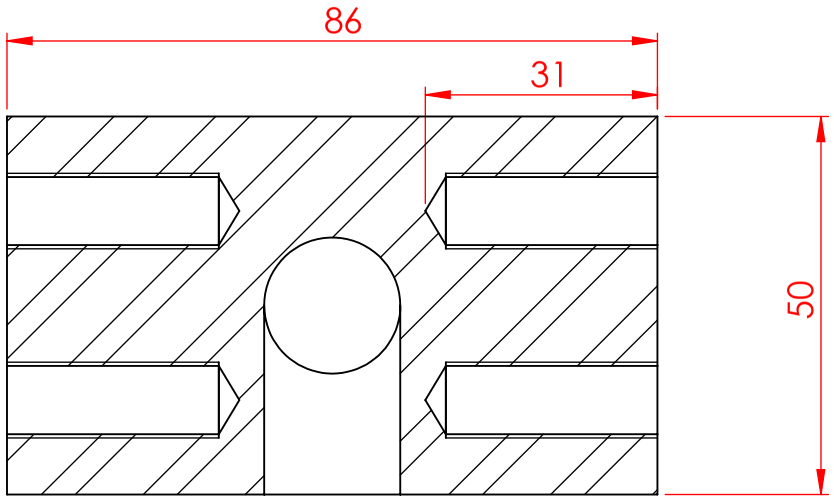

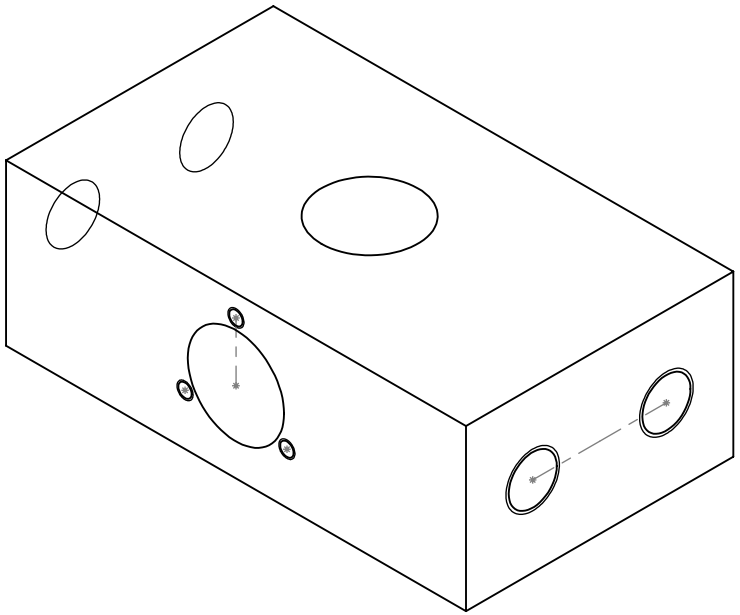

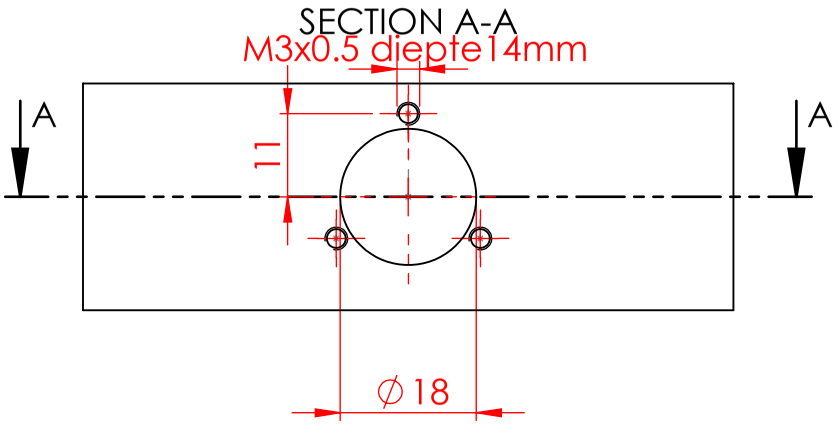

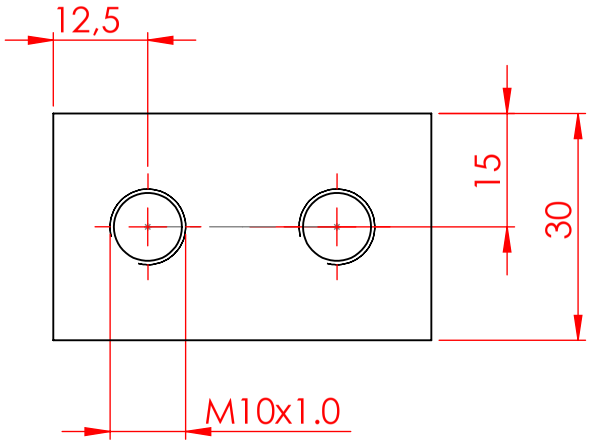

PROJECTION METHOD	UNLESS STATED OTHERWISE: TOLERANCES ± 0,5 MM	DRAWN	--	DATE	11-8-2016
		CHECKED	--	SCALE	1:1
MATERIAL: -- --	SURFACE FINISH: --	TITLE: NO NAME			REV.: 01
		DRAWING NO.: --			
UNIVERSITY OF TWENTE.		FILE / PART NAME: Part1			A4
FACULTY OF ENGINEERING		DIMENSIONS IN MILLIMETERS			SHEET 1 OF 1

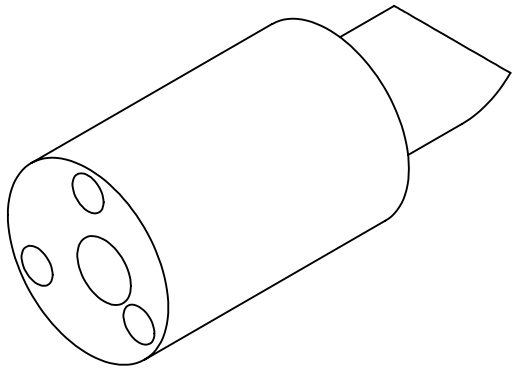

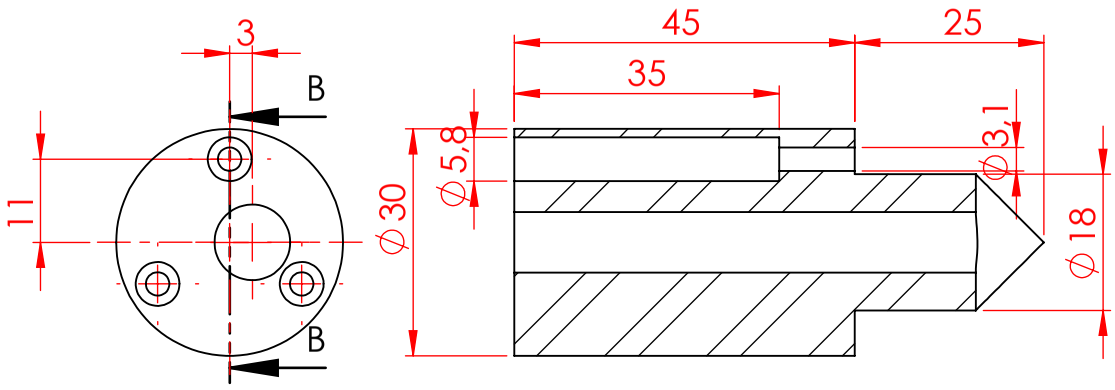

SECTION B-B

PROJECTION METHOD	UNLESS STATED OTHERWISE: TOLERANCES ± 0,5 MM	DRAWN	--	DATE	11-8-2016
		CHECKED	--	SCALE	1:1

MATERIAL: -- --	SURFACE FINISH: --	TITLE: NO NAME	REV.: 01
		DRAWING NO.: --	
UNIVERSITY OF TWENTE.		FILE / PART NAME: Part2	A4
FACULTY OF ENGINEERING		DIMENSIONS IN MILLIMETERS	SHEET 1 OF 1

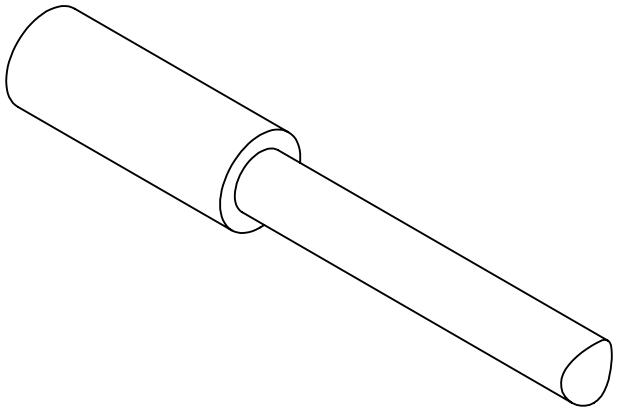

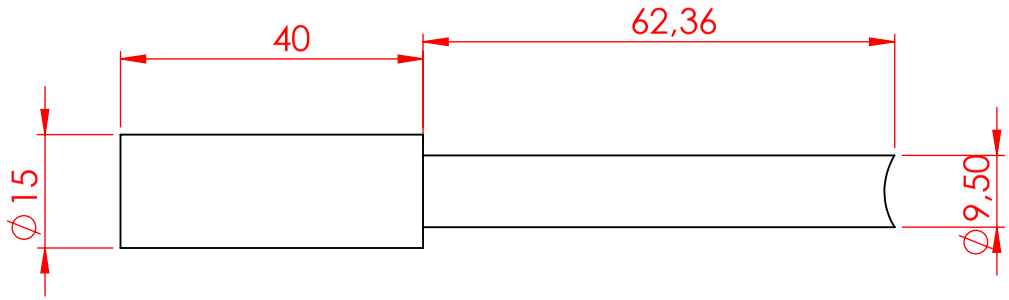

PROJECTION METHOD	UNLESS STATED OTHERWISE: TOLERANCES ± 0,5 MM	DRAWN	--	DATE	11-8-2016
		CHECKED	--	SCALE	1:2
MATERIAL -- --	SURFACE FINISH --	TITLE NO NAME			REV. 01
UNIVERSITY OF TWENTE.		DRAWING NO. --			A4
		FILE / PART NAME Part4			
FACULTY OF ENGINEERING		DIMENSIONS IN MILLIMETERS			SHEET 1 OF 1

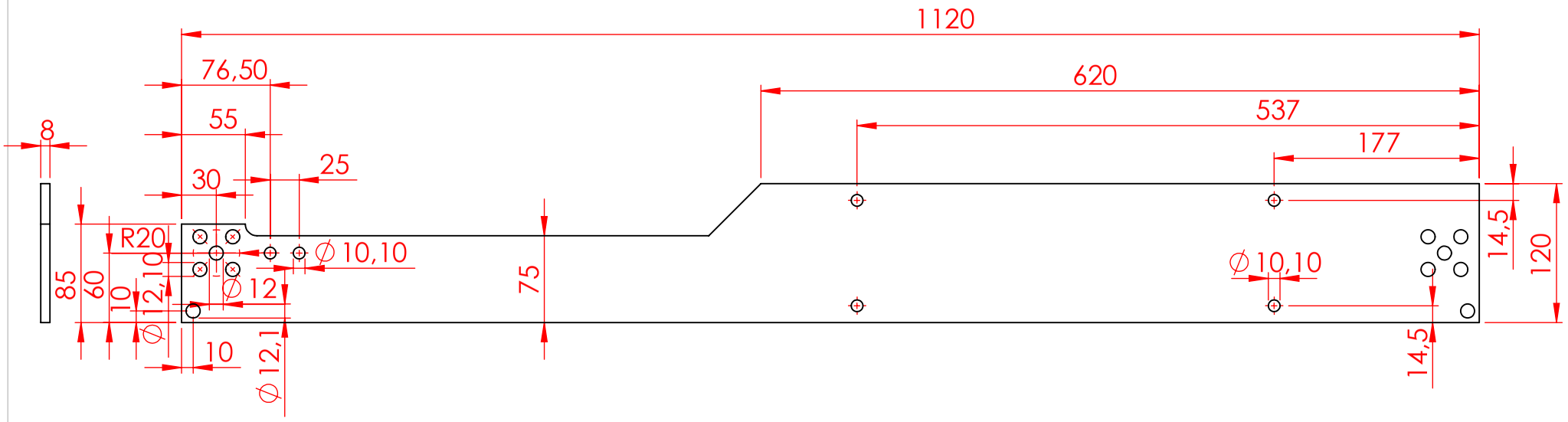

PROJECTION METHOD	UNLESS STATED OTHERWISE: TOLERANCES ± 0,5 MM	DRAWN	--	DATE	11-8-2016
		CHECKED	--	SCALE	1:5

MATERIAL	SURFACE FINISH	TITLE	REV.
--	--	NO NAME	01
--		DRAWING NO. --	
UNIVERSITY OF TWENTE.		FILE / PART NAME Part5	A4
FACULTY OF ENGINEERING		DIMENSIONS IN MILLIMETERS	SHEET 1 OF 1

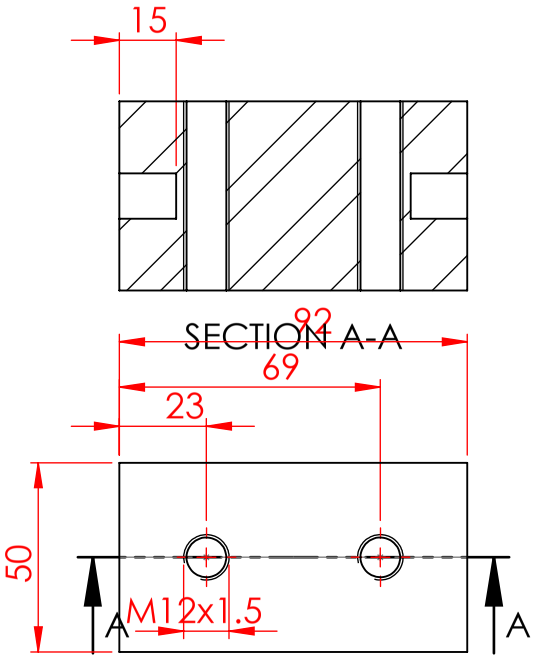

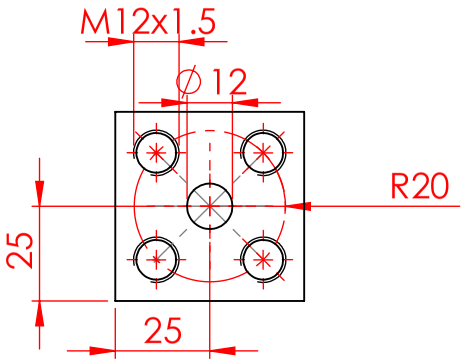

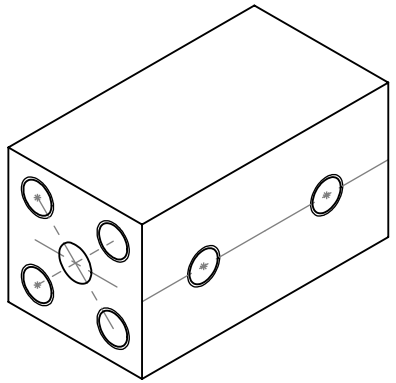

PROJECTION METHOD	UNLESS STATED OTHERWISE: TOLERANCES ± 0,5 MM	DRAWN	--	DATE	29-8-2016
		CHECKED	--	SCALE	1:2
MATERIAL: -- --	SURFACE FINISH: --	TITLE: NO NAME			REV.: 01
		DRAWING NO.: --			
UNIVERSITY OF TWENTE.		FILE / PART NAME: Part9			A4
FACULTY OF ENGINEERING		DIMENSIONS IN MILLIMETERS			SHEET 1 OF 1

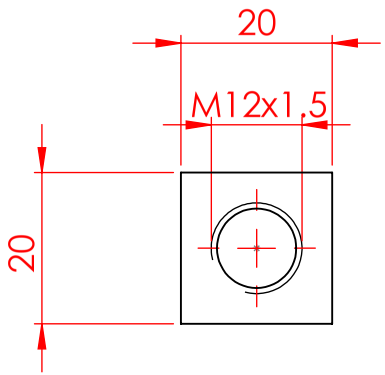

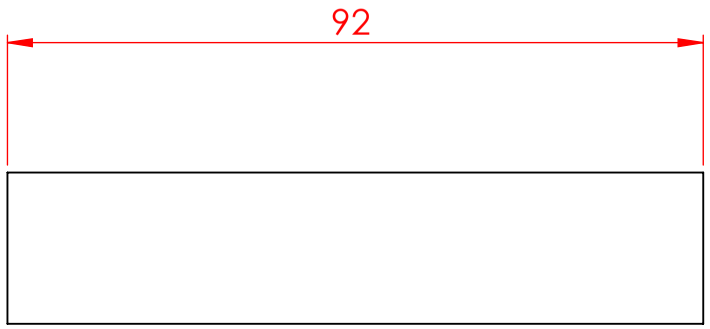

PROJECTION METHOD	UNLESS STATED OTHERWISE: TOLERANCES ± 0,5 MM	DRAWN	--	DATE	29-8-2016
		CHECKED	--	SCALE	1:1
MATERIAL: -- --	SURFACE FINISH: --	TITLE: NO NAME			REV.: 01
		DRAWING NO.: --			
UNIVERSITY OF TWENTE.		FILE / PART NAME: Part10			A4
FACULTY OF ENGINEERING		DIMENSIONS IN MILLIMETERS			SHEET 1 OF 1

Appendix C

Experiment III

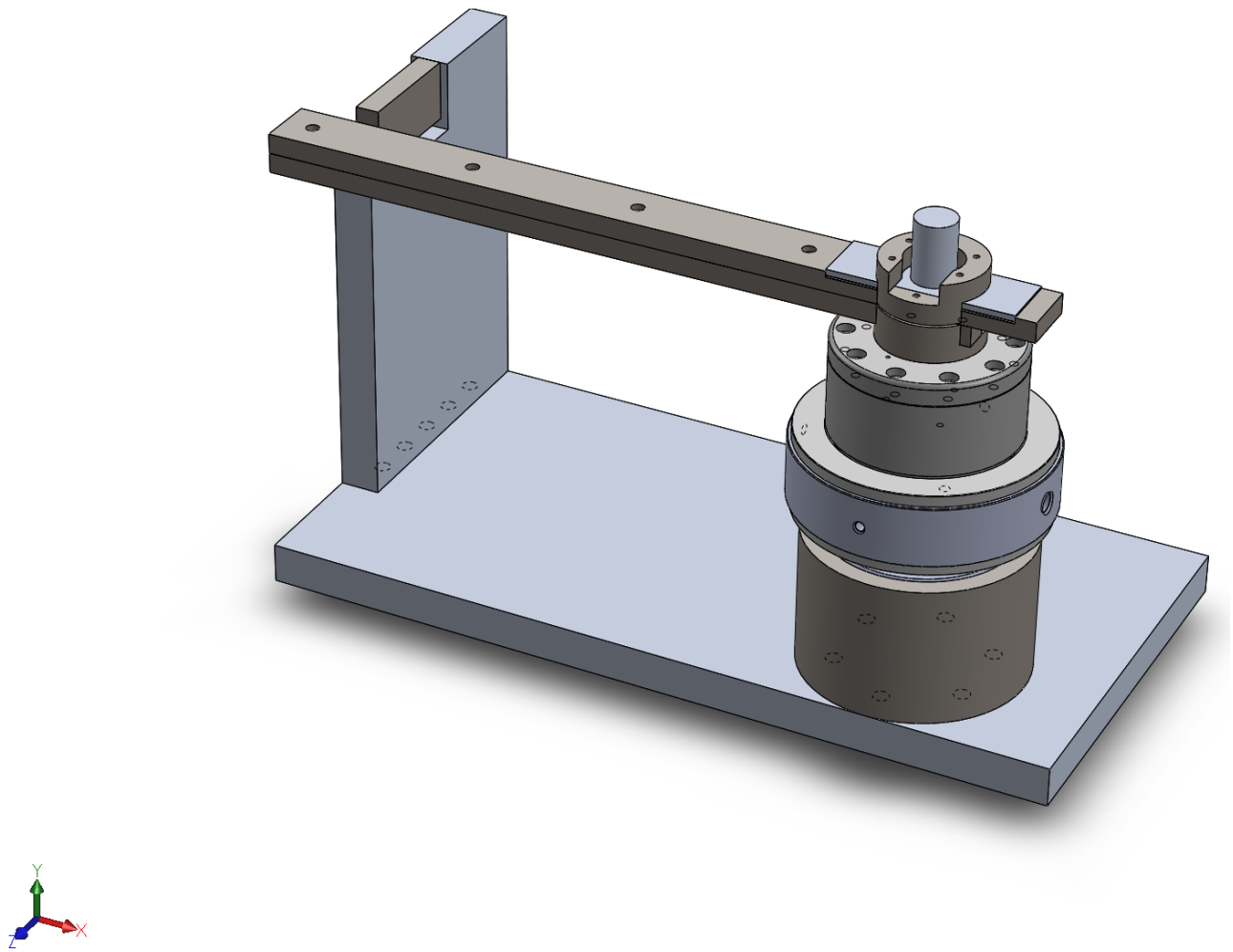

Figure C.1: *The third experimental setup. The experimental setup that was used in this thesis to create an understanding of the bonding process of aluminium 2024-T351*

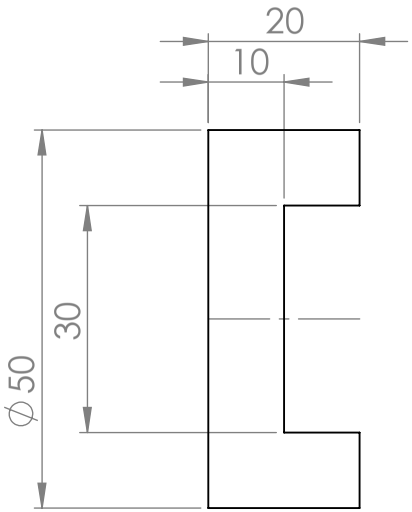

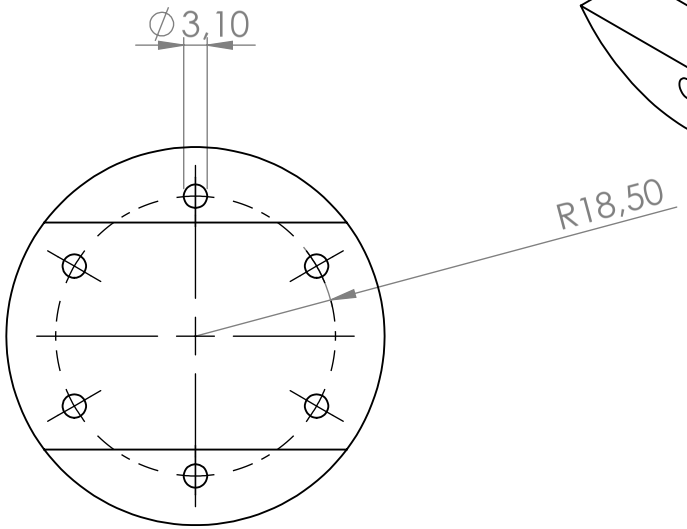

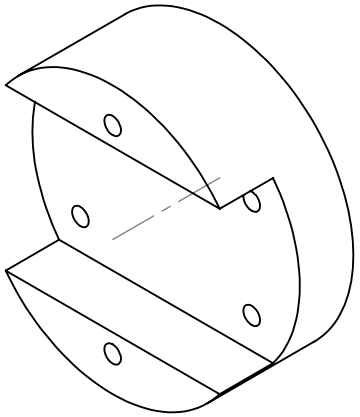

PROJECTION METHOD	UNLESS STATED OTHERWISE: TOLERANCES ± 0,5 MM	DRAWN	--	DATE	28-10-2016
		CHECKED	--	SCALE	1:1
MATERIAL: -- --	SURFACE FINISH: --	TITLE: NO NAME			REV.: 01
		DRAWING NO.: --			
UNIVERSITY OF TWENTE.		FILE / PART NAME: Part1new			A4
FACULTY OF ENGINEERING		DIMENSIONS IN MILLIMETERS			SHEET 1 OF 1

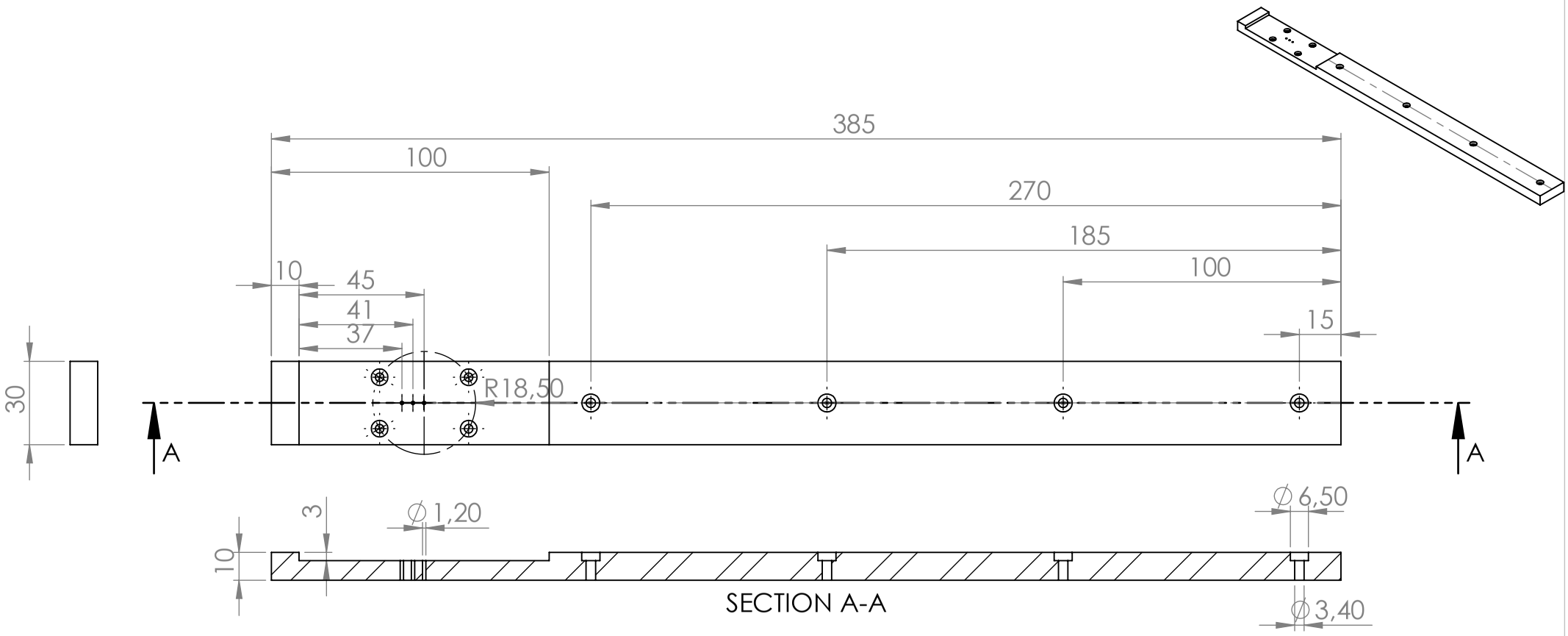

PROJECTION METHOD	UNLESS STATED OTHERWISE: TOLERANCES ± 0,5 MM	DRAWN	--	DATE	28-10-2016
		CHECKED	--	SCALE	1:2

MATERIAL -- --	SURFACE FINISH --	TITLE NO NAME	REV. 01
		DRAWING NO. --	
UNIVERSITY OF TWENTE.		FILE / PART NAME Part2new	A4
FACULTY OF ENGINEERING		DIMENSIONS IN MILLIMETERS	SHEET 1 OF 1

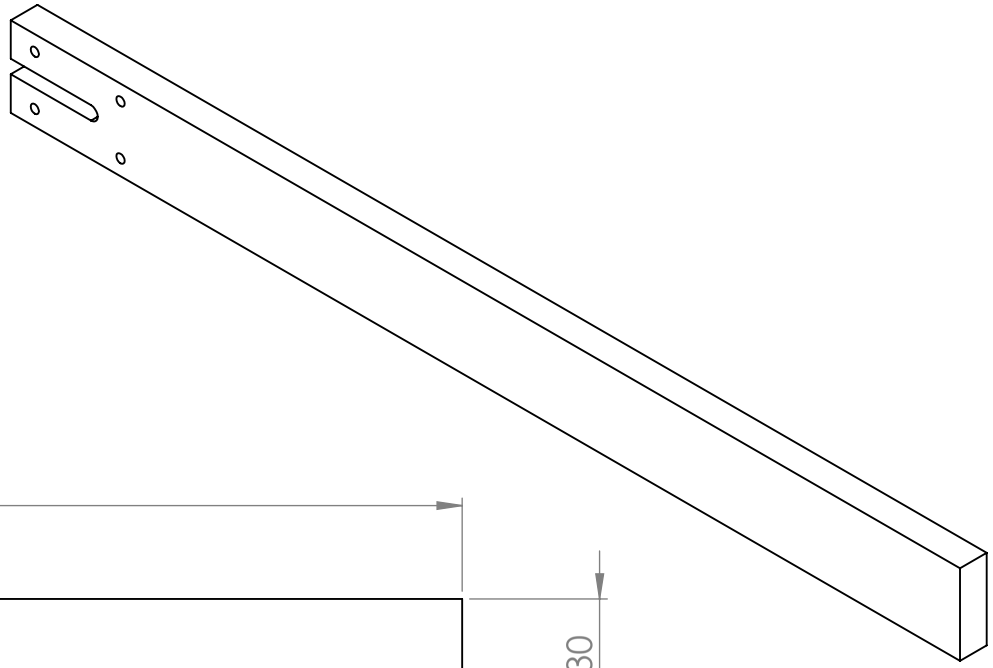

PROJECTION METHOD	UNLESS STATED OTHERWISE: TOLERANCES ± 0,5 MM	DRAWN	--	DATE	28-10-2016
		CHECKED	--	SCALE	1:2
MATERIAL: -- --	SURFACE FINISH: --	TITLE: NO NAME			REV.: 01
		DRAWING NO.: --			
UNIVERSITY OF TWENTE.		FILE / PART NAME: Part3new			A4
FACULTY OF ENGINEERING		DIMENSIONS IN MILLIMETERS			SHEET 1 OF 1

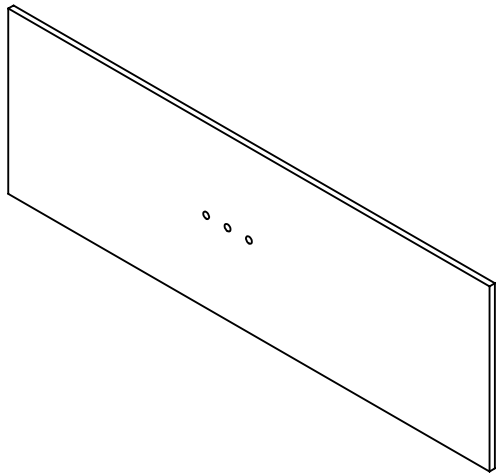

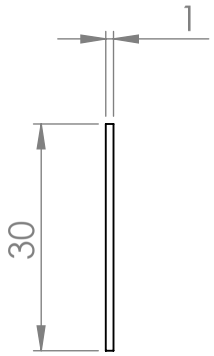

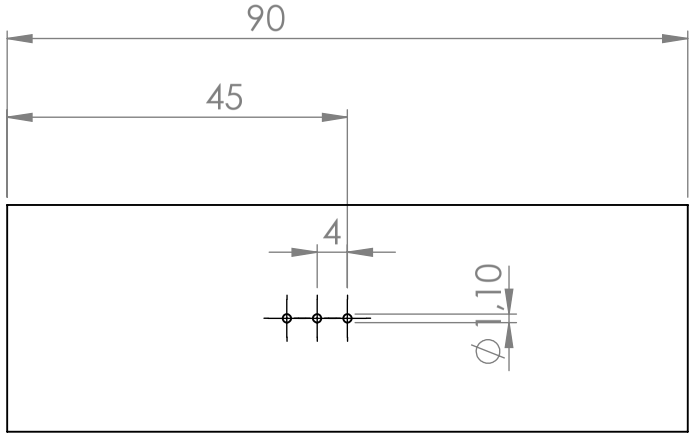

UNLESS OTHERWISE SPECIFIED: DIMENSIONS ARE IN MILLIMETERS SURFACE FINISH: TOLERANCES: LINEAR: ANGULAR:	FINISH:				DEBURR AND BREAK SHARP EDGES	DO NOT SCALE DRAWING / REVISION
	NAME	SIGNATURE	DATE			TITLE:
DRAWN						
CHK'D						
APPV'D						
MFG						
Q.A				MATERIAL:		DWG NO. Part4new / A4
				WEIGHT:		SCALE:1:1 / SHEET 1 OF 1

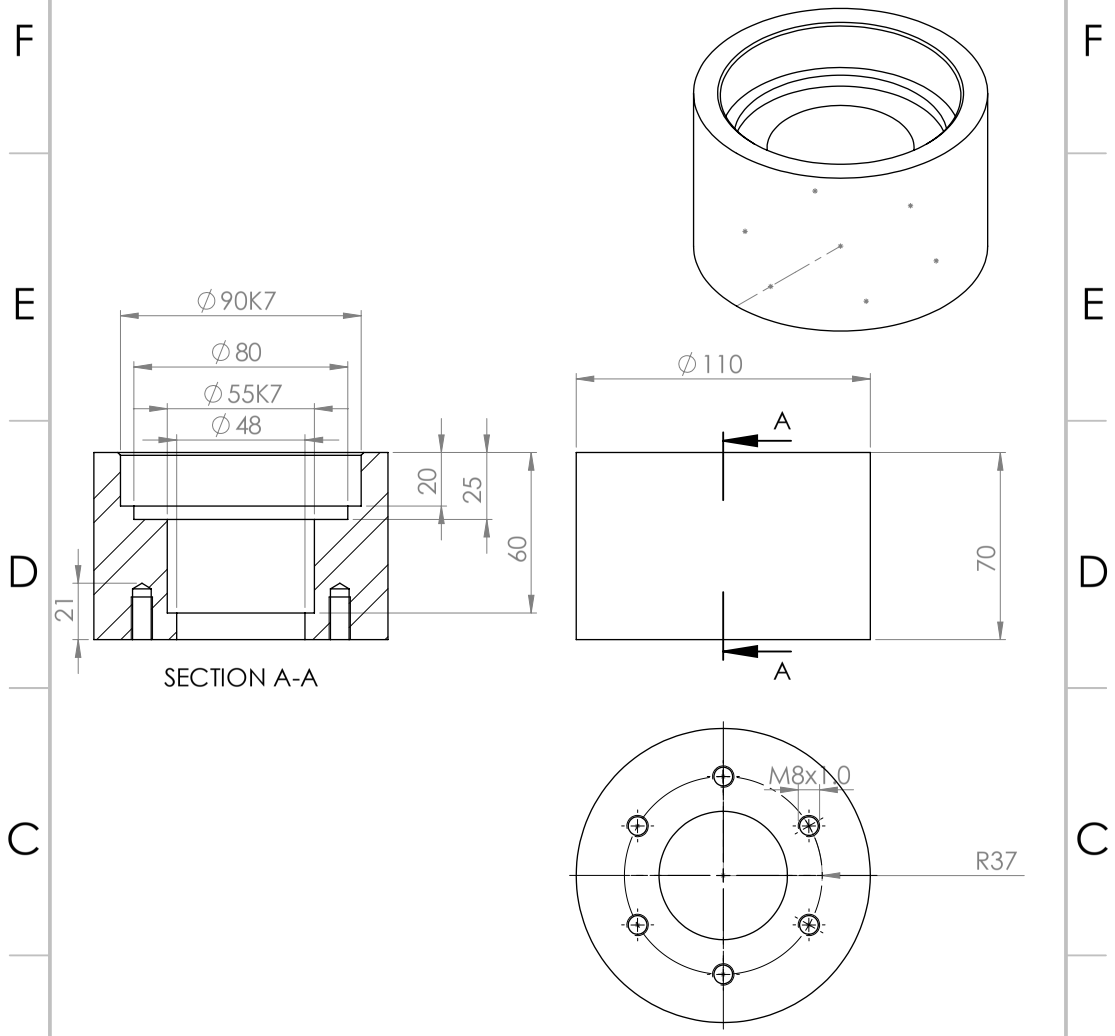

UNLESS OTHERWISE SPECIFIED: DIMENSIONS ARE IN MILLIMETERS SURFACE FINISH: TOLERANCES: LINEAR: ANGULAR:	FINISH:		DEBURR AND BREAK SHARP EDGES	DO NOT SCALE DRAWING	REVISION		
	NAME	SIGNATURE	DATE	TITLE:			
DRAWN							
CHK'D							
APPV'D							
MFG							
Q.A				MATERIAL:	DWG NO. Part6new		A4
				WEIGHT:	SCALE:1:2	SHEET 1 OF 1	

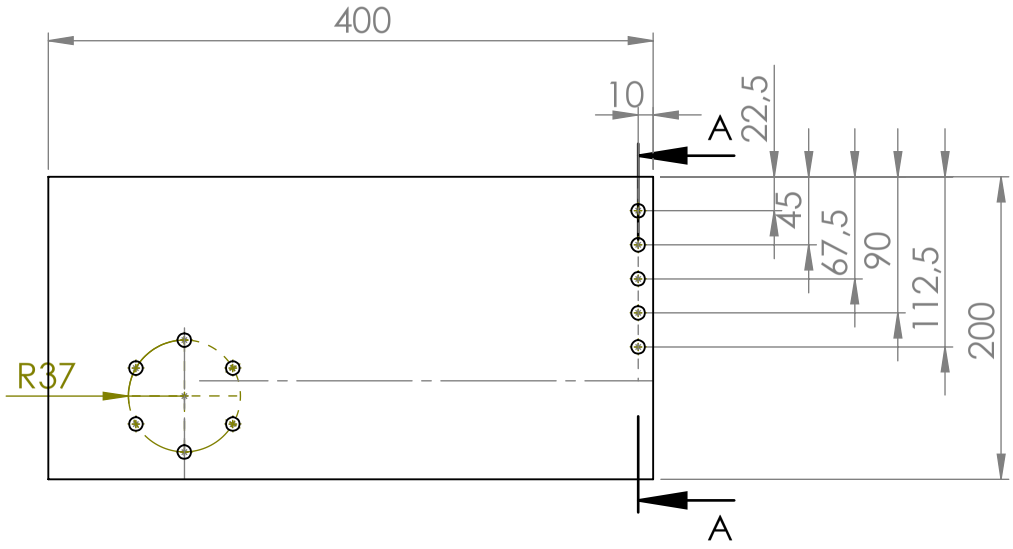

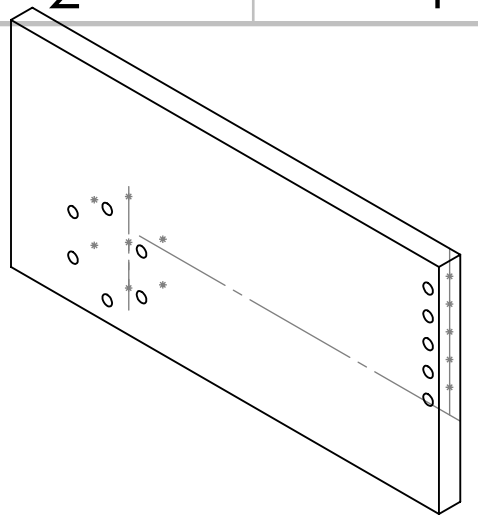

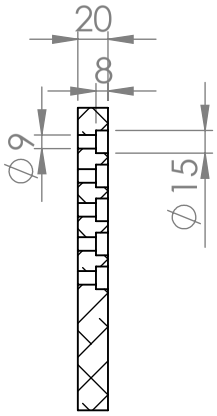

SECTION A-A

UNLESS OTHERWISE SPECIFIED: DIMENSIONS ARE IN MILLIMETERS SURFACE FINISH: TOLERANCES: LINEAR: ANGULAR:	FINISH:		DEBURR AND BREAK SHARP EDGES	DO NOT SCALE DRAWING	REVISION	
	NAME	SIGNATURE	DATE			TITLE:
DRAWN						
CHK'D						
APPV'D						
MFG						
Q.A				MATERIAL:	DWG NO. Part7new	A4
				WEIGHT:	SCALE:1:5	SHEET 1 OF 1

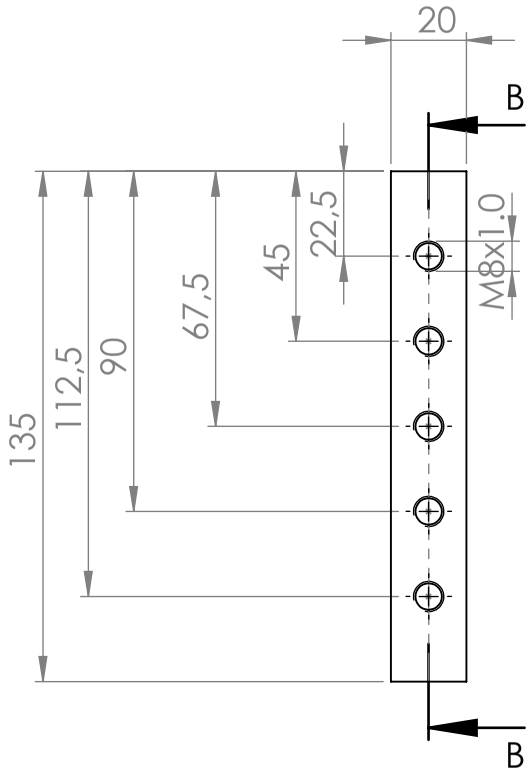

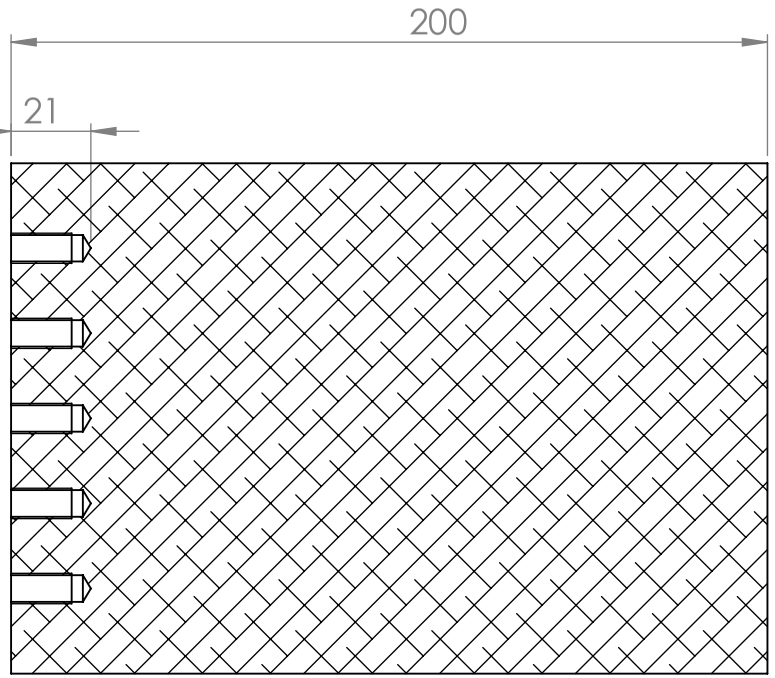

SECTION B-B

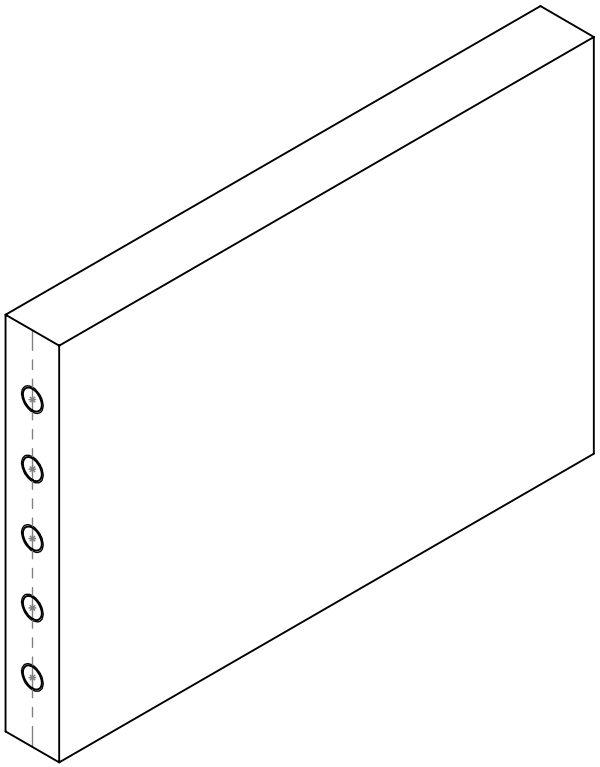

UNLESS OTHERWISE SPECIFIED: DIMENSIONS ARE IN MILLIMETERS SURFACE FINISH: TOLERANCES: LINEAR: ANGULAR:		FINISH:			DEBURR AND BREAK SHARP EDGES	DO NOT SCALE DRAWING	REVISION
	NAME	SIGNATURE	DATE			TITLE:	
DRAWN							
CHK'D							
APPV'D							
MFG							
Q.A				MATERIAL:		DWG NO. Part8new	A4
				WEIGHT:		SCALE:1:2	SHEET 1 OF 1

Appendix D

Control thermo-mechanical model

In chapter 3 Comsol 5.2 was used to create the thermo-mechanical model. Comsol 5.2 is a multi physics program that enables, among other things, to solve heat transfer problems. However, Liu et al. [3] noticed a bug in the program in an earlier version that allowed impossible physical solutions. To ensure the thermo-mechanical model will generate a representative temperature distribution, a check will be performed using analytical solutions to benchmark the FEM solution in the first part of this appendix. The second part of this appendix will be dedicated to convergence of the solution from the thermo-mechanical model, that will determine the spatial and time domain of the thermo-mechanical model.

D.1 Temperature distribution check

The analytical temperature distribution

In literature several analytical models predict the temperature distribution for certain heat fluxes. The analytical models that will be used to check the temperature distribution of the FEM model are:

$$T(x,t) = \frac{q_s}{k}\{\sqrt{\frac{4\alpha t}{\pi}}e^{\frac{-x^2}{4\alpha t}} - xerfc(\frac{x}{2\sqrt{at}})\} + T_i \tag{D.1}$$

$$T(x,t) = q_s\{\sqrt{\frac{t}{\pi k c_p \rho}}e^{\frac{-x^2}{4\alpha t}} - \frac{x}{2k}erfc(\frac{x}{2\sqrt{\alpha t}})\} + T_i \tag{D.2}$$

$$T(x,t) = \frac{q_s}{2k\sqrt{6\alpha t}}(\sqrt{6\alpha t} - x)^2 + T_i \tag{D.3}$$

Here is D.1 the exact heat diffusion [38], D.2 the exact heat diffusion 2 and D.3 the integral method heat diffusion [39]. Note that x is the distance in height starting at the heat flux. All the equations assume an infinite height of the billet, a constant heat flux q_s, thermal conductivity k, specific heat capacity c_p, density ρ and thermal diffusivity α. Al these assumptions made it impossible to describe the heat transfer problem of this thesis analytically. Therefore, comparing these analytical solutions to the complex model introduced chapter 3 is useless. However, the aim of interest in this control is to see if the heat penetration of the thermo-mechanical model gives a representative temperature distribution. For that a simpler model will suffice. In the next section the simple model will be explained into more detail.

The simple control model

In order to check the numerical model with the analytical model the assumptions have to be similar. This means that the control numerical model will be limited to the same limitations as the analytical model. The control model will be a simple billet with radius r and height H. A normal distributed heat flux will be placed on the top, while the other boundaries are thermally isolated as is shown in Figure D.1 (a). Sample points are introduced to follow the temperature over time, these are shown as red dots in Figure D.1(b).

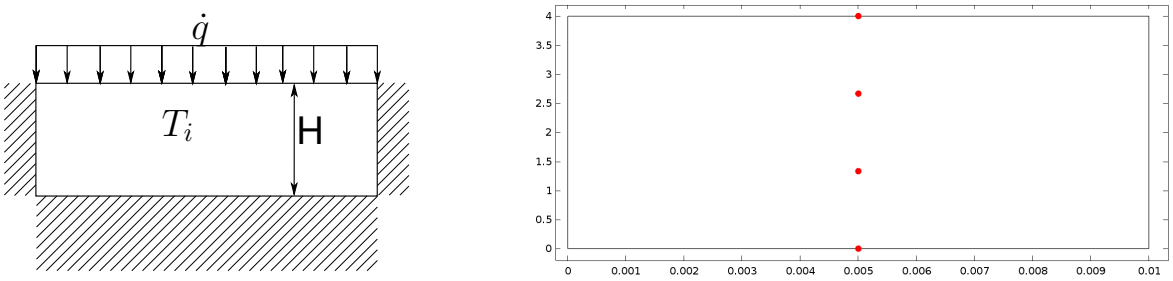

Figure D.1: *(a)Cross section simple heat transfer model (b) Data points in FEM model*

The heat flux was estimated using the average torsion of test 44 $\frac{M_{avg}\cdot\omega}{A} = 1875000W/m^2$. The other constants were taken equal to their initial value at 20 °C i.e. k = 121$\frac{W}{m\cdot K}$, c_p = 930$\frac{J}{k}$, ρ = 2760$\frac{kg}{m^3}$ and $\alpha = \frac{k}{\rho c_p} \approx$

$5.1 \cdot 10^{-5} \frac{m^2}{s}$. Note that Comsol uses the same initial condition but these are not constant along chancing temperature. As long as low temperatures are check the effect of this can be neglected.

Timespan

In the analytical equations the assumptions was made that the billet needed an infinite length, so that the bottom of the billet would not influence the heat penetration and thus the temperature distribution. Simulating an infinite length would go passed the interest of this control and therefore it was chosen to adjust the timespan to simulate an infinite length. The timespan was chosen such that the influence of the bottom could be neglected. A margin of less than 1% of the temperature of the top part in comparison to the bottom part was chosen as an acceptable range.

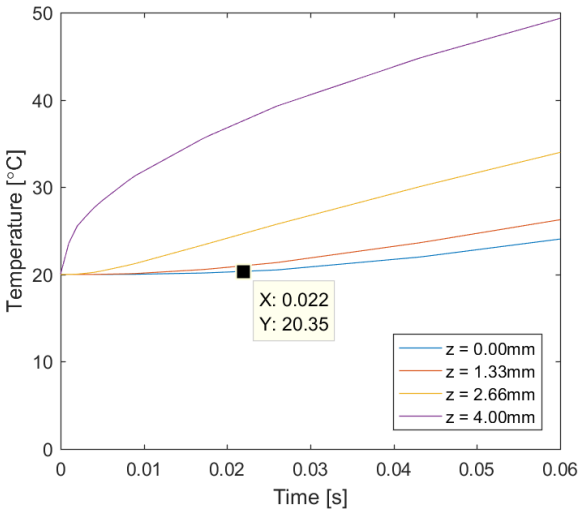

Figure D.2: *The temperature calculated by the FEM model with a constant flux at each sample point. Note at 0.022 seconds the temperature at the bottom crosses the assumed negligible boundary.*

Analytical vs numerical temperature distribution

The solution of the different analytical equations shows a substantial scatter for the temperature distribution at each sample point, as is shown in the Figure D.3. This shows that even with the assumption of the constants, the problem is difficult to describe for the whole time period. Especially the integral method shows a physically impossible solution for sample point outside the heat flux line. However, for a later time step the equation does tend to converge to a solution that agrees with the other equations. Due to the scatter of the results from the analytical equations it is impossible to conclude a correct temperature distribution. But, in the time frame were the influence of the bottom can still be neglected, the FEM model is constantly within the distribution of the analytical equations. Concluding that this version of Comsol does not show physically impossible results and the result from the model can considered representative according to the analytical equations.

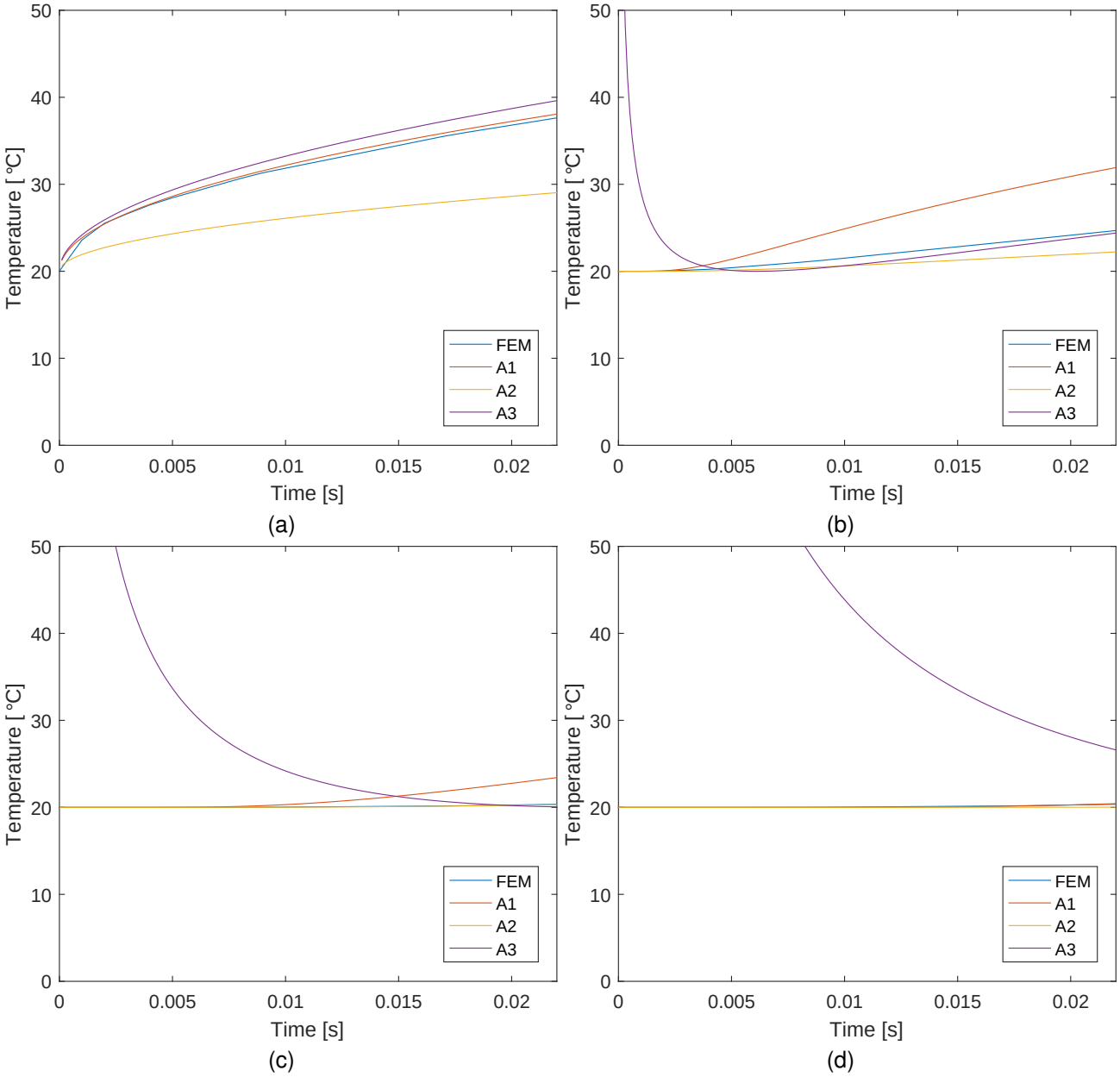

Figure D.3: *The temperature distribution of equation D.1, D.2 and D.3 vs the temperature distribution of the FEM model at all the sample points: (a) at z = 4.00mm, (b) z = 2.66mm, (c) z = 1.33mm and (d) z = 0.00mm*

D.2 Convergence check of the thermo-mechanical model

The thermo-mechanical model is solved using a backward Euler solver. For a correct numerical solution the outcome needs to converge on both the time and spatial domain. To find converging settings of the solution of the thermo-mechanical, both the mesh has been refined, shown in figure D.4(a), and the time step has been refined, shown in figure D.4(b). In the Figure it can be seen that the last two graphs overlap, but due to the resolution of the graph it is hard to see if graphs are really converging, for that error norm is introduced:

$$L^2_{time} = \int [u_n^{n+1} - u_n^n]^2 dt \qquad L^2_{spatial} = \int [u_{n+1}^n - u_n^n]^2 dt$$

For the time domain L^2_{time} is the error between the different time step graphs, where u_n^{n+1} is the finer time step graph and u_n^n the reference. For the time domain $e_{spatial}$ is the error between the different mesh graphs, where u_{n+1}^n is the finer mesh graph and u_n^n the reference graph. Note that a time step refinement causes different vector lengths therefore longer vector were compressed to lowest vector length coincidental values. In Table D.1 the results are summarized. It can be seen that Further refinement than fine mesh and time step 0.1s will not improve the accuracy of the model.

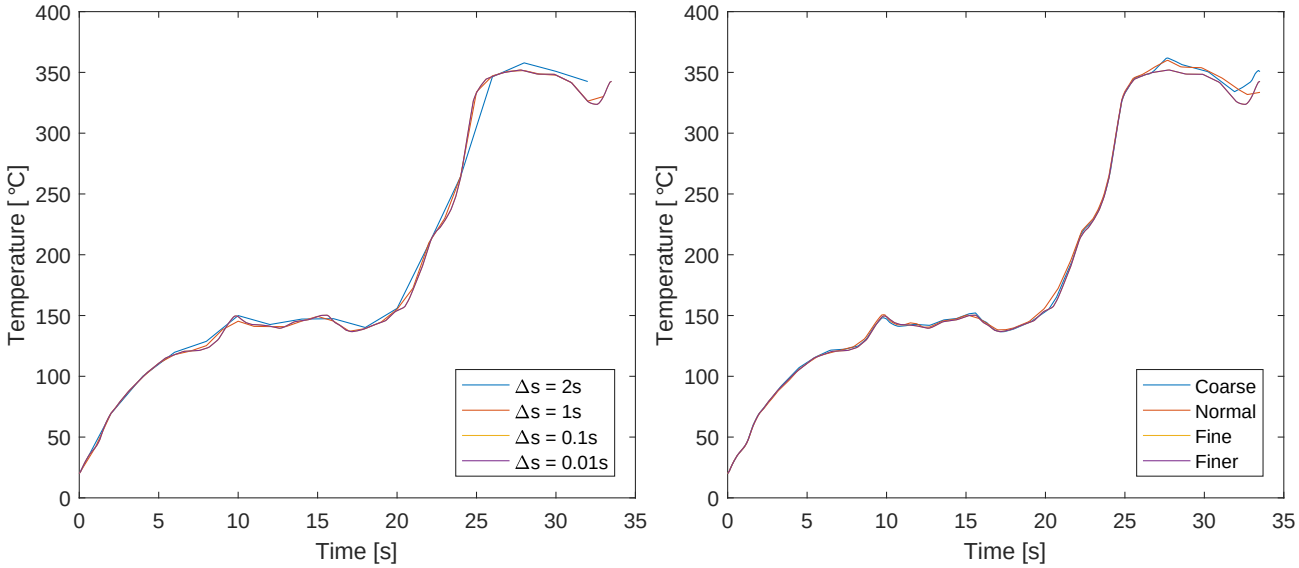

Figure D.4: *The temperature calculated by the FEM model with a constant flux at each sample point. Note at 0.022 seconds the temperature at the bottom crosses the assumed negligible boundary.*

Time step refinement	Δs1-Δ s2	Δ s01-Δ s1	Δ s0.1-Δ s0.01
L2 norm	272.3	136.2	0

Mesh refinement	Normal - Coarse	Fine - Normal	Finer - Fine
L2 norm	279.67	140.1	0

Table D.1: *L2 norm table, the error declines for each refinement. Further refinement than fine mesh and time step 0.1s will not improve the accuracy of the model*

Appendix E

Tensile test results

E.1 Rotation speed

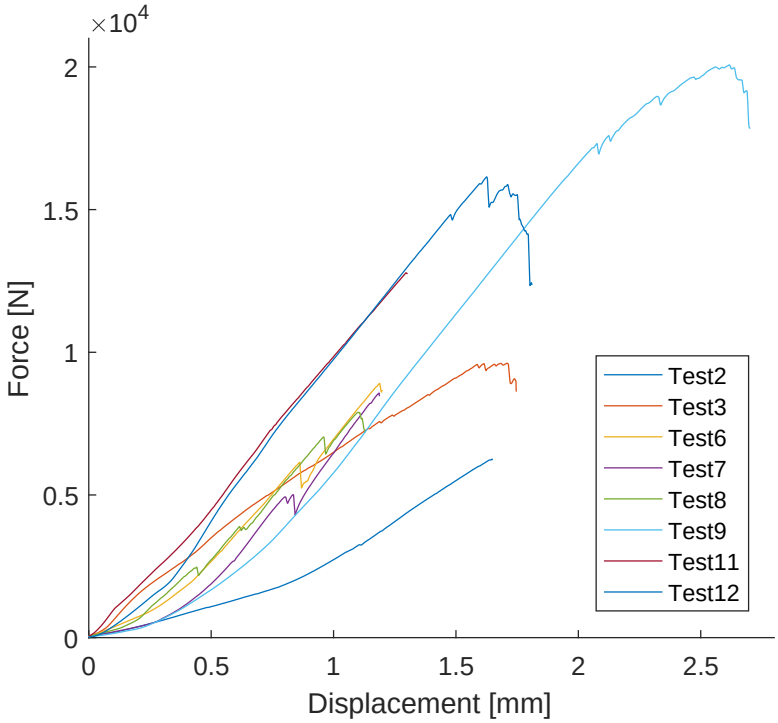

Figure E.1: *Tensile test result of samples produced with different rotation speeds*

Experiment	ω(RPM)	F(N)	T(C°)	$F_{max}(N)$	δ(mm)	Break at C&S	Break at M&C
Test 2	900	5,000	340	6.257	1.65	No	Yes
Test 3	900	5,000	320	2.323	1.75	No	Yes
Test 6	900	5,000	340	8.911	1.20	No	Yes
Test 7	900	5,000	320	8.573	1.19	Yes	No
Test 8	900	5,000	320	7.898	1.13	Yes	No
Test 9	450	5,000	330	20.071	2.73	No	Yes
Test 11	600	5,000	315	12.785	1.30	Yes	No
Test 12	600	5,000	315	16.146	1.81	Yes	No

Table E.1: *Data set 1*

E.2 Axial force

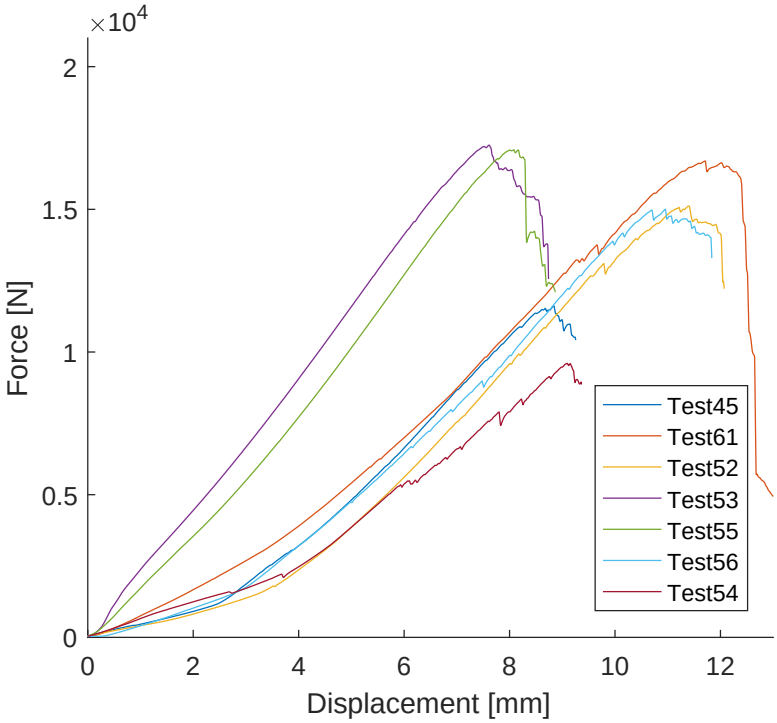

Figure E.2: *Tensile test result of samples produced with different rotation speeds*

Experiment	ω(RPM)	F(N)	T(C°)	F_{max}(N)	δ(mm)	$A_{eff}(mm^2)$	σ_s(MPa)
Test 45	450	5,000	320	6,330	2.46	92	69
Test 61	450	5,000	330	6,27	1.65	93	67
Test 52	450	7,500	330	9,617	1.75	109	88
Test 53	450	7,500	330	8,911	1.20	117	76
Test 55	450	10,000	330	8,573	1.19	127	68
Test 56	450	10,000	330	7,899	1.13	111	71
Test 54	450	12,500	325	20,071	2.70	118	170

Table E.2: *Data set 2 force*

E.3 Surface temperature

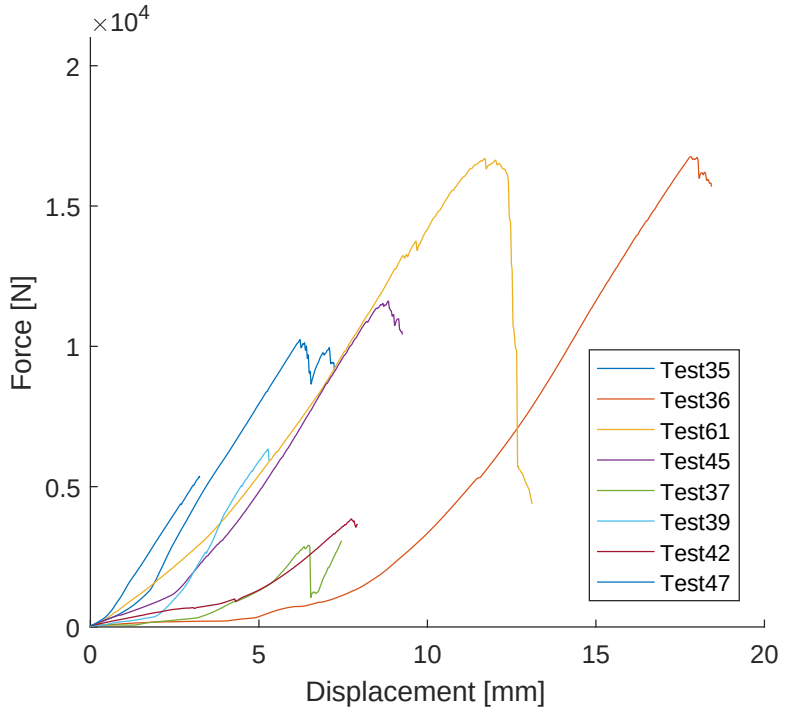

Figure E.3: *Tensile test result of samples produced with different rotation speeds*

Experiment	ω(RPM)	F(N)	T(C°)	F_{max}(N)	δ(mm)	$A_{eff}(mm^2)$	σ_s(MPa)
Test 35	450	5.000	340	6,330	2.42		
Test 36	450	5.000	335	6,257	1.65		
Test 61	450	5.000	330	9,618	1.75		
Test 45	450	5.000	320	8,911	1.20		
Test 37	450	5.000	300	8,573	1.19		
Test 39	450	5.000	270	7,898	1.13		
Test 42	450	5.000	280	20,071	2.70		
Test 47	450	5.000	250	12,785	1.30		
Test 48	450	5.000	240	0	0		

Table E.3: *Temperature data set 2*